Detailed Modeling of the Human Body in Motion to Investigate the Electromagnetic Influence of Fields in a Realistic Environment

Zur Erlangung des akademischen Grades Doktor-Ingenieur (Dr.-Ing.)
genehmigte Dissertation von M.Sc. Marija Nikolovski geb. Vuchkovikj aus
Skopje, Mazedonien
Tag der Einreichung: 09.05.2017, Tag der Prüfung: 12.07.2017
Darmstadt 2018 — D 17

1. Gutachten: Prof. Dr.-Ing. Thomas Weiland
2. Gutachten: Prof. Dr.-Ing. Herbert De Gersem

TECHNISCHE
UNIVERSITÄT
DARMSTADT

Fachbereich Elektrotechnik und Informationstechnik
Institut für Theorie Elektromagnetischer
Felder (TEMF)

Detailed Modeling of the Human Body in Motion to Investigate the Electromagnetic Influence of Fields in a Realistic Environment

Genehmigte Dissertation von M.Sc. Marija Nikolovski geb. Vuchkovikj aus Skopje, Mazedonien

1. Gutachten: Prof. Dr.-Ing. Thomas Weiland
2. Gutachten: Prof. Dr.-Ing. Herbert De Gersem

Tag der Einreichung: 09.05.2017
Tag der Prüfung: 12.07.2017

Darmstadt 2018 — D 17

Erklärung laut §9 PromO

Ich versichere hiermit, dass ich die vorliegende Dissertation allein und nur unter Verwendung der angegebenen Literatur verfasst habe. Die Arbeit hat bisher noch nicht zu Prüfungszwecken gedient.

Darmstadt, den 09. Mai 2017

Marija Nikolovski, M.Sc.

Contents

Abstract

This dissertation focuses on generalization and enhancement of the poser program called “BodyFlex”, in order to be used for deformation of different voxel-based human body models. Different postures of three voxel-based human models, HUGO, Gustav and Laura, can be generated with “BodyFlex”.

The first enhancement is related to the Free Form Deformation (FFD) technique, which is already implemented in “BodyFlex”, to allow deformation of non-axis aligned human body parts. Additionally, for deformation of the elbow and body parts which could be initially bent, the Extended Free Form Deformation (EFFD) is implemented. Both techniques deform an object by applying a deformation on a lattice with a predefined shape, which embeds the original object. The first step towards the generalization of “BodyFlex” is the automatic generation of the lattices, based on the joint positions, which is introduced in this work. Another enhancement is related to the generation of a proper posture of the HUGO model for evaluation of the electromagnetic effects from mobile phones. To this aim, an algorithm for separation of the fingers based on geometrical techniques was developed.

Two types of electromagnetic applications are described, which include a variety of postures of the human models that are generated by using “BodyFlex”. The first type is related to the analysis of the specific absorption rate (SAR) distribution in the human model, due to mobile phone radiation. In various simulation scenarios, the impact of the human hand’s position, as well as the influence of rings, earrings and eyeglasses on the SAR distribution are presented. The second type studies the influence of the position and the geometry of the human models on the SAR distribution. Three voxel-based human models, HUGO, Gustav and Laura, in a standing and sitting position are exposed to electromagnetic waves. The results for the whole body averaged SAR and the localized SAR distribution of the sitting human models are compared to the standing human models.

Zusammenfassung

Diese Dissertation befasst sich mit der Verallgemeinerung und Erweiterung des Posierungs-Programms “BodyFlex” für dessen Verwendung mit weiteren voxelbasierten Menschmodellen. Verschiedene Posen von drei voxel-basierten Menschmodellen, HUGO, Gustav und Laura können mit “BodyFlex” erzeugt werden.

Die erste Erweiterung steht in Zusammenhang mit der Free Form Deformation Technik, die bereits in “BodyFlex” implementiert ist und erlaubt die Verformung von nicht an den Koordinatenachsen ausgerichteten Körperteilen. Zusätzlich wurde zur Verformung des Ellenbogens und anderen im Ursprungsmodell gebeugten Körperteilen die Extended Free Form Deformation Technik implementiert. Beide Techniken verformen Objekte durch Anwendung eines Gitters in vordefinierter Form, das das Originalobjekt einschließt. Der erste Schritt zur Verallgemeinerung von “BodyFlex” in dieser Dissertation ist die automatische Erzeugung der Gitter anhand von Gelenkpositionen. Eine weitere Verbesserung ist die Erzeugung von Posen, die zur Simulation elektromagnetischer Felder mit Mobiltelefonen geeignet sind. Hierfür wurde ein Algorithmus zur Separation der Finger basierend auf geometrischen Techniken entwickelt.

Zwei Anwendungstypen werden beschrieben, die eine Vielzahl von mit “BodyFlex” generierten Posen beinhalten. Der erste Typ ist die Analyse der Verteilung der spezifischen Absorptionsrate (SAR) der Strahlung von Mobiltelefonen im Menschmodell. In verschiedenen Simulationsszenarien wird der Einfluss der Handposition sowie von Ringen, Ohrringen und Brillen auf die SAR-Verteilung vorgestellt. Der zweite Anwendungstyp untersucht den Einfluss der Position und Geometrie von Menschmodellen auf die SAR-Verteilung. Drei voxelbasierte Menschmodelle, HUGO, Gustav und Laura werden in stehender und sitzender Haltung elektromagnetischen Wellen ausgesetzt. Die Ergebnisse der ganzkörpergemittelten SAR und der lokalen SAR-Verteilung des sitzenden Menschmodells werden mit dem stehenden verglichen.

1 Introduction

1.1 Motivation and History

The increasing number of electric devices used in day-to-day life, attracts the attention and interest in the study of the electromagnetic field interaction with biological tissues. Understanding the field distribution inside the human body is crucial when the electromagnetic devices are being developed, because of the possible negative health effects. Unfortunately, there are huge limitations on direct measurement of the electromagnetic field inside the tissues and organs of the living organisms. As a result of the rapid development of the computer science, simulations on the human body models can be performed to predict the electromagnetic radiation effects, as well as the heating and the Specific Absorption Rate (SAR) distribution.

The development of computational human models used for variety of applications is still in focus nowadays. With the improved computer graphics and medical technique, more accurate computational human body models are being developed. The voxel-based human models, also known as tomographic models or voxel phantoms, can be created by analog photography of slices of a frozen body. But in most of the cases, the voxel-based human models are built from cross-sectional images obtained using Computer Tomography (CT) and Magnetic Resonance Imaging (MRI) devices. They are generated from the pixel data from these 2D images, transformed in three-dimensional volume elements called voxels. These models have a very large application range in the simulations of realistic electromagnetic problems. The main goal of the simulations is the evaluation of electromagnetic fields inside and outside the voxel-based human body models by numerically solving Maxwell's equations. One such numerical technique for solving Maxwell’s equations is the Finite Integration Technique (FIT), which was introduced by Weiland in 1977 [106].

The upright position of the most digital human models is the main obstacle to conduct realistic electromagnetic research activities. For the purpose of such research activities, it is very important the flexibility to generate various postures of the human body (e.g. sitting position, holding a mobile phone in the hand etc.). Some deformed human models already exist [30] [5] [32] [31] [78], but the techniques with which they are created are time consuming and the positions of the models are limited. In 2012, Gao proposed an approach for generation of a postured voxel based human model named “HUGO” [33], which was implemented within the software tool “BodyFlex” [44]. The combination of the Free Form Deformation technique (FFD) for 3D solid geometric models deformation introduced by Sederberg and Perry (1986) and the Marching Cubes (MC) algorithm introduced by Lorensen and Cline (1987) allows the generation of different positions for the HUGO model, while ensuring continuity of the tissues and conservation of the mass to an acceptable level [94] [71].

In this dissertation, an enhancement and generalization of “BodyFlex” is presented. One disadvantage of “BodyFlex” was that it worked only with the HUGO model. To improve the functionality and extend its capabilities for a general use, an algorithm for automatic placement of the control lattices, which guide the deformation process is developed. The control lattices are placed around almost all body parts, based on previously defined joint positions. With this generalization of “BodyFlex”, other voxel-based human models, like Gustav and Laura [86] can be deformed.

A very important enhancement of “BodyFlex” is the application of the Extended Free Form Deformation (EEFD) technique [27] to deform the elbow. Using this technique, control lattices with arbitrary shapes are defined to cope with the initial position of the elbow.

A new algorithm using sparse matrix logic is developed to enhance the performances of exporting the deformed human models with “BodyFlex”. Additionally, the posture and export processes are adapted for parallel execution, to use all available resources on the running machine.

In the first version of “BodyFlex”, deformations of almost all parts of the body were possible. Exceptions were the wrist and the fingers movements which required a change in the current algorithm because of the non-standard position of the forearms and the hands of the HUGO model, which are bent over the lower part of the abdomen in the original model. In recent computer graphics research, some algorithms for finger movements and hand deformations can be found. However, these algorithms were not suitable to be applied on the HUGO model, because HUGO’s fingers were not separated. Consequently, an algorithm for finger separation and movement is introduced in this dissertation.

One electromagnetic application where the wrist and the finger movement of a voxel-based human model are of interest is computing the Specific Absorption Rate (SAR). Since the electromagnetic fields produced by the mobile phone are classified by the International Agency for Research for Cancer as possibly carcinogenic to humans, it is very important to monitor, investigate and understand the possible impact by the mobile phones on the human health. There are two international bodies that have developed exposure guidelines for general public, which specify the maximal SAR values allowed for absorption [2] [3]. However, the current

SAR measurements are performed with the SAM (Specific Anthropomorphic Mannequin) phantom which is filled with homogeneous, but dispersive material. The SAR values in the hand are not measured and the impact of the hand when the mobile phone is held, on the SAR values, cannot be accurately predicted. When a hand from a voxel-based human model is present in the simulation, we are able to compute the SAR values in the hand and also to investigate the impact of the hand on the SAR values in the head of the voxel-based human model. Additionally, the effects of wearing some common jewelry and eyeglasses can be studied. Results showing the impact of the hand and some accessories (jewelry and eyeglasses) on the SAR values obtained from the simulations are presented in this dissertation.

1.2 Outline

This introductory Chapter 1 is followed by an overview of the available computational human models in Chapter 2, with a special focus on the voxel-based human models. The voxel-based human model HUGO, developed from the Visible Human Project® (VHP) , and the CST Voxel Family, originating from the GSF voxel family from Helmholtz Zentrum München — Deutsches Forschungszentrum für Gesundheit und Umwelt, which are used in this thesis, are described in detail.
Chapter 3 explains the working principle and describes the two three-dimensional deformation techniques used in this dissertation: Free Form Deformation (FFD) and Extended Free Form Deformation (EFFD). Also, in this chapter, the application of the three-dimensional rendering algorithm Marching Cubes (MC) in "BodyFlex" is shown together with its combination with the FFD technique.
In Chapter 4, the basis of electromagnetic theory, namely Maxwell's equations is given. In addition, the Finite Integration Technique (FIT) is explained, which is the time domain electromagnetic simulation algorithm used for the electromagnetic applications in this dissertation.
Chapter 5 describes the functionality and the enhancements of the poser program "BodyFlex", which is used to generate different postures of three human models: HUGO, Gustav and Laura. At first the joints positions are defined using the Voxel Model Observer (VMO) [85]. Then, an algorithm for automatic generation of the control points, which build the control lattices around almost all body parts is introduced in "BodyFlex". Two deformation techniques enable deformation of different body parts: FFD and EFFD. All body parts except the elbow are deformed using the FFD technique. As an enhancement to the first version of "BodyFlex", the FFD technique is extended for usage over non-axis aligned body parts in order to allow deformation on the wrist and the fingers of HUGO. Additionally, an algorithm for separation is developed to determine the voxels belonging to a certain finger. One

important step after the deformation process is the export of the human model in the new position. New algorithm based on the sparse matrix logic allows lower memory consumption and faster export of the deformed human model. In case of very large human model datasets, the time for posturing and export of the human model is very large. Therefore, the software is adapted for parallel execution and uses the maximum available CPU resources on the running machine.

In Chapter 6, a comparative analysis of performance between different software packages is given when posturing human models. Two commercial software packages, “Varipose®” and “SEMCAD X POP module®”, are described and their strengths and weaknesses are identified. Later, both software packages are compared to “BodyFlex” in terms of time for posturing of the human model and memory requirements.

In Chapter 7, various simulation scenarios are established to study the impact of the electromagnetic fields on original and postured human models. The analysis of the SAR distribution is conducted in two types of studies: the first type is related to the mobile phone radiation, while the second one investigates the influence of the position and the geometry of the human models exposed to incident electromagnetic wave. Within the first type of study, an investigation is conducted to examine the influence of the position of the hand and the fingers, as well as the effects of wearing eyeglasses or common jewelry, like rings and earrings on the SAR distribution due to mobile phone exposure.

Chapter 8 gives the summary of the thesis and the outlook, which includes possible future research topics related to this work.

2 Computational Human Models

The first sentence of Caon's paper [17], published in 2004 reads: "A computational model of human anatomy is a mathematical representation of the external envelope of the human body shape, together with the boundaries of the internal organs and tissues". The main reason to develop computational human models is their usage in dosimetry calculations. The first generation computational human models is developed between 1960s and 1980s. In this time period, the simplest computational human models are mainly modeled only by combining geometrical shapes. Such a set of human models human models has been developed by the Oak Ridge National Laboratory (ORNL) [77][52][19][23]. The models have head, neck, torso and legs. All internal organs, which were represented by equations of planes, ellipsoids, elliptical cylinders, cylinders, spheres and cones, were placed into the torso. The dimensions of the models including the internal organ dimensions and masses were chosen to conform to the ICRP "Reference Man" [101][53]. However, the simplicity of the internal organs shapes and their placement in a torso represented by an elliptical cylinder, do not coincide with the real anatomical organs in terms of the shape and the realistic position in the human body.

The rapid development of the computer technology starting in the 1980s contributed to the production of Computer Tomography (CT) and Magnetic Resonance Imaging (MRI) devices which could generate highly accurate cross-sectional images of internal organs. Once a dataset from the medical scans is available, a process of segmentation is conducted to identify the organs and the tissues in the human body. At the end of the segmentation process, a phantom is created to be further used in certain type of simulation software, such as: finite integration technique solvers (FIT), finite-difference time-domain (FDTD) solvers, finite element method (FEM) solvers, method of moment (MoM) solvers, or Monte-Carlo ionizing radiation simulators.

Taking the pixel data from the images as a starting point, researchers are motivated to create two types of widely used computational models: surface-based and voxel-based human models. The surface-based human models are built from triangular surface meshes, which are used to represent the tissues in the human body. They can approximate the outer surfaces and shapes of the organs and tissues in the human body in detail. These models are widely used in computer graphics domain. A very popular surface model family is the Virtual Population (ViP 3.0) [46]. This model family provides detailed and precise view of every single organ in the human body. They are equipped with 300 tissues and organs per model and a resolution of $0.5 \times 0.5 \times 0.5$ mm^3. The models are generated with extraction and processing of topologically conforming triangle surfaces. In order these models to be used in numerical modeling, they first need to be discretized, i.e. transformed into voxels or tetrahedral elements. Another example of surface models is the VHP-Female 3.0, which is created using the open-source high-resolution cryosection image dataset from the Visible Human Project® (VHP) Female [82].

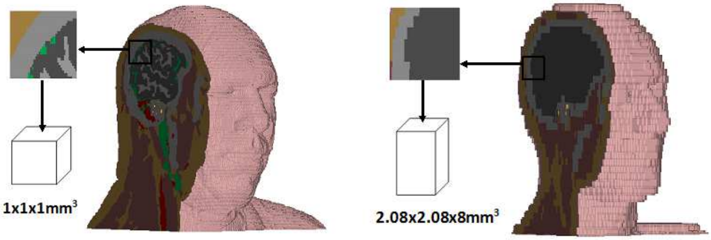

Figure 2.1.: Voxel-based human head phantoms with different voxel shape

The voxel-based human models are also known as tomographic models or voxel phantoms. They are generated from 2D cross-sectional images from medical scans, such that the pixel data are transformed in three-dimensional volume elements called voxels. As shown in Figure 2.1, a voxel can be a cube or a parallelepiped. Each voxel is filled with one material assigned with an ID number, which represents a particular tissue or organ.

Both types of human models have advantages and disadvantages. On one hand, the surface-based models can be used with numerous simulation methods. On the other hand, the voxel-based models can be used with FDTD solvers and Monte-Carlo ionizing radiation simulators (or other similar software) which are based on rectangular grids. Nevertheless, the voxel-based models can easily map highly inhomogeneous tissue distributions. The surface-based models which include many tissues and organs are described by large sized triangular surface meshes, which limits their usage only in FDTD solvers. A further advantage of the surface-based models is their possibility to describe curved organs realistically.

Currently there are 28 whole body models worldwide listed by the International Committee on Electromagnetic Safety [60] (see Appendix). Most of the listed models are voxel-based. These human models are used in various applications: radiation dosimetry [112][57][64][79][13][21], radio-frequency exposure [16][111], calculation of the specific absorption rate (SAR) [32][31][22], etc.

2.1 Voxel-based Human Models

Voxel-based human models, which describe the human anatomy quite accurately, are widely used in electromagnetic applications. These human models are obtained from different sources: whole body CT scans of cadavers, CT images from clinical examinations, MRI of volunteers and from the "Visible Human" project [4]. When a human body is scanned with CT, the attenuation of the radiated X-rays along a large number of lines is measured through cross-sections of the body [49]. The data collected from each cross-section are used to obtain an image of the scanned cross-section. Magnetic resonance imaging (MRI) is a powerful medical imaging technique which produces detailed pictures of the soft tissues in the human body and the metabolic processes therein [48]. It differs from CT, in the usage of strong magnetic field instead of X-rays. As a next step, a process of segmentation is conducted on the images available from these sources. It is a time consuming process of identification of the boundaries of every single tissue and organ visible on the medical image. All pixels which belong to a certain tissue or organ are assigned with an ID number to distinguish them from the other tissues or organs.

There are some drawbacks related to medical images which are used for generation of human models. Some images are obtained form cadavers or patients who might have some defects in the anatomy compared to a healthy human being. Also most medical images are obtained from cadavers or patients in a lying position. Therefore, their internal organs are displaced from their position in a standing person [113]. Additionally, there can be a difference in the dimension of the organs in individuals with similar size.

The listed models in Table A.1 vary in age, sex, dimension and weight. If some of these models is used in electromagnetic simulations, the obtained results should refer also to the patient. The advantage of voxel-models is the possibility to be scaled in order to fit to the dimensions of the studied human models, so they can be both increased or decreased in size. Despite their many positive characteristics, the voxel-human models also have some drawbacks. The first one is the voxel shape. Representation of the human model using voxels gives a staircase surface rather than a smooth one. This could lead to an overestimation of the size of certain organs. Another drawback is the problem related to the segmentation of tissues with dimensions smaller than the voxels dimensions. In some cases this could lead to inaccurate simulation results.

In 1986 the US National Library of Medicine (NLM) started the Visible Human Project (VHP). The goal of this project was the creation of complete, anatomically detailed, three-dimensional human bodies of a male and a female [100]. In 1994/95 the first datasets from the male and the female human bodies became available. These datasets consist of transverse CT, MR and cryosection images of male and female cadavers.

The visible human male was obtained from a cadaver of a 38 years volunteer who died from a court-ordered lethal injection [96]. Because the MR and CT images from frozen cadavers could be degraded, the body was first scanned with MR and CT. Later, CT scanning was performed again, at 1 mm slice thickness on 1 mm centers from the head to the toes on a frozen body. The next step was sectioning of the cadaver also at 1 mm intervals and photographing of the anatomical cross-sections. There were 1871 CT and anatomical images obtained from this cadaver. An example of both image types is shown in Figure 2.2.

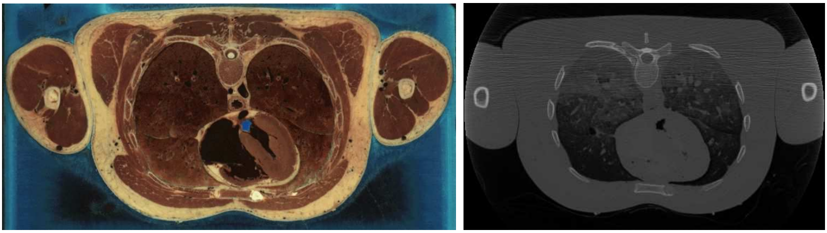

Figure 2.2.: Visible Human Male - thorax: cryosection (left) and CT scan after freezing (right) [100]

2.1.1 Human Model: HUGO

HUGO is a voxel-based human model which is built from the Visible Human Male dataset and represents anatomically realistic human body in digital form [33]. It has a height of 187 cm and a mass of 113 kg. There are numerous electromagnetic applications that use HUGO [8][9][10][11][43][45]. HUGO is available in various voxel resolutions, starting from $8 \times 8 \times 8$ mm^3 to $1 \times 1 \times 1$ mm^3. The dataset size varies from 72,000 voxels in the coarsest resolution to 380 millions in the finest resolution. HUGO consists of up to 32 different tissues. Each tissue has a unique ID number which is listed in Table 2.1. One voxel from the dataset contains only one type of tissue.

The voxel model dataset is stored in a large data file. The content of such file is not prescribed by a standard. Most of these files consist of a header of different size and a body in which the voxel values are stored. Also, there is no prescribed format for the type of the file. Namely, the voxel file is usually written in a binary format, but can also be written in ASCII format. In this case, HUGO's dataset is stored in a

Table 2.1.: HUGO: Tissue names and ID numbers [44]

ID Nr.	Tissue	ID Nr.	Tissue	ID Nr.	Tissue
1	Marrow	2	Fat	3	Bone
4	White substance	5	Gray substance	6	Skin
7	Eye	8	Muscle	9	Blood
11	Cerebellum	12	Lens	13	Nervus Opticus
14	Cartilage	15	Mucous membrane	16	Air
17	Lung	18	Large intestine	19	Kidney
20	Liver	22	Gland	23	Spleen
24	Stomach	25	Pancreas	26	Bladder
27	Gall bladder	28	Small intestine	30	Right ventricle
31	Left ventricle	32	Right atrium	33	Left atrium
43	Blood vessel	44	Blood aorta		

binary format. The file can be opened with any software which can process binary file format, for e.g Hex Editor Neo®. Using computer graphic techniques this file can be also rendered as a three dimensional human model, as shown in Figure 2.1.

2.1.2 Human Family: CST Voxel Family

The CST Voxel Family consists of seven human models in various size, age and sex shown on Figure 2.3. These models origin from the GSF voxel family from Helmholtz Zentrum München — Deutsches Forschungszentrum für Gesundheit und Umwelt [86][112]. These human models are constructed from CT and MR images of patients and contain up to 135 tissues and organs placed in 2-5 million voxels. They have a wide range of applications like simulations of exposures due to ionizing radiation, radiation therapy etc. In this dissertation, only Gustav and Laura are used.
The characteristics of the CST voxel family models are shown in Table 2.2.
CST voxel family members have more tissues compared to the HUGO model. Their tissue identification numbers are listed in Table 2.3.

Table 2.2.: CST voxel family characteristics

Model	Age	Sex	Size/cm	Mass/kg	Resolution/mm
Baby	8-weeks	Female	57	4.2	0.85 × 0.85 × 4.0
Child	7 years	Female	115	21.7	1.54 × 1.54 × 8.0
Donna	40 years	Female	176	79	1.875 × 1.875 × 10.0
Emma	26 years	Female	170	81	0.98 × 0.98 × 10.0
Gustav	38 years	Male	176	69	2.08 × 2.08 × 8.0
Laura	43 years	Female	163	51	1.875 × 1.875 × 5.0
Katja	43 years	F-pregnant	163	62	1.775 × 1.775 × 4.84

Table 2.3.: CST voxel family: Tissue names and ID numbers

ID Nr.	Tissue	ID Nr.	Tissue	ID Nr.	Tissue
1	Adrenals	2	Blood	3	Bone cortical
4	Bone m. cavity	5	Bone spongiosa	6	Brain
7	Breast glandular	8	Bronchi	9	Cartilage
10	Colon contents	11	Colon wall	12	Eye bulb
13	Eye Lens	14	Fat	15	Gall blad. cont.
16	Gall bladder	17	Heart	18	Kidney cortex
19	Kidney medulla	20	Kidney pelvis	21	Liver
22	Lung	23	Lymphatic nodes	24	Mucosa
25	Muscle	26	Oesophagus	27	Ovaries
28	Pancreas	29	Pituitary gland	30	Prostate
31	Penis	32	Muscle fat avrg.	33	Salivary glands
34	Skin	35	Small int. cont.	36	Small int. wall
37	Spinal cord	38	Spleen	39	Stomach contents
40	Stomach wall	41	Teeth	42	Testes
43	Small intestine	44	Thymus	45	Thyroid
46	Tongue	47	Tonsils	48	Trachea
49	Ureter	50	Urinary blad. cont.	51	Urinary blad. wall
52	Uterus Cervix	53	Air inside	54	Mucosa a. nasal
55	Mucosa p. nasal	56	Bone average	57	Kidney average
200	Placenta	201	Umbilical cord	202	Amniotic fluid
203	Fetus Head	204	Fetus Skin	205	Fetus Trunk
206	Fetus Arms	207	Fetus Legs	208	Fetus Brain
209	Fetus Eyes	210	Fetus Eye Lenses	211	Fetus Spinal Cord
212	Fetus Lungs	213	Fetus Heart	214	Fetus Kidneys
215	Fetus Liver	216	Fetus Stomach	217	Fetus Gall blad.
218	Fetus Cranium	219	Fetus CSF	220	Fetus Spine
255	Undefined				

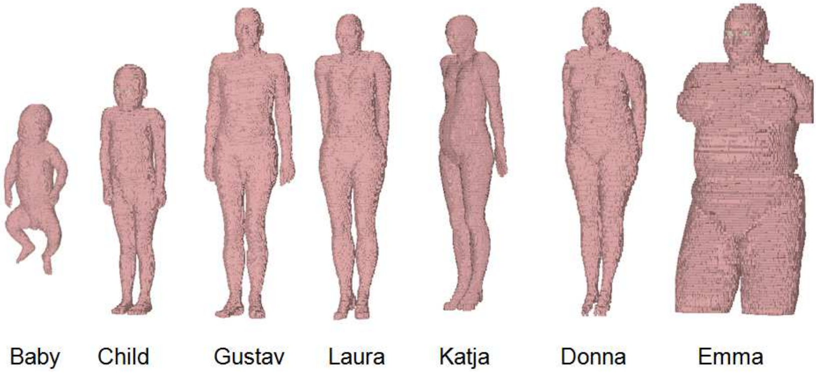

Figure 2.3.: CST Voxel Family

2.2 Dielectric Properties of Biological Tissues

The dielectric properties of the biological tissues should be provided for all frequencies to which the model is exposed within electromagnetic simulation scenarios. As available in the literature, the dielectric properties of the biological tissues at a certain frequency are determined by their relative permittivity and the total conductivity, which are expressed with the complex permittivity as follows:

$$\underline{\varepsilon}(\omega) = \varepsilon'(\omega) - j\varepsilon''(\omega) = \varepsilon_r(\omega) - j\frac{\sigma(\omega)}{\varepsilon_0\omega} \tag{2.1}$$

where ω is the angular frequency, ε_r is the relative permittivity of the material, ε_0 is the permittivity of vacuum, and σ is the total conductivity of the material.

In 1996, Gabriel et. all performed a literature survey, processing research work related to the dielectric properties of the tissues from the past five decades. The main features of the dielectric spectrum of a biological tissue can be found in [39]. The purpose of the literature survey was to find the gaps from the past researches, in order to be used as a starting point for conducting further measurements. Therefore, Gabriel et. all performed measurements of the dielectric properties of tissue in the frequency range 10 Hz to 20 GHz [40]. They used three experimental techniques based on automatic swept-frequency network and impedance analyzers on human and animal tissues, at body temperature, across the frequency range. The results obtained confirmed the literature data. Based on the previous two studies [39] and [40], a parametric model for the dielectric spectrum of tissues was developed, which describes the variation of dielectric properties of tissues as a function of frequency [41].

Each relaxation region of one tissue or organ is characterized by a single time constant τ and provides the Debye expression for the complex permittivity $\underline{\varepsilon}$ as a function of angular frequency ω in a first order approximation.

$$\underline{\varepsilon} = \varepsilon_\infty + \frac{\varepsilon_s - \varepsilon_\infty}{1 + j\omega\tau} \tag{2.2}$$

where ε_∞ is the permittivity at field frequencies where $\omega\tau >> 1$, ε_s is the permittivity at $\omega\tau << 1$. The magnitude of the dispersion is given by

$$\Delta\varepsilon = \varepsilon_s - \varepsilon_\infty \tag{2.3}$$

An alternative to the Debye equation known as the Cole-Cole equation is introduced in 2.4, because each dispersion region may be broadened by multiple contributions to it.

$$\underline{\varepsilon} = \varepsilon_\infty + \frac{\Delta\varepsilon}{1 + (j\omega\tau)^{(1-\alpha)}} \tag{2.4}$$

where α is a distribution parameter known as a measure of the broadening of the dispersion. The dielectric spectrum of a tissue can be described as a sum of multiple Cole-Cole dispersion equations and a conductivity term in which σ_i is the static ionic conductivity and ε_0 is the permittivity of free space

$$\underline{\varepsilon} = \varepsilon_\infty + \sum_n \frac{\Delta\varepsilon_n}{1 + (j\omega\tau)^{(1-\alpha)}} + \frac{\sigma_i}{j\omega\varepsilon_0} \tag{2.5}$$

To predict the dielectric behavior over a desired frequency range, appropriate parameters, available from the previous survey, should be chosen for each tissue in equation 2.5. In [41], the spectrum from 10 Hz to 100 GHz was modeled to four dispersion regions and the Cole-Cole term was used to express the frequency dependence within each region.

The Cole-Cole equation is widely used for prediction of the dielectric properties of human tissues and organs. Some commercial softwares use the Cole-Cole model to obtain the biological material properties at a given frequency. Also, there are research institutes that provide an online platform to check the dielectric material properties based on the Cole-Cole model. The first one providing a web tool is the Federal Communications Commission (FCC) from USA which could be accessed on

Table 2.4.: Dielectric properties of few CST voxel family and HUGO tissues and organs at 50 MHz and 70 MHz

Tissue	(50 MHz) Relative permittivity	(50 MHz) Conductivity (S/m)	(70 MHz) Relative permittivity	(70 MHz) Conductivity (S/m)
Bladder	26.04	0.28	24.14	0.29
Blood	94.21	1.19	84.12	1.21
Bone (Cortical)	17.74	0.057	16.35	0.06
Fat	6.87	0.034	6.39	0.035
Heart	117.95	0.65	102.89	0.69
Kidney	133.62	0.71	113.82	0.75
Liver	89.05	0.43	77.88	0.45
Lung	41.31	0.28	35.81	0.29
Muscle	77.06	0.68	70.75	0.69
Skin	107.17	0.41	87.58	0.45
Spleen	126.16	0.71	105.81	0.75

the following link[1]. The web tool is based on the 4-Cole Cole model described in [38]. The relative permittivity and conductivity of 43 human body tissues can be obtained for frequencies between 10 MHz and 6 GHz. The second one is the Nello Carrara Institute of Applied Physics (IFAC) which provides both an online tool and a standalone Win32 tool for calculation of the dielectric parameters of the human tissues based on the same model [38]. The online tool could be accessed on the following link [2]. Despite the calculation of the conductivity and premittivity, additionally the loss tangent, penetration depth and the wavelength can be calculated. Compared to the previous tool, this one provides various calculations for frequencies between 10 Hz and 100 GHz. The dielectric parameters could be obtained for all tissues at single frequency, single tissue at a certain frequency range and single tissue at single frequency.

Within this dissertation, the dielectric properties of the human tissues are obtained using the Cole-Cole model. Table 2.4 shows the dielectric properties of few human tissues at 50 MHz and 70 MHz, which are used in simulations described in Chapter 7.

---

[1] https://transition.fcc.gov/oet/rfsafety/dielectric.html

[2] http://niremf.ifac.cnr.it/tissprop/htmlclie/htmlclie.php

3 Algorithms and Techniques

This chapter discusses the algorithms and techniques implemented in “BodyFlex”. Two three-dimensional deformation techniques from the computer graphics domain are part of “BodyFlex”: the Free Form Deformation (FFD) and the Extended Free Form Deformation (EFFD). Depending on the initial position of a certain body part, one of the two deformation techniques is used. Also, an algorithm for rendering of the human models called Marching Cubes (MC) is implemented in “BodyFlex”. The combination of the FFD technique and the MC algorithm allows the user to see the postured human model before it is exported in a new voxel dataset [44]. Since the export process is time consuming, especially for large datasets, the given option can save the user a lot of time, in case the posture should be changed.

3.1 Overview of 3D Deformation Techniques

There are two classes of techniques used for deformation of human bodies: physical-based and geometry-based. The author discusses them in [105]. The physical-based techniques are widely used nowadays in computer animations. They use numerical methods, such as the finite element/difference/volume methods. Although these methods provide excellent deformations, one drawback of usage of these methods is that they are usually performed at a very high computational cost.

On the other hand, the geometry-based techniques have a much lower computational complexity. These techniques usually conduct deformation of the surface of the human model, based on the rigid movement of the skeleton. Surface interpolation techniques, together with the skeleton model are used to obtain the desired posture. Some well known existing techniques are Linear Blend Skinning (LBS), Skeleton Subspace Deformation (SSD) [72], [68] and Pose Space Deformation (PSD) [69], [89], [65].

Geometry-based deformation techniques have been introduced earlier than the physical-based deformation techniques. A very efficient method for solid object deformations is introduced by Barr [12]. Transformations of an object include stretching, bending, twisting, and tapering operations. In the same year, Cobb presents the first modeling tool allowing the user to define bumps with different shapes [25]. She uses the basic warp technique and extends it by introducing the region warp and the skeletal warp.

A very popular and widely used geometry-based technique for deformation of voxel models is the Free Form Deformation (FFD) technique [94]. The working principle of this technique is such that the model is embedded into a cubic-shaped lattice and the deformation of the lattice is translated to the embedded model, as described later in this chapter. An excellent survey of spatial deformation techniques, to which the FFD technique and its extensions belong, is given by Gain [42]. One limitation of the classical FFD technique is the initial cubic shape of the lattice used for the deformation. To overcome this limitation, Coquillart [27] presents the Extended Free Form Deformation technique (EFFD), which allows the definition of non-cuboid lattices.

A very important factor when choosing a technique to deform fine-resolution voxel models is the computational efficiency. The HUGO model has more than 300 million voxels in its finest resolution, which demands high computational resources for calculating deformations. Using the physical-based techniques, it would take a very long time to achieve the desired position of the human model. Therefore, in the present work, an extension of the classical FFD technique to initially rotated Cartesian parallelepiped and lattices is introduced, to cope with the initial positions of the arms, hands and fingers in the human models. Additionally, the EFFD technique is introduced to deform the elbow using arbitrary shaped lattices.

3.2 Free Form Deformation Technique (FFD)

The Free Form Deformation technique has originally been introduced in 1986 by Sederberg and Parry [94]. Using this technique, solid geometric models with various complexity can be deformed in a free-form manner. During the deformation of the solid geometric model, it is possible to maintain its continuity and preserve its volume. Nowadays, the FFD technique is still widely used in the computer graphics domain, to deform flexible objects.

The FFD technique is usually applied to flexible objects, which can be deformed easily. The object is embedded in a flexible FFD control lattice which has a three-dimensional parallelepiped form. One FFD control lattice has control points defined on the nodes of the lattice. A lattice can be deformed by moving the control points. The main idea behind the FFD technique is to deform the embedded object by imposing the deformation on the FFD control lattice. As the FFD control lattice is deformed, the embedded object is deformed along with it.

Mathematically, the FFD technique is defined with the following algorithm, described also by [44]:

Step 1: Definition of the FFD control lattice and calculation of the local coordinates of the surface in the parallelepiped region
Figure 3.1 shows a parallelepiped which represents an FFD control lattice.

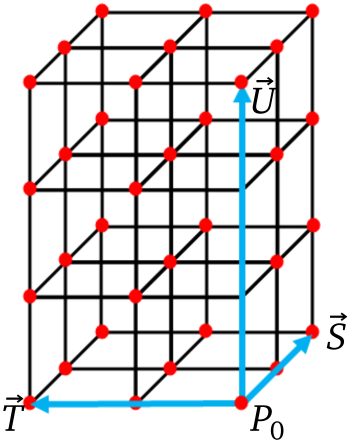

Figure 3.1.: Local coordinate system (LCS) imposed on a parallelepiped region

At the beginning of the deformation process, the local coordinates of every point $P(x,y,z)$ of the embedded object are calculated. Therefore, a Local Coordinate System (LCS) $P_0 - STU$ is imposed on the parallelepiped, where P_0 is the origin of the LCS. Any point P of the original model has local coordinates (s,t,u) such that:

$$\vec{P}(x,y,z) = \vec{P_0}(x,y,z) + s\vec{S} + t\vec{T} + u\vec{U} \tag{3.1}$$

A vector solution for the (s,t,u) coordinates of P by using linear algebra is:

$$s = \frac{\vec{T}\times\vec{U}\cdot(\vec{P}-\vec{P_0})}{\vec{T}\times\vec{U}\cdot\vec{S}}, \quad t = \frac{\vec{U}\times\vec{S}\cdot(\vec{P}-\vec{P_0})}{\vec{U}\times\vec{S}\cdot\vec{T}}, \quad u = \frac{\vec{S}\times\vec{T}\cdot(\vec{P}-\vec{P_0})}{\vec{S}\times\vec{T}\cdot\vec{U}} \tag{3.2}$$

It should be noticed that any point in the parallelepiped can have (s,t,u) values in range $0 < s < 1$, $0 < t < 1$ and $0 < u < 1$.
Step 2: Impose a grid of control points
The next step in the deformation process is the definition of control points $\vec{C}_{\mathrm{ijk}}$ on the parallelepiped, which lie on the nodes of the lattice. The FFD control points are shown on Figure 3.1 in red. There are in total $(l+1)\times(m+1)\times(n+1)$ FFD control points, where l,m and n are the number of subdivisions along each of the

three directions $\vec{S}, \vec{T}$ and $\vec{U}$. These FFD control points form $l+1$ planes in the $\vec{S}$ direction, $m+1$ planes in the $\vec{T}$ direction, and $n+1$ planes in the $\vec{U}$ direction. The locations of the FFD control points are defined as

$$\vec{C}_{\mathrm{ijk}} = \vec{P}_0(x,y,z) + \frac{i}{l}\vec{S} + \frac{j}{m}\vec{T} + \frac{k}{n}\vec{U} = \vec{P}_0(x,y,z) + \vec{C}'_{\mathrm{ijk}}(s,t,u) \tag{3.3}$$

such that $0 \leq i \leq l$, $0 \leq j \leq m$ and $0 \leq k \leq n$. The desired object shape is obtained by deformation of the FFD control lattice. It is deformed by moving the FFD control points $\vec{C}_{\mathrm{ijk}}$ from their initial position.

Step 3: Deform the original object

The deformation function is defined by a trivariate tensor product. The deformed position P_{FFD} of an arbitrary point P is found by first computing its (s,t,u) coordinates from equation 3.1, and then evaluating in:

$$\vec{P}_{\mathrm{FFD}} = \sum_{i=0}^{l}\sum_{j=0}^{m}\sum_{k=0}^{n} H_i^l(s) H_j^m(t) H_k^n(u) \vec{C}'_{\mathrm{ijk}} \tag{3.4}$$

where $\vec{P}_{\mathrm{FFD}}$ is a vector containing the local coordinates of the displaced point, $\vec{C}'_{\mathrm{ijk}}$ is a vector containing the local coordinates of the control point, and H is a basis function. Various basis functions can be chosen in Equation 3.4, such as: B-spline FFD [47], rational Bernstein FFD [29][61] and non-uniform rational B-splines (NURBS) [67]. Sederberg and Parry formulate the FFD using Bernstein polynomials [94]. The Bernstein basis function is given by the following formula:

$$B_i^n(t) = \frac{n!}{i!(n-i)!} t^i (1-t)^{n-i} = \binom{n}{i} t^i (1-t)^{n-i} \tag{3.5}$$

Using the Bernstein basis function B, instead of the basis function H in equation 3.4 results in

$$\vec{P}_{\mathrm{FFD}} = \sum_{i=0}^{l}\sum_{j=0}^{m}\sum_{k=0}^{n} B_i^l(s) B_j^m(t) B_k^n(u) \vec{C}'_{\mathrm{ijk}} \tag{3.6}$$

Applying equation 3.5 to equation 3.6 results in:

$$\vec{P}_{\mathrm{FFD}} = \sum_{i=0}^{l}\sum_{j=0}^{m}\sum_{k=0}^{n}\binom{l}{i}s^{i}(1-s)^{l-i}\binom{m}{j}t^{j}(1-t)^{m-j}\binom{n}{k}u^{k}(1-u)^{n-k}\vec{C}'_{\mathrm{ijk}} \qquad (3.7)$$

In equation 3.7, the control points $\vec{C}'_{\mathrm{ijk}}$ are coefficients of the Bernstein polynomial. The Bernstein basis function is commonly used in the Bezier curve and the Bezier surface patch. Namely, the edges of the parallelepiped are mapped into Bezier curves, defined by the control points on the respective edges. Similarly, the faces map into tensor product Bezier surface patches, defined by the control points on the respective faces.

Once having the deformed position P_{FFD} of an arbitrary point P in LCS, its coordinates in the Global Coordinate System (GSC), can be obtained using 3.1. With this last step, the position of any point in the object, can be calculated.

3.3 Extended Free Form Deformation Technique (EFFD)

Although the FFD is a powerful technique, arbitrarily shaped deformations are not possible, because of the limitation of the FFD to use parallelepipedical shape of the FFD lattice.

In 1991, Coquillart introduced a method, which is an extension of the FFD technique proposed by Sederberg and Parry [27][94]. This method is called Extended Free-Form Deformation (EFFD). All the advantages of FFD are not only retained, but extended. The main advantage of this method is the possibility of using non-parallelepipedic 3D lattices for object deformation. Moreover, an arbitrary shape of the boundary is allowed.

The EFFD algorithm follows the workflow of the FFD algorithm:

Step 1: Definition of the EFFD control lattice and computation of the local coordinates of each point of the object in the EFFD lattice region

As previously mentioned, the EFFD control lattice can have an arbitrary shape. Figure 3.2 shows two arbitrary shaped EFFD control lattices.

Because of the arbitrary shape of the EFFD control lattice, any point P of the original model has local coordinates (s, t, u), which are computed using Newton's method. The main problem using the Newton method is the possible failure to converge to the root. Therefore, it is important to choose a good starting point for the Newton iteration. Choosing s = 0.5, t = 0.5 and u = 0.5 as a starting point often leads to very good convergence. To protect from divergence, an under-relaxation factor in the interval can be defined.

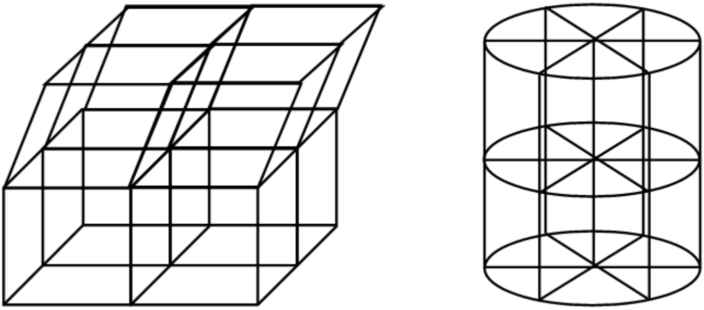

Figure 3.2.: Arbitrary shaped EFFD control lattices: decahedron (left) and cylinder (right) [27]

Step 2: Impose a grid of control points
The control points on the EFFD control lattice are defined on every intersection between two edges, i.e in the lattice nodes. The EFFD control lattice is deformed by the movement of the control points. All the transformations applied by the user to the lattice are passed to the object. The local coordinates of the control points are obtained also by using the Newton method, due to the arbitrary shape of the EFFD control lattice.

Step 3: Deform the original object
The calculation of the deformed position of an arbitrary point P, which belongs to the embedded object, is equivalent to the FFD case given by Equation 3.4.

3.3.1 Application of the EFFD in the Poser Program

The Extended Free Form Deformation technique is used in "BodyFlex" in order to deform the elbow. Because of the specific initial position of the arms of the HUGO model, putting a parallelepipedical shape of the FFD control lattice can lead to an unsatisfactory deformation of this body part. Therefore, a decahedron is defined as an EFFD control lattice. The decahedron is built from two hexahedrons. A description of the algorithm for elbow deformation is given in Chapter 5.

In order to use the EFFD algorithm with a decahedron lattice shape, one mapping and two methods should be implemented: mapping a hexahedron to a unit cube, the Gauss-Jordan elimination method and Newton's method. The local coordinates of an object point P can not be obtained by simply solving a set of linear equations, as in the FFD case. Therefore, a mapping of the coordinates of the hexahedron to a unit cube is needed.

Mapping a Hexahedron to a Unit Cube

Mapping a hexahedral form from a Cartesian coordinate system (x, y, z) to a unit cube or half of the unit cube with coordinates (m, n, p) is described in [103]. Figure 3.3 shows the hexahedron and the eight vertices on the corners (left) which are mapped to the eight vertices on the corners of the unit cube (right). All vectors and matrices described below have 8 elements, corresponding to the 8 vertices on the corners of the hexahedron.

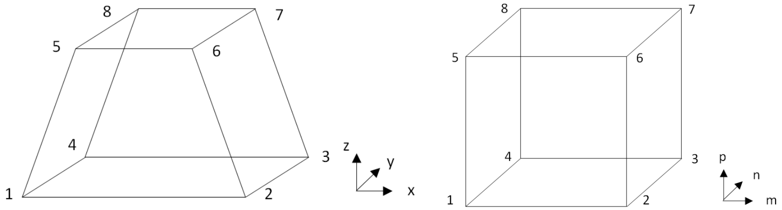

Figure 3.3.: Hexahedron (left) mapped on a cube (right) [103]

The Cartesian coordinates (x, y, z) expressed in terms of (m, n, p) can be obtained using the trilinear functions:

$$\begin{cases} x = \alpha_1 + \alpha_2 m + \alpha_3 n + \alpha_4 p + \alpha_5 mn + \alpha_6 np + \alpha_7 mp + \alpha_8 mnp \\ y = \beta_1 + \beta_2 m + \beta_3 n + \beta_4 p + \beta_5 mn + \beta_6 np + \beta_7 mp + \beta_8 mnp \\ z = \gamma_1 + \gamma_2 m + \gamma_3 n + \gamma_4 p + \gamma_5 mn + \gamma_6 np + \gamma_7 mp + \gamma_8 mnp \end{cases} \tag{3.8}$$

The system can be expressed in vector form as follows:

$$\begin{cases} \mathbf{x} = \mathbf{M}\boldsymbol{\alpha} \\ \mathbf{y} = \mathbf{M}\boldsymbol{\beta} \\ \mathbf{z} = \mathbf{M}\boldsymbol{\gamma} \end{cases} \tag{3.9}$$

Where:

$$\boldsymbol{\alpha} = \begin{bmatrix}\alpha_1\\ \alpha_2\\ \alpha_3\\ \alpha_4\\ \alpha_5\\ \alpha_6\\ \alpha_7\\ \alpha_8\end{bmatrix}, \boldsymbol{\beta} = \begin{bmatrix}\beta_1\\ \beta_2\\ \beta_3\\ \beta_4\\ \beta_5\\ \beta_6\\ \beta_7\\ \beta_8\end{bmatrix}, \boldsymbol{\gamma} = \begin{bmatrix}\gamma_1\\ \gamma_2\\ \gamma_3\\ \gamma_4\\ \gamma_5\\ \gamma_6\\ \gamma_7\\ \gamma_8\end{bmatrix}, \boldsymbol{x} = \begin{bmatrix}x_1\\ x_2\\ x_3\\ x_4\\ x_5\\ x_6\\ x_7\\ x_8\end{bmatrix}, \boldsymbol{y} = \begin{bmatrix}y_1\\ y_2\\ y_3\\ y_4\\ y_5\\ y_6\\ y_7\\ y_8\end{bmatrix}, \boldsymbol{z} = \begin{bmatrix}z_1\\ z_2\\ z_3\\ z_4\\ z_5\\ z_6\\ z_7\\ z_8\end{bmatrix}$$

$$\mathbf{M} = \begin{bmatrix}
1 & m_1 & n_1 & p_1 & m_1n_1 & n_1p_1 & m_1p_1 & m_1n_1p_1\\
1 & m_2 & n_2 & p_2 & m_2n_2 & n_2p_2 & m_2p_2 & m_2n_2p_2\\
1 & m_3 & n_3 & p_3 & m_3n_3 & n_3p_3 & m_3p_3 & m_3n_3p_3\\
1 & m_4 & n_4 & p_4 & m_4n_4 & n_4p_4 & m_4p_4 & m_4n_4p_4\\
1 & m_5 & n_5 & p_5 & m_5n_5 & n_5p_5 & m_5p_5 & m_5n_5p_5\\
1 & m_6 & n_6 & p_6 & m_6n_6 & n_6p_6 & m_6p_6 & m_6n_6p_6\\
1 & m_7 & n_7 & p_7 & m_7n_7 & n_7p_7 & m_7p_7 & m_7n_7p_7\\
1 & m_8 & n_8 & p_8 & m_8n_8 & n_8p_8 & m_8p_8 & m_8n_8p_8
\end{bmatrix}$$

When the global coordinates of the initial shape (the hexahedron) and the local coordinates that should be obtained (the coordinates of the unit cube) are already known, the coefficients for the hexahedron $\boldsymbol{\alpha}, \boldsymbol{\beta}$ and $\boldsymbol{\gamma}$, can be computed easily. To this aim, the inverse matrix $\mathbf{M}^{-1}$ is obtained by using the Gauss-Jordan elimination method [6].

Knowing the coefficients of the hexahedron $\boldsymbol{\alpha}, \boldsymbol{\beta}$ and $\boldsymbol{\gamma}$ as well as the Cartesian coordinates of the eight vertices on the corners of the hexahedron, the coordinates (m, n, p) from which the $\mathbf{M}$ matrix consists of, can be obtained by using the Newton method described next in this section.

Newton's Method

Newton's method is a method which iteratively calculates better approximation to the roots of a real-valued function [84].

The system of trilinear equations given in Eq. 3.8 is a system of 3 non-linear equations with 3 unknowns m, n, and p. In order to use the Newton method for solving the system, it should be reformulated as in Eq. 3.10

$$\begin{cases} f_1(m,n,p) = \alpha_1 + \alpha_2 m + \alpha_3 n + \alpha_4 p + \alpha_5 mn + \alpha_6 np + \alpha_7 mp + \alpha_8 mnp - x \\ f_2(m,n,p) = \beta_1 + \beta_2 m + \beta_3 n + \beta_4 p + \beta_5 mn + \beta_6 np + \beta_7 mp + \beta_8 mnp - y \\ f_3(m,n,p) = \gamma_1 + \gamma_2 m + \gamma_3 n + \gamma_4 p + \gamma_5 mn + \gamma_6 np + \gamma_7 mp + \gamma_8 mnp - z \end{cases} \tag{3.10}$$

The same system in vector form is given by

$$\mathbf{f}(v) = 0 \tag{3.11}$$

where **v** and **f** are

$$\mathbf{v} = \begin{bmatrix} m \\ n \\ p \end{bmatrix}, \quad \mathbf{f} = \begin{bmatrix} f_1(v) \\ f_2(v) \\ f_3(v) \end{bmatrix}$$

The next step is to calculate the Jacobian matrix, which contains the first-order partial derivatives of a vector-valued function. The Jacobian matrix of the trilinear system of equations is a matrix with dimensions 3 by 3, defined as:

$$\mathbf{J} = \begin{bmatrix} \frac{\partial f_1}{\partial m} & \frac{\partial f_1}{\partial n} & \frac{\partial f_1}{\partial p} \\ \frac{\partial f_2}{\partial m} & \frac{\partial f_2}{\partial n} & \frac{\partial f_2}{\partial p} \\ \frac{\partial f_3}{\partial m} & \frac{\partial f_3}{\partial n} & \frac{\partial f_3}{\partial p} \end{bmatrix} \tag{3.12}$$

The first guess of the solution is $v = v_0$ and the functions **f** and the Jacobian **J** are evaluated. Usually the initial guess for finding the coordinates (m,n,p), from the given (x,y,z) coordinates is chosen to be the middle point of the cube $(0.5, 0.5, 0.5)$. The successive approximations to the solution are obtained using the formula:

$$v_{n+1} = v_n - \mathbf{J}^{-1}\mathbf{f}(v_n) \tag{3.13}$$

The algorithm for the Newton method first checks if the Jacobian matrix is singular. If the Jacobian matrix is singular, then a new initial guess should be chosen. The condition for convergence of the system of non-linear equations is that the absolute value of the vector $\mathbf{f}(v_n)$ is smaller than prescribed tolerance ϵ:

$$|\mathbf{f}(v_n)| < \epsilon \tag{3.14}$$

The successive approximation of solution is checked in certain number of iterations. If the maximum number of iterations is reached the solution is not found. Also, if the absolute value of the vector $\mathbf{f}(v_n)$ is larger than previously defined big number, which could not be the solution, then the solution does not converge. To protect from this situation and to improve the convergence, an under-relaxation factor c in the interval $0 < c < 1$ is defined. The current solution starts with $c = 0.9$ and it is decreased for 0.1 each time the solution does not converge. When the under-relaxation factor c is decreased, the number of iterations is reset, which in the current algorithm is set to 100. In this case, the successive approximation of the solution is obtained using the formula:

$$v_{n+1} = v_n - c\mathbf{J}^{-1}\mathbf{f}(v_n) \tag{3.15}$$

The previously described Newton's method algorithm is written in pseudo code in Appendix A. In the pseudo code, the function **FuncF** evaluates the function **f** as described in Eq. 3.10. Further, the function **Jacobian** calculates the Jacobian matrix, using the Eq. 3.12.

The input parameters for the algorithm are the following:

- v_0 - the initial guess
- α - an array of coefficients for the first trilinear equation
- β - an array of coefficients for the second trilinear equation
- γ - an array of coefficients for the third trilinear equation
- p - point to be transformed from global to local coordinate system

3.4 Relationship between FFD and EFFD Techniques

In order to deform the human body parts satisfactorily, both techniques are implemented in the poser program "BodyFlex". Most of the body parts are axis-aligned, which allows a parallelepipedical control lattice to be placed around them. Also there are some body parts which are non-axis aligned, but simply rotated around one or more axes. For deformation of these body parts, the parallelepiped-shaped control lattice can be also used. However, there are some body parts which are initially bent and can not be embedded in a parallelepipedical lattice. Therefore an arbitrary shaped lattice must be used. In the poser program "BodyFlex", the FFD algorithm is applied to all body parts, while the EFFD algorithm is used for deformation of the tissues around both elbows and between the elbows and the wrists.

Regarding performance, the FFD algorithm is preferred over the EFFD algorithm. The FFD algorithm is faster and requires less memory compared to the EFFD algorithm. Therefore, the deformation of the most body parts is conducted using FFD control lattices.

Although the deformation of the human body parts causes a change of the position of the tissues, their continuity must be maintained after their deformation. In order to maintain the continuity of the tissues which are embedded in neighboring control lattices, there has to be a connection between the control lattices. This connection could be achieved by a shared face. Therefore, the FFD control lattice which embeds the tissues above the elbow should be connected to the EFFD control lattice placed around the elbow, through the shared face. Figure 3.4 shows the EFFD control lattice around the right elbow and the FFD control lattice above the elbow.

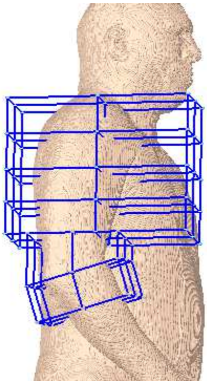

Figure 3.4.: FFD and EFFD control lattices

3.5 Marching Cubes Algorithm for Rendering (MC)

In 1987, Lorensen and Cline introduced a high-resolution 3D surface construction algorithm called marching cubes (MC) [71]. This algorithm constructs human models from a 3D data array, such that it creates a polygonal representation of constant density surfaces. The 3D surface images are widely used in medical applications. They are constructed from multiple 2D slices of computer tomography (CT), magnetic resonance imaging (MRI), and single-photon emission computed tomography (SPECT).

Some algorithms for 3D surface construction existed before MC was introduced: contour connection [63], the cuberille approach [50], and the ray casting method [35]. However, all of them have some drawbacks because they do not consider some of the useful information in the original data.
The basic idea of the MC algorithm is to extract a polygonal mesh of an iso-surface from a three-dimensional discrete scalar field [71]. The MC algorithm is already implemented in the first version of "BodyFlex" [44]. In this implementation, the three-dimensional discrete scalar field consists of the tissue ID numbers of the voxels from which the human model is built. An example to describe the working principle of the MC algorithm is explained by Gao in [44].

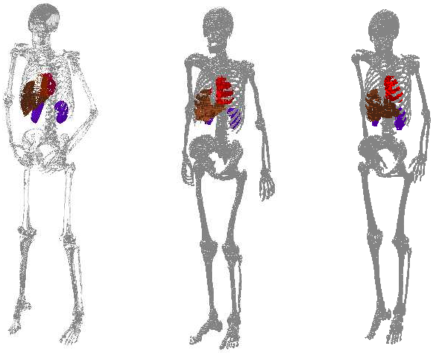

Figure 3.5.: Bones, liver, heart and kidneys of HUGO (left), Gustav (middle) and Laura (right) rendered with the marching cubes algorithm

The new version of the rendering function in "BodyFlex" allows choosing one or more tissues or organs at once, whose surface can be drawn in 3D. This option helps users to get a more clear picture of the tissues and organs of interest after a certain deformation of the human model. Figure 3.5 shows different tissues and organs of HUGO, Gustav and Laura, which are rendered with the MC algorithm.

3.6 Combination of the FFD Technique and the MC Algorithm

The main reason to use the marching cubes algorithm in "BodyFlex" is not only the high rendering speed, but also the feature to preserve the continuity of the deformed human model. In a combination with the FFD technique, the deformed human model can be drawn without being exported first [44].

An example for explaining the advantage of combining the FFD technique and the MC algorithm is given by Gao [44].

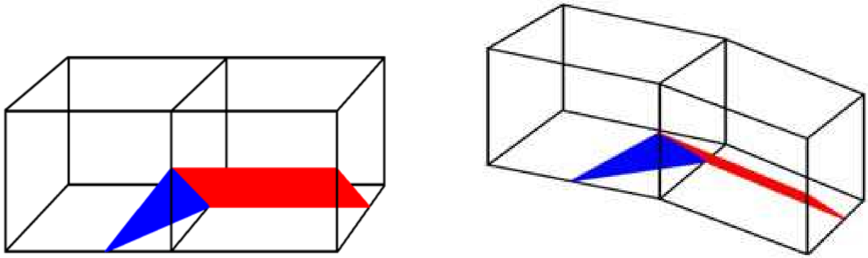

Figure 3.6.: Two marching cubes side by side: before model deformation (left) and after the model deformation (right) [44]

Figure 3.6 shows two imaginary cubes of the MC algorithm, which are placed one next to the other. Each of them contains one facet: a blue triangular facet in the left and a red rectangular facet in the right cube. These connected facets belong to a certain tissue or organ. They should remain connected even after deformation of the human model because they build an outer surface of that certain tissue or organ. When a deformation is imposed to the human model, the voxels might change their initial position, as shown in Figure 3.6 right. Despite of the changed position of the voxels, the combination of both techniques (FFD and MC) prevent from discontinuities in the rendered human model. Namely, the two imaginary cubes still share one surface, and the facets share one edge which means that the two facets will stay connected to each other.

Also the EFFD technique can be combined with the MC algorithm in the same manner as the FFD technique, preserving the continuity of the human model after the deformation. Any additional change of the existing algorithm is not necessary, because only the deformed position of the voxel is of interest, not the shape of the lattice to which the deformation is imposed.

Using this feature in “BodyFlex”, the user saves a lot of time until a satisfactory human model position is obtained. In few seconds the user can check the posture of the human model by using the feature and he/she can change its posture until the expected one is achieved. This prevents the user repeatedly to export the postured human model in a new dataset, which can take from a few seconds, up to several minutes for large human model datasets. Figure 3.7 shows some example postures of HUGO, Gustav and Laura.

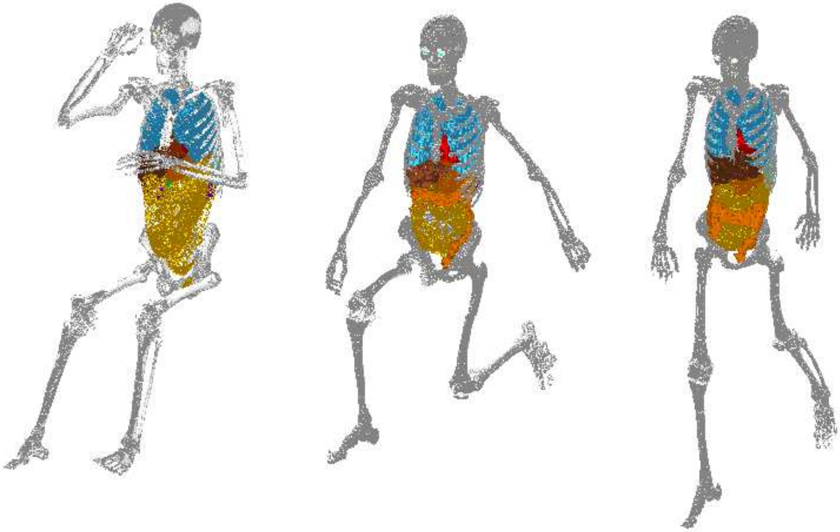

Figure 3.7.: HUGO (left), Gustav (middle) and Laura right in different postures

4 Time Domain Electromagnetic Field Simulation Algorithm

Within this dissertation, the influence of the electromagnetic fields on a set of voxel-based human body models is observed. Four physical laws that describe the time-varying electromagnetic fields are collected in a set of equations known as Maxwell's equations. These equations, that describe all macroscopic phenomena of electromagnetism are stated in the first section of this chapter.

Since the analytical solution of Maxwell's equations is not applicable for complex electromagnetic problems, using numerical methods to solve Maxwell's equations is more convenient. These methods are based on discretization of the computational domain and time to a set of discrete elements and discrete time instants. Later, the numerical solution is calculated for every spatial element at each time instant. Some of the well known numerical methods for solving Maxwell's equations are: Finite Integration Technique (FIT), Finite Volume Method (FVM), Finite Element Method (FEM) and Finite Difference Time Domain (FDTD). The second section of this chapter introduces the Finite Integration Technique for solving Maxwell's equations.

4.1 Maxwell's Equations

Macroscopic electromagnetic phenomena in continuous space are described using a set of four equations known as Maxwell's equations, named by James Clerk Maxwell. Maxwell's equations in integral form are expressed as follows:

$$\int_{\partial A} \vec{E}(\vec{r},t)\cdot \mathrm{d}\vec{s} \;=\; -\int_{A} \frac{\partial \vec{B}(\vec{r},t)}{\partial t}\cdot \mathrm{d}\vec{A} \tag{4.1}$$

$$\int_{\partial A} \vec{H}(\vec{r},t)\cdot \mathrm{d}\vec{s} \;=\; \int_{A} \Big(\frac{\partial \vec{D}(\vec{r},t)}{\partial t} + \vec{J}(\vec{r},t)\Big)\cdot \mathrm{d}\vec{A} \tag{4.2}$$

$$\int_{\partial V} \vec{D}(\vec{r},t)\cdot \mathrm{d}\vec{A} \;=\; \int_{V} \rho(\vec{r},t)\mathrm{d}V \tag{4.3}$$

$$\int_{\partial V} \vec{B}(\vec{r},t)\cdot \mathrm{d}\vec{A} \;=\; 0 \tag{4.4}$$

for any surface A with its boundary ∂A and volume V with its boundary ∂V. The electric field strength is denoted by $\vec{E}$, $\vec{H}$ denotes to the magnetic field strength, $\vec{B}$ the magnetic flux density, $\vec{D}$ the electric flux density, $\vec{J}$ the electric current density and ρ the electric charge density. The electric current density consists of three parts: conduction current density $\vec{J}_\kappa$, convection current density $\vec{J}_c$ and the impressed current density $\vec{J}_i$. The spatial variable is indicated by $\vec{r}$ and the temporal variable by t.

Equation 4.1 is known as Faraday's law and equation 4.2 as Ampère's law. These two equations bind the electric and magnetic field vectors along the boundary ∂A of a surface A with the electric, magnetic or current fluxes through the same surface. The last two equations, 4.3 known as Gauss' law and 4.4 known as Gauss' law of magnetism, connect the electric and magnetic flux over a closed surface ∂V of a volume V to the total charge within the same volume.

Maxwell's equations can be also expressed in differential form using the Stokes and the Gauss-Ostrogradsky theorem to the integral form [97][62]. Stokes' theorem connects the surface integral of the curl of a vector field over a surface A and the line integral of the vector field over the boundary of the same surface ∂A:

$$\int_{\partial A} \vec{F}\cdot \mathrm{d}\vec{s} = \int_{A} \nabla \times \vec{F}\mathrm{d}\vec{A} \tag{4.5}$$

Gauss-Ostrogradsky's theorem known also as Gauss' or divergence theorem reads:

$$\int_{\partial V} \vec{G} \cdot \mathrm{d}\vec{A} = \int_{V} \nabla \cdot \vec{G} \mathrm{d}V \tag{4.6}$$

Applying Stokes' theorem to the equations 4.1 and 4.2 and Gauss's theorem to the equations 4.3 and 4.4 and taking into account that the area A and the volume V in these equations are arbitrary, yields the differential form of Maxwell's equations:

$$\begin{aligned}
\nabla \times \vec{E}(\vec{r},t) &= -\frac{\partial \vec{B}(\vec{r},t)}{\partial t} && (4.7)\\
\nabla \times \vec{H}(\vec{r},t) &= \frac{\partial \vec{D}(\vec{r},t)}{\partial t} + \vec{J}(\vec{r},t) && (4.8)\\
\nabla \cdot \vec{D}(\vec{r},t) &= \rho(\vec{r},t) && (4.9)\\
\nabla \cdot \vec{B}(\vec{r},t) &= 0 && (4.10)
\end{aligned}$$

The connection between fields and fluxes in a material is given by the constitutive equations. The constitutive equations read:

$$\begin{aligned}
\vec{D}(\vec{r},t) &= \varepsilon_0 \vec{E}(\vec{r},t) + \vec{P}(\vec{r},t) && (4.11)\\
\vec{B}(\vec{r},t) &= \mu_0 \vec{H}(\vec{r},t) + \mu_0 \vec{M}(\vec{r},t) && (4.12)\\
\vec{J}_\kappa(\vec{r},t) &= \sigma(\vec{r}) \vec{E}(\vec{r},t) && (4.13)
\end{aligned}$$

where ε_0 is the permittivity of vacuum, μ_0 is the permeability of vacuum and σ is the conductivity of the medium. The vectors $\vec{P}$ and $\vec{M}$ are the polarization and magnetization field. The permittivity and permeability of a material are usually expressed relative to their values in vacuum:

$$\begin{aligned}
\mu(\vec{r}) &= \mu_0 \mu_r(\vec{r}) \quad , \quad \mu_0 = 4\pi \times 10^{-7} \mathrm{Vs/Am} && (4.14)\\
\varepsilon(\vec{r}) &= \varepsilon_0 \varepsilon_r(\vec{r}) \quad , \quad \varepsilon_0 = \frac{1}{\mu_0 c_0^2} \approx 8.854 \cdot 10^{-12} \mathrm{As/Vm} && (4.15)
\end{aligned}$$

where $c_0 \approx 2.998 \cdot 10^8$ m/s is the speed of light in vacuum.
In frequency domain computations, the electromagnetic fields have harmonic time dependence and oscillate at a certain frequency ω. Therefore, the electromagnetic

fields are represented by a complex-phasor vector which is independent of time. Since the dielectric properties of the human tissues are frequency dependent, they are also expressed using complex quantities. The constitutive equations for linear, homogeneous, isotropic, and dispersive materials read:

$$\begin{aligned} \underline{\vec{D}}(\vec{r}) &= \underline{\varepsilon}\underline{\vec{E}}(\vec{r}) && (4.16) \\ \underline{\vec{B}}(\vec{r}) &= \underline{\mu}\underline{\vec{H}}(\vec{r}) && (4.17) \\ \underline{\vec{J}}_{\kappa}(\vec{r}) &= \sigma(\vec{r})\underline{\vec{E}}(\vec{r}) && (4.18) \end{aligned}$$

where $\underline{\varepsilon}$ and $\underline{\mu}$ are given by:

$$\begin{aligned} \underline{\varepsilon} &= \varepsilon_0(\varepsilon_r' - j\varepsilon_r'') && (4.19) \\ \underline{\mu} &= \mu_0(\mu_r' - j\mu_r'') && (4.20) \end{aligned}$$

4.2 Finite Integration Technique

One of the numerical techniques for solving Maxwell's equations is the Finite Integration Technique (FIT), which was introduced by Weiland in 1977 [106]. Using this technique, many computational electromagnetic problems in different areas have been solved. Further research activities related to the Finite Integration Technique can be found in [24][102][93][99][107].

The first step towards solving Maxwell's equations is the discretization of the computational domain Ω into a computational grid G. This computational grid consists of individual non-overlapping grid cells, which can have arbitrary shape. In two-dimensional space, the computational domain is usually discretized with triangles or rectangles, while in three-dimensional space, hexahedral or tetrahedral volumetric cells are applied. This work deals with voxel-based human models, which perfectly match to a hexahedral Cartesian grid type. Therefore, the simulations performed during this work use a three-dimensional Cartesian grid.

A hexahedral grid consists of hexahedral elementary volumes (cells) V_n ($n = 1,...,N_V$) which are bounded by elementary faces (facets) A_n ($n = 1...N_A$). A hexahedral cell is bounded by six faces. Each facet has an orientation. The facets are bounded by edges L_n ($n = 1...N_L$). There are four edges that bound the facets of a hexahedral elementary volume. The edges are always bounded by two points which are known as nodes P_n $(n = 1 \ldots N_P)$. Figure 4.1 shows a hexahedral grid cell containing all the elementary geometric entities listed above.

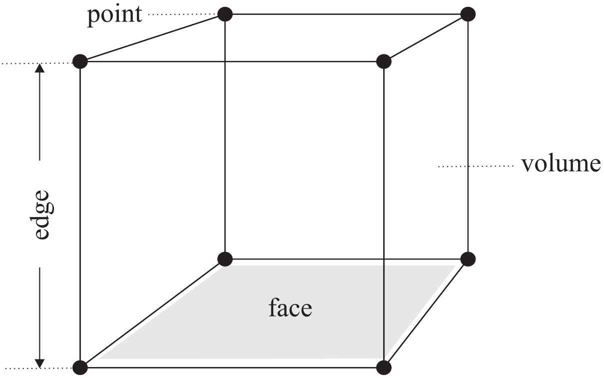

Figure 4.1.: Hexahedral grid cell

For discretization of Maxwell's equations, the Finite Integration Technique demands the usage of two grids: a primary grid G and a dual grid $\widetilde{G}$. In three-dimensional Cartesian space, the dual grid $\widetilde{G}$ is obtained from a translation of the first grid by half a mesh step in each of the three spatial directions. Each dual edge intersects a primary facet in its center and vice versa. Also each dual cell contains one primary point and vice versa. Regarding the relative orientation (indexes) of the entities, the oriented (indexed) dual entities have the same orientation (index) as the corresponding primary entities.

On the primary grid, two electromagnetic quantities are defined:

$$\widehat{e}_n = \int_{L_n} \vec{E} \cdot \mathrm{d}\vec{s} \tag{4.21}$$

$$\widehat{\widehat{b}}_n = \int_{A_n} \vec{B} \cdot \mathrm{d}\vec{A} \tag{4.22}$$

where $\widehat{e}_n$ are the electric voltages along the edges and L_n is the edge with number n. Magnetic fluxes through the facets are denoted by $\widehat{\widehat{b}}_n$ and A_n is the facet with number n.

On the dual grid, four electromagnetic quantities are defined:

$$\overset{\frown}{h}_n = \int_{\widetilde{L}_n} \vec{H}\cdot\mathrm{d}\vec{s} \tag{4.23}$$

$$\overset{\frown}{\overset{\frown}{d}}_n = \int_{\widetilde{A}_n} \vec{D}\cdot\mathrm{d}\vec{A} \tag{4.24}$$

$$\overset{\frown}{\overset{\frown}{j}}_n = \int_{\widetilde{A}_n} \vec{J}\cdot\mathrm{d}\vec{A} \tag{4.25}$$

$$q_n = \int_{\widetilde{V}_n} \rho\,\mathrm{d}V \tag{4.26}$$

where $\overset{\frown}{h}_n$ are the magnetic voltages along the dual edges and $\widetilde{L}_n$ is the dual edge with number n. Electric fluxes through the dual facets are denoted by $\overset{\frown}{\overset{\frown}{d}}_n$ and $\widetilde{A}_n$ is the facet with number n. The electric currents through the dual facets are represented by $\overset{\frown}{\overset{\frown}{j}}_n$. Finally, the electric charge in the dual cells is denoted by q_n where $\widetilde{V}_n$ is the dual cell with number n.

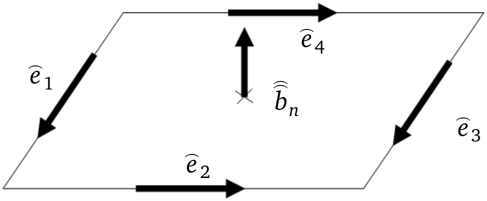

Figure 4.2.: Discretization of Faraday's law shown on a facet n

The discretization of Faraday's law is explained using Figure 4.2. The first step towards the discretization of Faraday's law, is writing the left-side integral on the boundary of the face as a sum of four integrals over the four edges (see equation 4.1). Each integral is actually a discrete electric voltage along the edge. This leads to the discretized form of Faraday's law on the given facet:

$$\overset{\frown}{e}_1 + \overset{\frown}{e}_2 - \overset{\frown}{e}_3 - \overset{\frown}{e}_4 = -\frac{\mathrm{d}}{\mathrm{d}t}\overset{\frown}{\overset{\frown}{b}}_n \tag{4.27}$$

The signs in front of the electric voltages are determined from the orientations of the edges.

Equation 4.27 is valid for all facets of the grid. Combining all the coefficients multiplying the discrete electric voltages (+1 and -1) in a matrix **C** and all the discrete electric voltages and magnetic fluxes in vectors $\widehat{\mathbf{e}}$ and $\widehat{\widehat{\mathbf{b}}}$ respectively, leads to the matrix form of Faraday's law discretized by FIT:

$$\mathbf{C}\widehat{\mathbf{e}} = -\frac{\mathrm{d}}{\mathrm{d}t}\widehat{\widehat{\mathbf{b}}} \tag{4.28}$$

The matrix **C** is the discrete equivalent of the curl operator. It is a topological matrix, because it describes the relationship between edges and facets in a grid G, i.e., which edge belongs to a certain facet and what is the relative orientation. If an edge belongs to a certain facet and has the same orientation as the facet, then the value of the respective element in the matrix is 1. If the orientation is opposite, then the value is set to -1. Otherwise, if the element does not belong to the face, the value of the respective element in the matrix is set to 0.

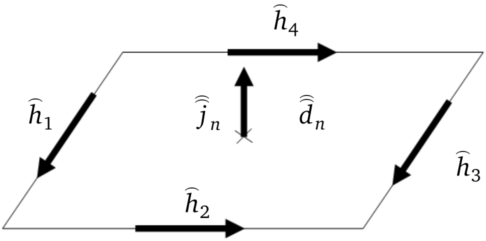

Figure 4.3.: Discretization of Ampère's law on a dual grid facet n

The second law from Maxwell's equations, Ampère's law, is discretized in a similar way as Faraday's law, but on the dual grid $\widetilde{G}$. The left-side integral from equation 4.2 is split into sum of four integrals along the dual grid edges as shown in Figure 4.3. Each integral is the discrete magnetic voltage along the respective edge. Ampère's law discretized using FIT reads:

$$\widehat{h}_1 + \widehat{h}_2 - \widehat{h}_3 - \widehat{h}_4 = \frac{\mathrm{d}}{\mathrm{d}t}\widehat{\widehat{d}}_n + \widehat{\widehat{j}}_n \tag{4.29}$$

Similarly as for Faraday's law, the matrix form of the Ampère's law discretized with FIT reads:

$$\tilde{\mathbf{C}}\hat{\mathbf{h}} = -\frac{\mathrm{d}}{\mathrm{d}t}\hat{\hat{\mathbf{d}}} + \hat{\hat{\mathbf{j}}} \tag{4.30}$$

where $\tilde{\mathbf{C}}$ contains the coefficients multiplying the discrete magnetic voltages. This matrix is again the discrete equivalent of the curl operator, but on the dual grid.

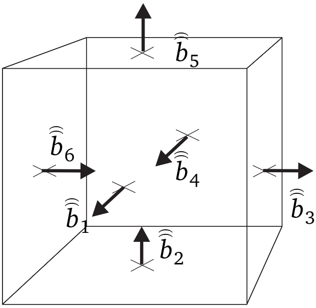

Figure 4.4.: Discretization of Gauss's law of magnetism on a primary grid cell

The discretization of Gauss's law of magnetism is performed on a cell of the primary grid, by splitting the left-hand side integral from equation 4.3 into six integrals on the six facets (Figure 4.4). Each integral on a facet is the discrete magnetic flux through that facet. The Gauss's law of magnetism discretized using FIT reads:

$$\hat{\hat{b}}_1 - \hat{\hat{b}}_2 + \hat{\hat{b}}_3 - \hat{\hat{b}}_4 + \hat{\hat{b}}_5 - \hat{\hat{b}}_6 = 0 \tag{4.31}$$

The matrix form of Gauss's law of magnetism reads:

$$\mathbf{S}\hat{\hat{\mathbf{b}}} = 0 \tag{4.32}$$

where the matrix **S** consists of the coefficients of the magnetic fluxes. The **S** is the discrete equivalent of the divergence operator on the primary grid.
In similar manner to Gauss's law of magnetism, the discretization of the left-hand side integral of Gauss's law is performed on a cell, but on the dual grid. The left-hand side integral is split into six integrals on the six faces (Figure 4.5). The Gauss's law reads:

$$\hat{\hat{d}}_1 - \hat{\hat{d}}_2 + \hat{\hat{d}}_3 - \hat{\hat{d}}_4 + \hat{\hat{d}}_5 - \hat{\hat{d}}_6 = q_n \tag{4.33}$$

The matrix form of Gauss's law reads:

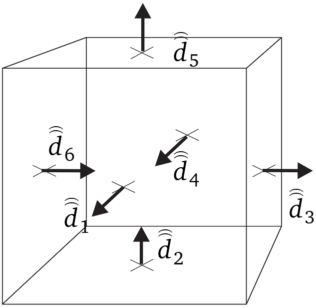

Figure 4.5.: Discretization of Gauss's law on a dual grid cell

$$\widetilde{\mathbf{S}}\widetilde{\widetilde{\mathbf{d}}} = \mathbf{q} \tag{4.34}$$

where $\widetilde{\mathbf{S}}$ is the discrete equivalent of the divergence operator on the dual grid. It consists of the coefficients of the electric fluxes.

The equations 4.28, 4.30, 4.32, and 4.34 are known as Maxwell's grid equations. Some of the basic properties of the topological matrices which are part of the equations above are the following.

$$\widetilde{\mathbf{C}} = \mathbf{C}^T \tag{4.35}$$

The first property from Eq. 4.35 connects the curl matrix on the dual grid with the transpose of the curl matrix on the primary grid.

The following properties, which originate from vector analysis, and consider the discrete equivalents of the divergence and the curl operators read:

$$\mathbf{SC} = 0, \quad \widetilde{\mathbf{S}}\widetilde{\mathbf{C}} = 0 \tag{4.36}$$

5 Positioning of General Voxel Human Models

This chapter explains the existing and the new functionalities of the posturing software "BodyFlex". A Graphical User Interface (GUI) is used to assist the user in the generation of different postures of human models. The main functions of "BodyFlex" are to import a non-deformed human model from a dataset file, deform the human model in different postures and export it in a new dataset file. As an intermediate step between the main functions, the user can render the original human model as well as the deformed one, before it is exported. In addition to the functions already introduced by Gao [44], other useful functions such as definition of joint points in the Voxel Model Observer (VMO) by Patrushev [85], automatic placement of the control lattices based on the positions of the joints, separation and movement of the fingers of the HUGO model are included in the software. New algorithms are introduced to improve some of the functionalities of "BodyFlex", such as algorithms for elbow deformation and improved export of the human models. In order to speed up the deformation and the export process, some parts of the software are enabled for parallel execution, which saves a lot of time especially for large human dataset files. Both deformation techniques implemented in "BodyFlex" are based on matrix manipulation to define the initial and calculate the deformed positions of the control points of the lattices based on the adjusted rotation angles.

The poser program "BodyFlex" was initially developed based on Microsoft Visual Studio 2008®. For the second version of the program, which includes the enhancements introduced in this thesis, it was upgraded to Microsoft Visual Studio 2010®. The program is written in the C++ language and has a GUI, which is developed with the MFC (Microsoft Foundation Class). Additional libraries are used to enable some specific functionalities, such as: OpenGL®libraries, for graphical representation of the human model and the simplified puppet, OpenMP®for parallelization of the code execution and TinyXml for parsing XML files. The program was developed on a Microsoft Windows 7®professional version operating system as a 64 bit (x64) application, but it can also run on a Windows Server 2008®and Windows Server 2012®.

This chapter is organized as follows: the first section describes the main and the optional functionalities of the "BodyFlex" which the user can manipulate. The second section explains the way of defining the joint points of a human model. In the third section, the principle of automatic placement of the control lattices based on the positions of the joints is described, supported by few examples. The movement of non-axis aligned body parts, the separation and the movement of the fingers of HUGO model and also the algorithm for elbow's movement are explained in the fourth section. An algorithm for fast export of human models is described in the fifth section, while in the last section the parallelization of the software and its benefits are presented.

5.1 Functionality and Scope of the Poser Program

Figure 5.1 shows all modules included in "BodyFlex". Below the figure each module is described separately.

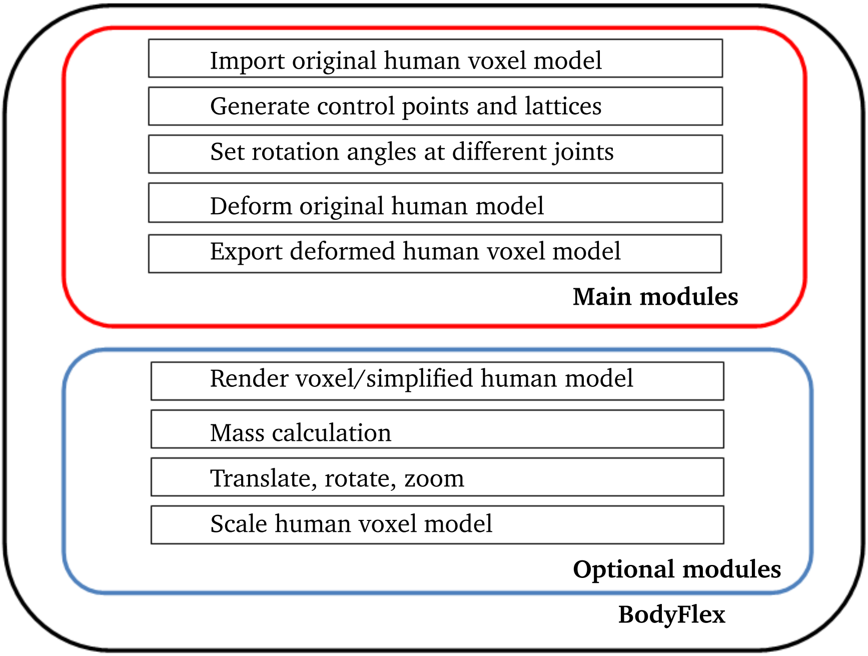

Figure 5.1.: Modules of "BodyFlex"

Import of human voxel model dataset file

The current version of “BodyFlex” allows import of three human voxel models: HUGO, Gustav and Laura. One of the three .vox files should be selected through the model selection dialog, shown in Figure 5.2. These files contain information about the human model names, their dataset size and resolution, as well as characteristics of the tissues at certain frequencies. As soon as the .vox file is selected, the cell size of the model should also be chosen from a drop-down list. Based on this input data, the appropriate human model dataset is loaded in “BodyFlex”.

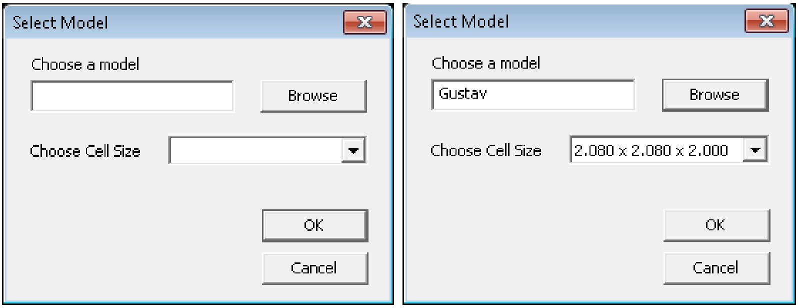

Choose a model

Choose Cell Size

Choose a model: Gustav

Choose Cell Size: 2.080 x 2.080 x 2.000

Figure 5.2.: Model selection dialog before (left) and after (right) selection of a human model

A human model dataset contains tissue IDs and has a dimension $X \times Y \times Z$, which is available in a .vox file. Gao [44] proposes two ways of storing the human model dataset: in a one-dimensional array and a three-dimensional array. The most intuitive way of storing the human model dataset when importing in “BodyFlex” would be a three-dimensional array with dimension $X \times Y \times Z$. This way of storing the human model dataset, which was initially used for HUGO, is also used for Gustav and Laura. Each element of the three-dimensional array is an object derived from a voxel class, which has the following member variables: voxel value (tissue ID), position of the voxel in 3D, and the body part ID to which the voxel belongs. This way of storage allows easy access to each element during the posture when the coordinates of each voxel should be recalculated.

Set rotation angles at different joints

After the human model is imported in “BodyFlex”, rotation angles at different joints can be set. To this aim, a simplified human model, which consists of geometrical forms (cylinders, spheres and elliptical cylinders) is used. Depending on the range and the direction of movement of the joint points, rotation angles around x,y and/or z - axis can be set. Figure 5.3 shows a dialog to set up the rotation angles in the respective directions using sliders.

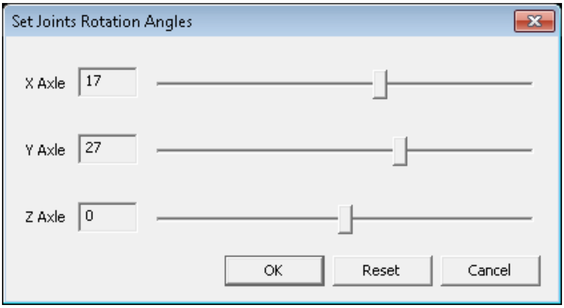

Figure 5.3.: Set joints rotation angles dialog

For the HUGO model, rotation angles of all joint points can be set, while for Gustav and Laura, the rotation of the fingers is not yet implemented. Therefore, the graphical representation of the simplified human model for HUGO differs from the one for Gustav and Laura, as shown in Figure 5.4.

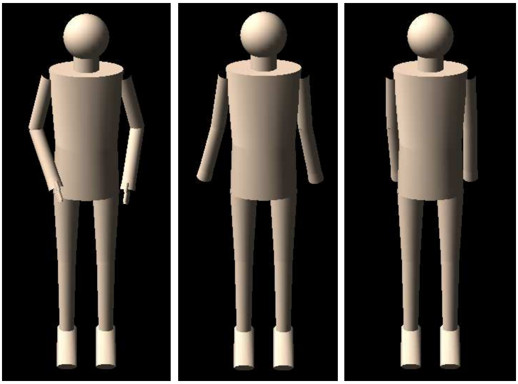

Figure 5.4.: Simplified human model used for deformation of HUGO (left), Gustav (middle), Laura (right)

The dimensions of the body parts of the simplified human model are chosen to relate to the ones in the voxel human model. This is achieved by calculating the distances between the joints. In order to have the same initial position of the simplified human model as the one of the human voxel model, the angles between the upper-arms and the fore-arms are considered.

Deform the original human model

The deformation of the human model depends on the rotation angles at the joints. After the user sets the rotation angles at the joints, the FFD or EFFD control lattices related to the joints are deformed. Then, the process of deforming the human model is started. During this process, new positions of the voxels are calculated. Usually this process takes from a few seconds to a few minutes, depending on the human model dataset size. If the user is not satisfied with the deformation, he can correct the rotation angles at the joints and again run the deformation process. This procedure can be repeated until the human model is postured satisfactorily. When this is achieved, the model can be exported for further usage.

Render the human model

After the model is imported in "BodyFlex", the user can see the model. By default the fat tissue of the human model is rendered with the MC algorithm and shown in the GUI. Also, the user has the possibility to choose other tissues to be shown, from a list of available tissues for the respective human model. Additionally, when the calculations in the deformation process are finished, the postured human model can be displayed in the GUI. This possibility is very useful, because the user can check the deformed model before it is exported. If the user is not satisfied with the resulting position, he can change it without exporting the human model and start the rendering functionality again. Since the export process is also time consuming, in this manner, the user saves a lot of time.

Export of deformed human model as a new dataset file

The human model can be exported as a new voxel dataset file in CST®voxel file format. The first version of "BodyFlex" had two different export functions: a slow one, which occupies less memory and a fast one with larger memory requirements. During this PhD work, an improved export function was developed, which is also fast, but with medium memory requirements. The principle of working of this function is described in section 5.5.

Mass calculation

This functionality allows the user to compare the mass of the deformed human body model with the mass of the original human model. The mass of all tissues from both models is calculated. Additionally, the relative error of the tissue masses of the deformed model referred to the original model is calculated.

Translate, rotate, zoom

The software has a list of commands that allow translation, rotation and zoom of the voxel-based and of the simplified human model, to enable the user to see the human model from different perspectives. This functionality also helps the user to set the rotation angles in an easier way.

Scale the human model

This functionality allows the user to scale the human model. It recalculates the joint point positions to fit to the scaling factor given by the user. Based on the new joints positions, all FFD lattices are rebuilt for further deformation of the human model. Scaling the human model is useful when some electromagnetic simulations should be performed with a child model and such a model is not available. Figure 5.5 shows the original and a scaled HUGO model.

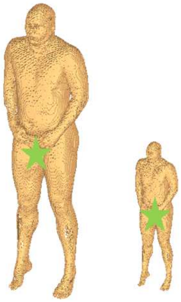

Figure 5.5.: Original and scaled HUGO model

5.2 Definition of Joint Points

Human body movements are closely related to, as well as dependent on the movements of the joints. Therefore, the positions of the joints need to be determined, in order to allow posing of the human models. The movements of the body parts in "BodyFlex" are related to the movement of joint points. For the HUGO model, a joint point can be defined at each joint of the original voxel model using the CST STUDIO SUITE ® [44]. In this manner, the positions of 14 joints and 6 help-joints, except the finger joints, are defined. Additional help-joints are defined in the patellas and at the end of the hands and feet in order to facilitate the placement of the control lattices needed for deformation of these body parts. The process of determination of the joint point positions in a 3D environment is time-consuming. Taking into account that each hand has 14 movable joints in the fingers, determination of the position of each of them in a 3D environment would be very time-consuming (one or two days), because the human models with the lowest resolution are considered. Therefore, the Voxel Model Observer (VMO) is used [85]. The VMO offers three cross-sectional views of the human body, in which the joint point position can be easily defined without rotating the whole human body to determine the right joint position in 3D space. Using VMO, all joints positions of a human model can be determined in a few hours. Figure 5.6 shows the graphical user interface of VMO.

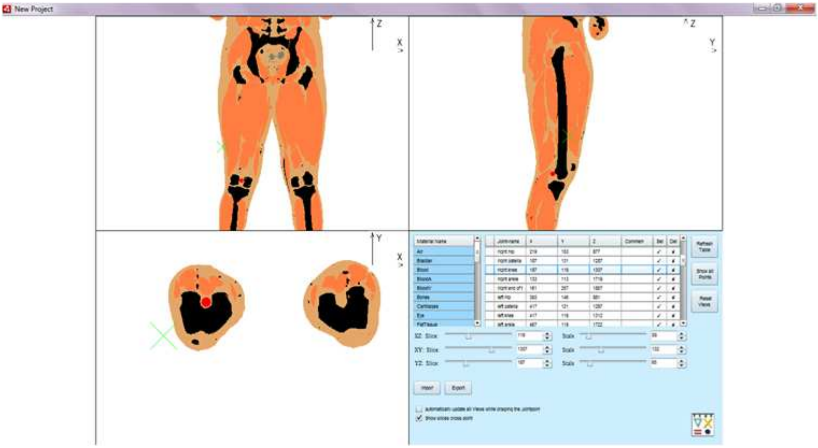

Figure 5.6.: Definition of a knee joint point in the Voxel Model Observer (VMO)

The workflow of the VMO is as follows:

Step 1: Import of a human voxel model
All three models, which are supported by the “BodyFlex” can be imported in the VMO.

Step 2: Definition of joint points or loading joint points from .xml file
The joint points can be easily placed in any of the three cross-sectional views by pressing the left mouse button. A red circle appears on the place where the joint point is defined. If the user is not satisfied with the location of the joint point in a certain cross-section, he/she can easily select the red circle and move it to the desired location. Then, the joint point will be automatically moved in all cross-sectional views.

The coordinates of the joint point are shown in a table, which is located in the right-down window. Additionally, the user can give a name of the joint point in the first column of the table. The VMO allows the user to choose one, several or all the tissues that should be rendered on the screen. If the user can not see the right cross-section where the joint point should be placed, he can use the appropriate slider to move between the slices. Also if the cross-section is too zoomed in or zoomed out, the user can use the appropriate slider to scale the current view. Another useful option in the VMO is to show all the joint points. Pressing the button with the same name, all the joint points will be drawn in all the cross sectional views. With this option, the user can see the approximate positions of the joints on the skeleton.

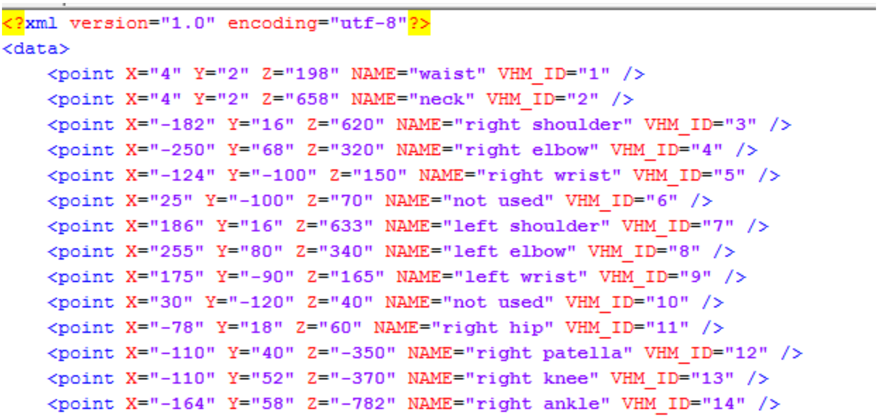

```
<?xml version="1.0" encoding="utf-8"?>
<data>
    <point X="4" Y="2" Z="198" NAME="waist" VHM_ID="1" />
    <point X="4" Y="2" Z="658" NAME="neck" VHM_ID="2" />
    <point X="-182" Y="16" Z="620" NAME="right shoulder" VHM_ID="3" />
    <point X="-250" Y="68" Z="320" NAME="right elbow" VHM_ID="4" />
    <point X="-124" Y="-100" Z="150" NAME="right wrist" VHM_ID="5" />
    <point X="25" Y="-100" Z="70" NAME="not used" VHM_ID="6" />
    <point X="186" Y="16" Z="633" NAME="left shoulder" VHM_ID="7" />
    <point X="255" Y="80" Z="340" NAME="left elbow" VHM_ID="8" />
    <point X="175" Y="-90" Z="165" NAME="left wrist" VHM_ID="9" />
    <point X="30" Y="-120" Z="40" NAME="not used" VHM_ID="10" />
    <point X="-78" Y="18" Z="60" NAME="right hip" VHM_ID="11" />
    <point X="-110" Y="40" Z="-350" NAME="right patella" VHM_ID="12" />
    <point X="-110" Y="52" Z="-370" NAME="right knee" VHM_ID="13" />
    <point X="-164" Y="58" Z="-782" NAME="right ankle" VHM_ID="14" />
```

Figure 5.7.: Definition of the joint points in .xml file

Step 3: Export of the joint points in .xml file
After a satisfactory placement of all the joint points, the user can export the joint points data in a .xml file. This file is later imported in “BodyFlex” together with the human model voxel dataset in order to allow the automatic placement of the initial control lattices. The structure of the .xml file which contains the joint points data is shown in Figure 5.7.

5.3 Automatic Placement of Control Lattices

The whole human model deformation process is guided by control lattices which are defined around the body parts. The manual definition of such control lattices for a variety of human body models is a very time-consuming process. Because the first version of “BodyFlex” implemented by Gao [44] concerned only HUGO, an enhancement was needed to allow automatic generation of the control lattices around almost all body parts, in order to generalize the usage of “BodyFlex”. As in the first version, the placement of the control lattices is based on the joint points positions. An exception is the elbow control lattice, which is defined semi-automatically because of the different initial position of this body part in different human models.
The first step towards the definition of the control lattices is to make a segmentation of the human body in such a way that almost each segment includes one joint

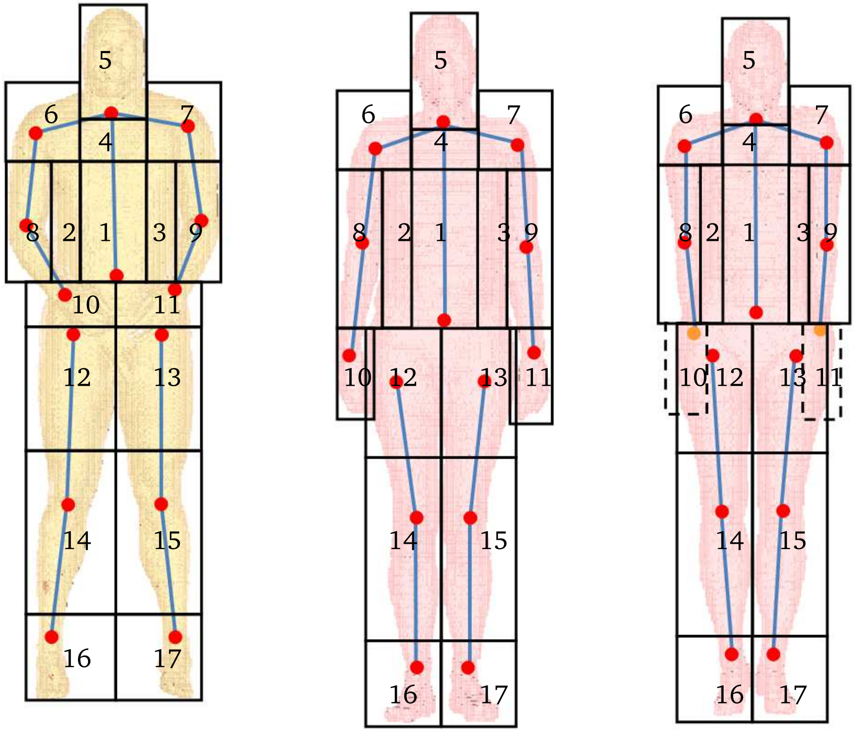

Figure 5.8.: Segmentation of the human models HUGO, Gustav and Laura based on the joints positions

point (denoted by a red circle in Figure 5.8). Later, in each segment, one or several control lattices are defined. Based on the segmentation of HUGO, initially introduced by Gao [44], the segmentation of the three human body models is shown in Figure 5.8.

Although in Figure 5.8 all human models are segmented into 17 body parts, HUGO has an additional segmentation of the fingers which is explained later in section 5.4.2. Even though in Figure 5.8 all body parts appear precisely segmented, there are some of them that actually overlap. Such body parts are 2 and 8, as well as body parts 3 and 9. Also body part 10 overlaps body part 12 and body part 11 overlaps body part 13. Therefore, an additional algorithm was implemented by Gao [44], to distinguish between voxels that belong to the trunk and voxels that belong to the arm in the HUGO model. Namely, the arms of the HUGO model were segmented in five parts. However, the initial position of the arms of Gustav and Laura do not require such detailed segmentation as HUGO. The arms of these two human models are divided in two segments, one containing the upper arm and half of the forearm, and the other one containing the lower part of the forearm and the hand.

Control lattice around the head

Body part number 5 from the previously shown segmentation corresponds to the head which can be moved by the neck joint. To deform the head only one FFD control lattice is defined. The most intuitive way to define this control lattice is to create a box from 3D planes. Four planes can be immediately defined in the following way: plane 1 passes through the neck joint and has a normal vector $\vec{n}_1 = (0,0,1)$; plane 2 is parallel to plane 1 with normal vector $\vec{n}_2 = -\vec{n}_1$ and passes through the highest voxel in z-direction; plane 5 has a normal vector $\vec{n}_5 = (0,-1,0)$ and passes through the last back voxel in y-direction; plane 6 is parallel to plane 5 with a normal vector $\vec{n}_6$ opposite to vector $\vec{n}_5$ and passes through the first front voxel in y-direction. Two more planes, 3 and 4 need to be defined. Let us first define plane 3. The first step is to calculate the middle point M between the neck joint and the highest voxel in z-direction. Starting from point M an air voxel is searched in negative x-direction. When such voxel is found, a plane is created at that position. This plane should not contain any voxel filled with tissue different than air. Therefore a rectangle is created from the intersection of this plane with planes 1, 2, 4 and 5. This rectangle is divided in two other rectangles, upper and lower one, and only the upper one is investigated, so that the voxels belonging to the torso are excluded from the investigation. This rectangle is moved further in negative x-direction if it contains at least one voxel which is not filled with air. Otherwise, plane 3 is defined from one of the voxels that lie on the rectangle and the normal vector $\vec{n}_3 = (1,0,0)$. As soon as plane 3 is defined, the plane 4 is defined symmetrically to the point M in opposite direction, with vector $\vec{n}_4 = (-1,0,0)$. All normal vectors defined above point to the inside of the box. In Figure 5.9 left, the two planes 3 and 4, which are colored in blue, should be defined, while in Figure 5.9 right, plane 3 is created.

When the box is created, a control lattice with 36 control points split in 4 layers, each containing 3 x 3 control points is defined in the following way: the box is first split in two parts along the x-axis, such that the 3/4 of the volume belong to the upper box and the rest belongs to the lower box. The lower box is additionally split in two equal boxes along the x-axis, because the deformation occurs in the middle of the lower box. Then the control points are defined at each layer. The control points on the top and bottom of the box border are obtained with an intersection

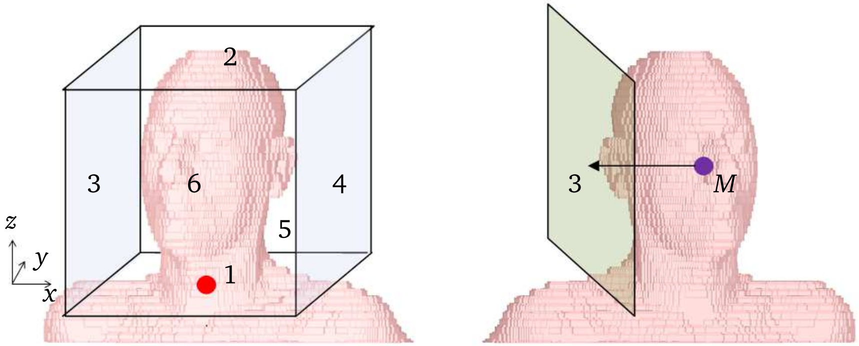

Figure 5.9.: Six planes around the head to define a box(left) and definition of plane 3 (right)

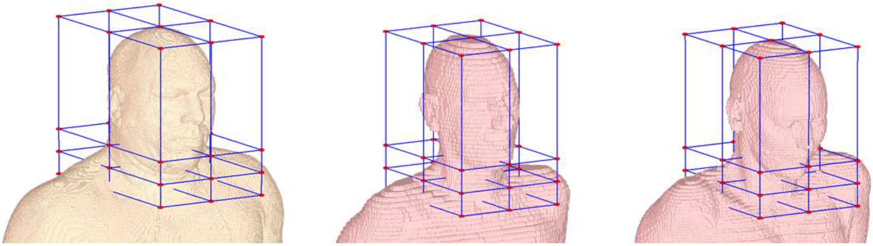

Figure 5.10.: FFD control lattices around heads

between the planes which define the box. The rest control points on one layer are calculated as middle control points of the border control points. All the control points positions in the two middle layers in the box are obtained by shifting the control points in the bottom layer at a certain distance in z-direction. Finally the FFD control lattice around the head is defined. Figure 5.10 shows the control lattices around the head of Hugo, Gustav and Laura, defined using the algorithm described above.

Control lattice around the hip

Body part 12 includes the upper part of the leg (thigh) and the lower part of the abdomen. The thigh is moved by the hip joint. In this body part, two FFD control lattices are defined: one controlling the movement of the leg and other protecting the tissues in the pelvis from movement. Both FFD control lattices have 4 layers, each with 3 x 3 control points. Here an example for the definition of lattices around the right hip is given. The FFD control lattices of the left hip are defined in the same manner.

At first, the FFD control lattice around the thigh is defined. The same process of definition of a box as for the head is conducted. The top plane (plane 1) is defined at the waist joint height. The bottom plane (plane 2) is defined at a point above the knee. Plane 5 and 6 are defined as by the head, at the most back and the most front point, respectively. Also plane 2 is defined in the same way as by the head (finding rectangle containing only air voxels). The plane 3 is defined at a point which is placed in positive x-direction away from the right hip joint, at 1/20 of the distance between the hip joints.

Since the box is defined now, the control points can be also calculated. There are 36 control points split in 4 layers, each containing 3 x 3 control points. At first, the box is split in two parts along the x-axis, such that a little bit less than half of the volume belongs to the upper box and the rest belongs to the lower box. The hip joint which guides the movement of the leg is in the upper box. Therefore this box is split in two equal boxes along x-axis. After all four layers are defined, the border control points are calculated as intersections between the layers and the planes defining the box. The points in the middle of the lattice are calculated from the middle between two border control points, which lie in same layer.

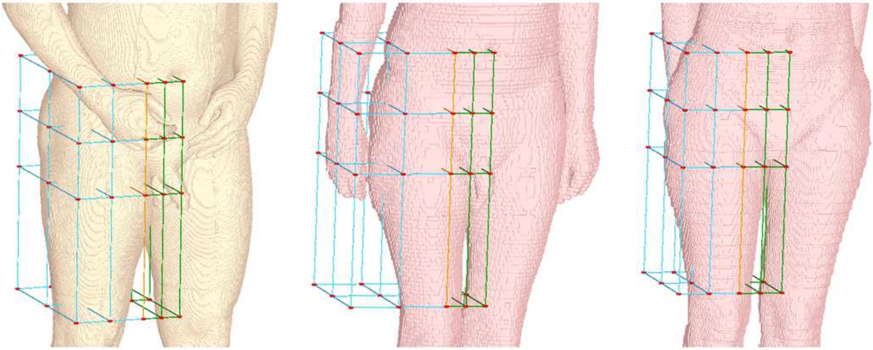

Figure 5.11.: FFD control lattices right upper leg

Next, the second FFD control lattice is defined. Planes 1,2,4 and 5 are the same as at the thigh box. Because the two FFD control lattices are placed one next to the other, they share same face, which means that plane 3 defined at the thigh box is plane 2 at the second box, with a normal vector in opposite direction to the one at plane 3. At last, plane 3 is defined in the middle point between the two hip joints. The 36 control points that build the second FFD control lattice are defined in the same manner as the one at the thigh FFD control lattice. The only difference between these two lattices is that the control points at the second FFD control lattice, which belong to the upper box are static, so that the tissues in the pelvis are not moved. Figure 5.11 shows the two control lattices defined on the three human models. The blue one is the thigh FFD control lattice, while the second one is colored in green. The face that the both FFD control lattices share is in orange.

5.4 Movement of Human Body Parts

Within the first version of the “BodyFlex” application, not all parts of the body could be deformed. Exceptions were the wrist and finger movements which require a change in the implemented deformation algorithm because of the position of the forearm and the hand of the HUGO model. These body parts are bent on the lower part of the abdomen.

Two enhancements of the “BodyFlex” application are introduced in this thesis, which are connected to each other. The first enhancement is the algorithm for movement of non-axis aligned body parts, which is developed because of the above mentioned non-standard initial position of the forearm and hand of the HUGO model. The author discusses this enhancement in [104]. The second enhancement is the numerical approach for the separation and movement of the fingers of the HUGO model. This approach allows generation of a proper posture of the hand of the HUGO model. First, an algorithm is developed to geometrically separate the fingers and distinguish between the voxels that belong to each finger. Later, non-axis aligned control lattices are placed around the fingers to cope with their initial position. The author published this approach in [105].

5.4.1 Movement of Non-axis Aligned Body Parts

In the first version of the “BodyFlex” wrist movements were not possible. The forearm and the hand of HUGO were embedded in one FFD control lattice, as it is shown on Figure 5.12 left, which could not be deformed. In realistic electromagnetic simulation scenarios, sometimes the possibility for bending the wrist and also the fingers is important. Therefore it is necessary to embed these body parts in separated FFD control lattices. Moreover, the FFD control lattice on Figure 5.12 left is aligned to the global coordinate system axes, which does not fit to HUGO’s initially bended forearm and wrist.

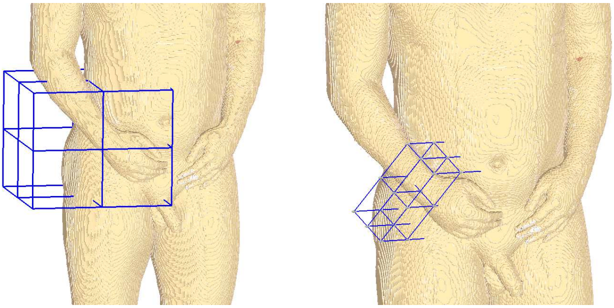

Figure 5.12.: Old version (left) and new version (right) of the FFD lattices for the wrist

The first enhancement of “BodyFlex” is shown in Figure 5.12 right. The initially rotated FFD control lattice in which the wrist is embedded allows rotation and movement of the wrist, not in the direction of the global coordinate system axes, but in the direction of the rotated coordinate system axes which are defined along the FFD control lattices. The position of a control point or a voxel data point in the rotated coordinate system of the lattice is obtained using the well known direction cosine matrix. This matrix, which is used for transformation from one to another coordinate system is defined as follows:

$$\mathbf{R} = \begin{bmatrix} \cos\theta_{x'x} & \cos\theta_{x'y} & \cos\theta_{x'z} \\ \cos\theta_{y'x} & \cos\theta_{y'y} & \cos\theta_{y'z} \\ \cos\theta_{z'x} & \cos\theta_{z'y} & \cos\theta_{z'z} \end{bmatrix}. \tag{5.1}$$

where θ is the angle between the global coordinate system axis x, y or z and the axis x', y' or z' of the rotated coordinate system, respectively (Figure 5.13). The transformation (rotation, translation) of the FFD control lattices could be performed around or along axes aligned with the global coordinate system, but it could result in an unnatural deformation. Therefore, the movement of this body part should be performed around or along axes of the rotated coordinate system, which is aligned to the wrist. The axes of the rotated coordinate system are treated as arbitrary axes in 3D space and the rotation of this body part should is performed around these axes[15].

Rotation around an arbitrary axis differs from the rotation around the Cartesian coordinate axes. Figure 5.14 shows an arbitrary axis defined as a line between two

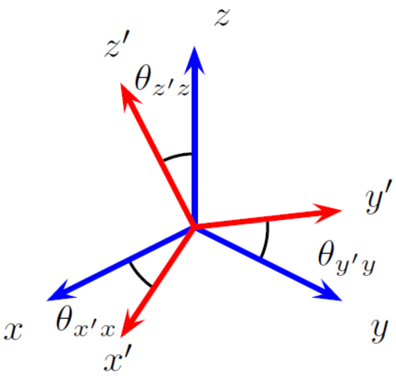

Figure 5.13.: Global and rotated coordinate systems

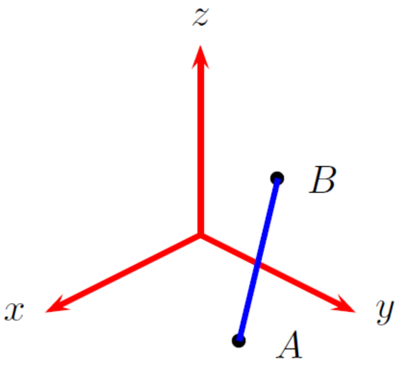

Figure 5.14.: An arbitrary axis between the points A and B

points $A(x_1, y_1, z_1)$ and $B(x_2, y_2, z_2)$. Rotation of a point in 3 dimensional space by angle θ around the given arbitrary axis can be achieved in a few steps.

Step1 Translation of A so that the rotation axis passes through the origin

In order for the rotation axis to pass through the origin as shown on Figure 5.15, the point A should be translated by $-A(-x_1, -y_1, -z_1)$. To accomplish this step, a translation matrix **T** should be used.

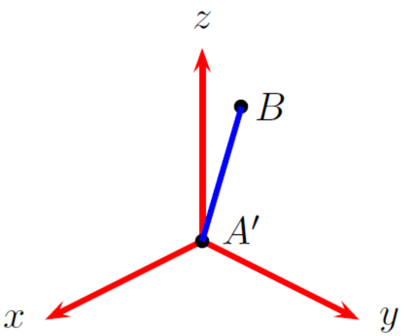

Figure 5.15.: Translation of A to the origin

$$\mathbf{T} = \begin{bmatrix} 1 & 0 & 0 & -x_1 \\ 0 & 1 & 0 & -y_1 \\ 0 & 0 & 1 & -z_1 \\ 0 & 0 & 0 & 1 \end{bmatrix} \tag{5.2}$$

Step2 Rotation around the x-axis so that the rotation axis lies in the xz plane

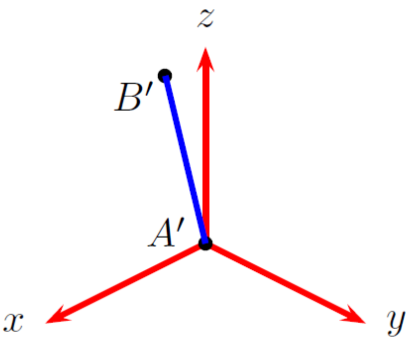

Figure 5.16.: Rotation around x-axis until B lies on xz plane

The first step towards placing the rotation axis in the xz plane (see Figure 5.16) is the definition of a unit vector $\vec{n} = (n_x, n_y, n_z)$ along the rotation axis and $d = \sqrt{n_y^2 + n_z^2}$, which is the length of the projection of the rotation axis on the yz plane.

The rotation angle α is the angle between the z-axis and the projection of the rotation axis on the yz plane. The rotation matrix $\mathbf{R}_x$ which describes this rotation has the cosine and the sine of the angle as elements. They can be calculated using the following formulas:

$$\cos(\alpha) = n_z/d, \quad \sin(\alpha) = n_y/d \tag{5.3}$$

$$\mathbf{R}_x = \begin{bmatrix} 1 & 0 & 0 & 0 \\ 0 & n_z/d & -n_y/d & 0 \\ 0 & n_y/d & n_z/d & 0 \\ 0 & 0 & 0 & 1 \end{bmatrix} \tag{5.4}$$

Step3 Rotation around the y-axis so that the rotation axis lies along the z-axis
For this purpose the rotation matrix $\mathbf{R}_y$ is used, whose sine and cosine elements are n_x and d respectively. This step is shown on Figure 5.17.

$$\mathbf{R}_y = \begin{bmatrix} d & 0 & -n_x & 0 \\ 0 & 1 & 0 & 0 \\ n_x & 0 & d & 0 \\ 0 & 0 & 0 & 1 \end{bmatrix}, \tag{5.5}$$

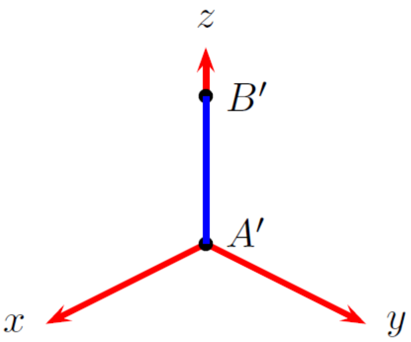

Figure 5.17.: Rotation around y-axis until B lies along the z-axis

Step4 Perform the desired rotation by θ around the z axis
The last forward step is the desired rotation around the z axis by an angle θ. The rotation matrix $\mathbf{R}_z$ describes this step which is shown on Figure 5.18.

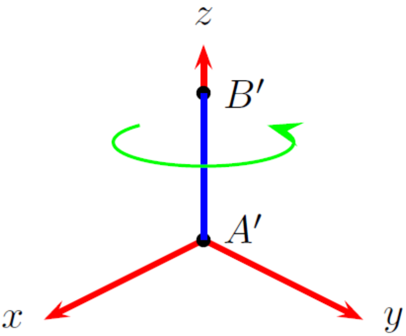

Figure 5.18.: Rotation around z-axis

$$\mathbf{R}_z = \begin{bmatrix} \cos(\theta) & 0 & -\sin(\theta) & 0 \\ \sin(\theta) & 0 & \cos(\theta) & 0 \\ 0 & 0 & 1 & 0 \\ 0 & 0 & 0 & 1 \end{bmatrix} \tag{5.6}$$

Step5 Inverse of steps 3, 2 and 1

The last step of the rotation around an arbitrary axis is to apply an inverse of steps 3, 2 and 1 respectively, to bring the arbitrary axis in its initial position.

The transformation steps to rotate a point $P_1(x_1, y_1, z_1)$ around the rotation axis to a new point $P_2(x_2, y_2, z_2)$ can be described by the following equation:

$$\begin{pmatrix} x_2 \\ y_2 \\ z_2 \\ 1 \end{pmatrix} = \mathbf{T}^{-1}\mathbf{R}_x^{-1}\mathbf{R}_y^{-1}\mathbf{R}_z\mathbf{R}_y\mathbf{R}_x\mathbf{T} \begin{pmatrix} x_1 \\ y_1 \\ z_1 \\ 1 \end{pmatrix} \tag{5.7}$$

In Eq. (5.7), the translation of the point P_1 is performed by first using the translation matrix $\mathbf{T}$, then the rotation matrices $\mathbf{R}_{x,}\mathbf{R}_{y,}\mathbf{R}_z$. Later, the inverse rotation matrices $\mathbf{R}_y^{-1}$ and $\mathbf{R}_x^{-1}$ are applied and finally the inverse translation matrix $\mathbf{T}^{-1}$ is used.

Using the following example, written by the author in [104] [105], the transformation of the position of a voxel data point P with Cartesian coordinates (x_1,y_1,z_1) is explained. This voxel point belongs to the wrist and it is located in the FFD control lattice of the wrist. Because the movement of the voxel point depends on the movement of the wrist and HUGO's wrist is not aligned to the Cartesian coordinate system axes, a second coordinate system attached to the FFD control lattice on the wrist is considered, with a center in a point $O(a, b, c)$. The goal is to determine the position of the voxel point (x_2, y_2, z_2) in the Cartesian coordinate system after rotation and translation of the point with respect to the coordinate system attached to the FFD control lattice.

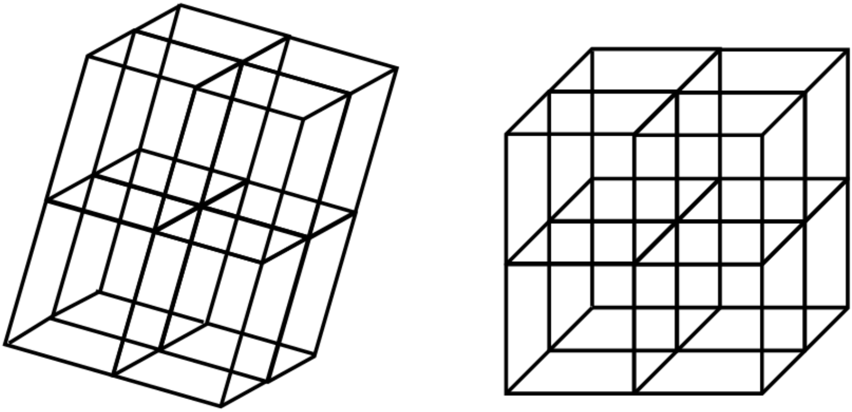

Figure 5.19.: Initial rotated FFD control lattice (left) and unit cube which represents the local FFD control lattice (right)

The first step is to map the FFD control lattice onto a unit cube as shown on Figure 5.19. Each control point of the FFD control lattice is mapped to one vertex on the unit cube. First, the direction cosine matrix $\mathbf{R}$ is used to describe the position of the FFD control lattice points with respect to the Cartesian coordinate system. Additionally, the dimensions of the FFD control lattice in the three directions, denoted as ℓ_x, ℓ_y and ℓ_z are necessary for the transformation. There are 27 control points distributed in three dimensional matrix with dimensions $3x3x3$, denoted by $\mathbf{C}$ which describe the FFD control lattice. The control points mapped on the unit cube, which actually represent local coordinates, are denoted with $\mathbf{C}'$. The transformation is described in Eq. 5.8:

$$\begin{pmatrix} \mathbf{C}'_{ijk}(x) \\ \mathbf{C}'_{ijk}(y) \\ \mathbf{C}'_{ijk}(z) \end{pmatrix} = \begin{pmatrix} \mathbf{C}_{ijk}(x) - a \\ \mathbf{C}_{ijk}(y) - b \\ \mathbf{C}_{ijk}(z) - c \end{pmatrix} \cdot \mathbf{R} \cdot \begin{pmatrix} \ell_x^{-1} \\ \ell_y^{-1} \\ \ell_z^{-1} \end{pmatrix} \tag{5.8}$$

where $0 < i, j, k < 3$. The same equation is used to determine the position of the point $P(x_1, y_1, z_1)$ in the local coordinate system $P'(x'_1, y'_1, z'_1)$. The terms $\mathbf{C}'$ and $\mathbf{C}$ are replaced with P' and P respectively, as described in Eq. 5.9.

$$\begin{pmatrix} x'_1 \\ y'_1 \\ z'_1 \end{pmatrix} = \begin{pmatrix} x-a \\ y-b \\ z-c \end{pmatrix} \mathbf{R} \begin{pmatrix} \ell_x^{-1} \\ \ell_y^{-1} \\ \ell_z^{-1} \end{pmatrix} \tag{5.9}$$

After the FFD control points and the voxels embedded in this FFD control lattice are transformed in local coordinates, the new position of the point P' is calculated by the deformation function used in the FFD technique. This function is defined by a trivariate tensor product Bernstein polynomial. The position of the voxel in local coordinates $(x_2^{'},y_2^{'},z_2^{'})$ after applying the deformation function is given by:

$$\vec{P}'_{x'_2 y'_2 z'_2} = \sum_{i=0}^{2}\sum_{j=0}^{2}\sum_{k=0}^{2} B_i^2(x'_1) B_j^2(y'_1) B_k^2(z'_1) C'_{ijk}, \tag{5.10}$$

where B_i^2, B_j^2, B_k^2 are the Bernstein polynomials of second order and $\mathbf{C}'$ is the matrix which contains the local coordinates of the control points of the FFD control lattice. Finally, the position of the voxel data point $P(x_2, y_2, z_2)$ is determined in the Cartesian coordinate system. Therefore the inverse of the direction cosine matrix is used. Eq. 5.11 calculates the position of the voxel data point embedded in the deformed FFD control lattice:

$$\begin{pmatrix} x_2 \\ y_2 \\ z_2 \end{pmatrix} = \begin{pmatrix} a \\ b \\ c \end{pmatrix} + \mathbf{R}^{-1} \begin{pmatrix} x'_2 \cdot \ell_x \\ y'_2 \cdot \ell_y \\ z'_2 \cdot \ell_z \end{pmatrix} \tag{5.11}$$

5.4.2 Separation and Movement of the Fingers of HUGO Model

Until this development, the “BodyFlex” did not allow the movement of the fingers. The movement of the fingers is also important for investigating the effects of electromagnetic fields on the human body. Algorithms for finger movement have already been introduced in computer graphics and computer animation. Moccozet proposed the Dirichlet Free Form Deformation (DFFD) [75], which can be used for deformation of hands and fingers of human models. This technique uses a Dirichlet-Voronoi tessellation for a set of arbitrary control points. Algorithms successfully used to deform the human hand are [72], [68], [89], [65], [75].

The first obstacle towards the movement of the fingers of HUGO is the missing skin layer between the fingers in the original HUGO model, which should be a natural boundary between the fingers. Therefore it was necessary to develop a geometrical algorithm for finger separation, which can determine which voxel belongs to which finger. Around each finger, hexahedrons are created such that each hexahedron contains voxels only from one finger.

Separation of the Fingers

Before the algorithm for separation of the fingers is described, the terminology used in this algorithm is explained. The fingers on each hand are named as shown on Figure 5.20: thumb, index, middle, ring and pinky. There are in total 14 movable joints in the fingers on each hand. They are split in three categories as shown on Figure 5.21. In order to limit the area of each finger, one more point, threated as a joint which does not move, is defined at the end of each finger. In total the number of joints defined for all the fingers on each hand is 19.

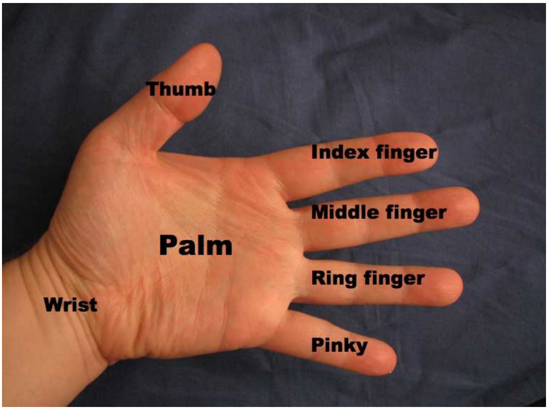

Figure 5.20.: Hand parts and their names [28]

In Figure 5.22, the bones of the right hand are shown. The example given below is used by the author in [105] to explain the algorithm for separating the fingers. The relevant joints for describing the separation of the fingers are marked by points denoted by *MD*, *RD*, *ID*, *MM*, *MR* and *MU*.

The middle finger is the first finger on which the separation algorithm is performed. Starting with the joint point *MM* and the normal vector $\vec{a}$, oriented from *MM* to *MD*, the first plane is created. In the next step, a second plane between the middle and

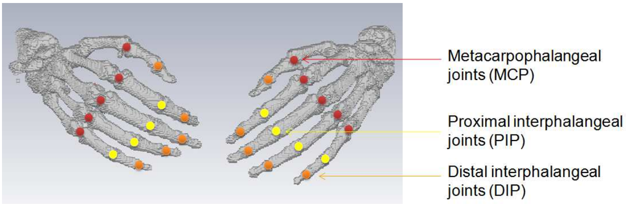

Figure 5.21.: Movable joints in the fingers of both hands

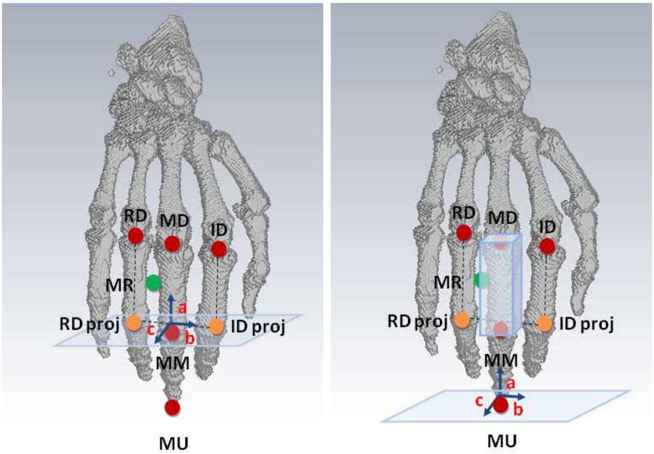

Figure 5.22.: Definition of the planes for separation of the upper part(left) and the lower part(right)

the ring finger should be created. To this aim, several vectors were tested until the most suitable one was chosen for creating the plane. Namely, the vector, denoted by $\vec{b}$ was created by projecting the joint points *RD* and *ID* on the first plane, denoted by *RDproj*, *IDproj* in Figure 5.22 left and with an orientation *RDproj* to *IDproj*. Then a third plane is created which is parallel to the second one and passes through the middle point *MR*, between the upper parts of the middle and the ring finger. Two more planes, in front and back, are created in the following way: first, the normal vector $\vec{c}$ is obtained from the cross product of the vectors $\vec{a}$ and $\vec{b}$. Then, a search along this vector is performed in the both directions, to find the "first" and the "last" voxel of the hand, through which the two planes are created. The last plane to build the hexahedron is the plane created from the lower part of the FFD control lattice around the wrist.

The same vectors are used to create a hexahedron for the lower part of the middle finger. A plane is created through the point *MU* with a normal vector $\vec{a}$ oriented from *MU* to *MM*. The same planes used from the left, the right and the bottom side of the upper hexahedron are used as a left, right and upper plane for the lower hexahedron. Two new planes in front and back of the middle finger are created in the same manner as for the upper hexahedron. After the voxels of the middle finger are embedded in both hexahedrons, the same algorithm is used to define the two hexahedra which surround the ring finger. These hexahedra are shown on Figure 5.23.

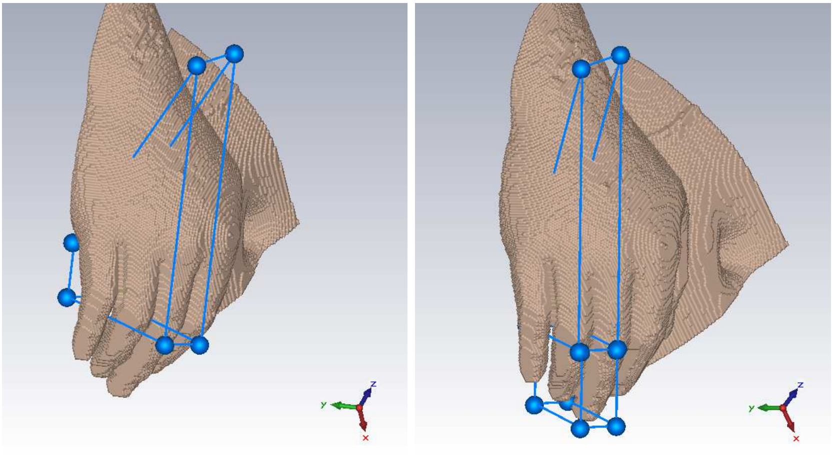

Figure 5.23.: Hexahedra for separating the ring finger

The same algorithm is applied to the pinky finger, with one additional examination. Since the pinky finger is the last finger from the hand, it is necessary to determine the boundary plane from the left side. To this aim, a search along the vector $\vec{b}$ in the opposite direction is performed, starting from the joint point *PD*, which lies left from the joint *RD*. The search allows to determine the "last" voxel in the given direction and belonging to the hand. Through this voxel, the left boundary plane is constructed, with the direction vector $\vec{b}$.

For the index finger, the determination of the vectors to create a hexahedron differs from the middle, ring and the pinky finger. All the vectors remain the same, except the vector $\vec{b}$ which is oriented from the finger joint *ID* to the *MD*. Additionally, for the thumb finger, the vector $\vec{c}$ has an orientation, which coincides with the unit vector of the Cartesian coordinate system in y direction.

The movement of the fingers is controlled by the FFD control lattices which are aligned with the fingers. These lattices, similar to the lattices around the wrists, are rotated with respect to the global coordinate system to cope with the position of the body parts embedded in them. There are 5 FFD control lattices for the thumb and 7 FFD control lattices for each of the rest fingers which control the movement of the fingers. The FFD lattices have an orientation based on the vectors $\vec{a}$, $\vec{b}$ and $\vec{c}$ determined during the separation process. Additionally, the left and the right boundary planes from the FFD control lattices for a certain finger from index to ring finger are defined through joints of the fingers next to the given finger. For example, the right boundary plane of the FFD lattice of the ring finger passes trough the *MM* joint of the middle finger (Figure 5.22). Each lattice has 3 layers and 27 control points. In Figure 5.24, the FFD control points around the ring and the index finger are shown.

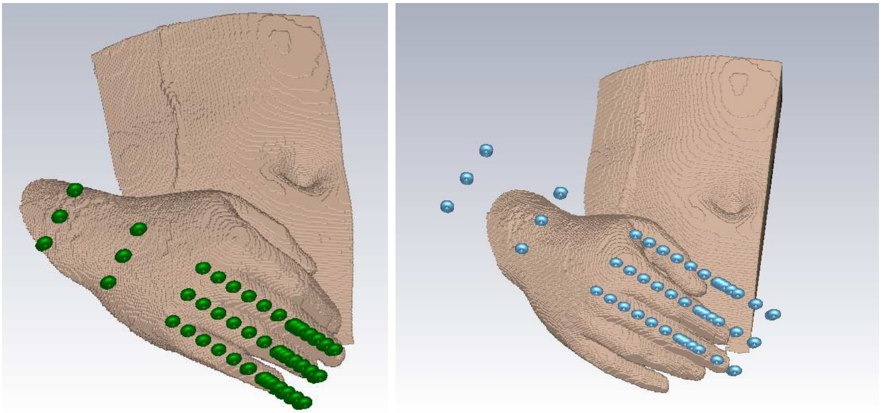

Figure 5.24.: FFD control points for movement of the ring finger (left) and index finger (right)

The algorithm for moving and deforming of the fingers does not differ from the algorithm for moving the wrist, described in Section 5.4.1. Even though the FFD lattices of two neighboring fingers can overlap, the FFD deformation algorithm runs without any problem because the deformation is applied only to the voxels that belong to a certain finger, not to all voxels embedded in the FFD lattice. Also the continuity of the tissues between the roots of the fingers and the hand is preserved during the deformation process, because all FFD lattices around the fingers have the same upper plane, which is the same as the lower plane of the FFD lattice of the wrist.

5.4.3 Elbow Movement

The elbow deformation of HUGO is a specific problem. The arm is not in a straight position, and the FFD control lattice, aligned with the global coordinate system axes, is not a good choice for deforming the elbow. One approach for definition of FFD lattice for this body part could be the initially rotated FFD lattice, but in this case it would not fit to the actual form of this body part, which is bent. Another approach is to use the Extended Free Form Deformation technique (EFFD) which is based on the Free Form Deformation, but allows the use of arbitrary shaped non-axis aligned hexahedrons. In this particular case, the EFFD lattice has the form of a decahedron, that is built from two merged arbitrary hexahedrons, in which the elbow is embedded. The transformed form of the arbitrary shaped decahedron to the local coordinates is again a unit cube, which is the same shape as in the original FFD. However, obtaining the coordinates of a certain point which is moved in an arbitrary formed EFFD lattice demands many transformations. At first, the mapping of the decahedron to a unit cube is not straightforward as in the case for the rotated parallelepiped FFD lattice. The decahedron is separated in two hexahedrons and each hexahedron is mapped on half of the unit cube. In the next subsection, the mapping of a hexahedron to a unit cube is explained in detail.

Elbow Deformation Algorithm

In this subsection, the algorithm for elbow deformation is described. As already mentioned earlier in this chapter, the initial form of the EFFD lattice for the elbow consists of two irregular hexahedrons which are merged together and form a decahedron. The first transformation is the transformation of the global coordinates (x, y, z) of the initial form in local coordinates (m, n, p). Figure 5.25 shows the EFFD control lattice in form of a decahedron and the cube to which the decahedron is mapped. The decahedron represents one EFFD lattice made of 3 layers and 27 control points (as shown on Figure 5.25 (left)).
Eight points are taken into consideration during the calculation of the $\boldsymbol{\alpha}, \boldsymbol{\beta}$ and $\boldsymbol{\gamma}$ coefficients explained in section 3.3.1. The decahedron is mapped on a cube within the range [0-1] in m, n and p direction. First the decahedron is split into two hexahedrons. Each of these hexahedrons is mapped on a parallelepiped, corresponding to half of the cube. The eight points considered for calculating the coefficients $\boldsymbol{\alpha}, \boldsymbol{\beta}$ and $\boldsymbol{\gamma}$ are the eight vertices from the corners of the hexahedron,

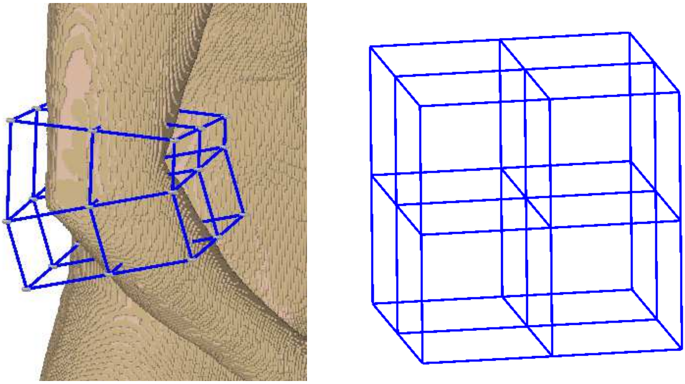

Figure 5.25.: Decahedron around the elbow (left) and cube (right)

i.e the parallelepiped. The first parallelepiped occupies the range [0-1] in m and n direction and [0-0.5] in p direction, while the second one occupies the same range in m and n direction, but the range [0.5-1] in p direction. Therefore we have two 8x8 matrices, $\mathbf{M}_1$ within the range [0,0,0]-[1,1,0.5] and $\mathbf{M}_2$ within the range [0,0,0.5]-[1,1,1]. The unit cube has 3 layers and 27 control points, the same as the decahedron. Each layer represents a 9-node quadrilateral. The local coordinates of the points are saved in a three dimensional matrix $\mathbf{B}$. Knowing the eight control points from the eight corners of the hexahedron, i.e parallelepiped, all the other 19 points can be easily obtained once the coefficients $\boldsymbol{\alpha}, \boldsymbol{\beta}$ and $\boldsymbol{\gamma}$ are calculated, using the following formulas

$$\begin{cases} \boldsymbol{\alpha}_1 = \mathbf{M}_1^{-1}\mathbf{x}_1 \\ \boldsymbol{\beta}_1 = \mathbf{M}_1^{-1}\mathbf{y}_1 \\ \boldsymbol{\gamma}_1 = \mathbf{M}_1^{-1}\mathbf{z}_1 \end{cases} \tag{5.12}$$

$$\begin{cases} \boldsymbol{\alpha}_2 = \mathbf{M}_2^{-1}\mathbf{x}_2 \\ \boldsymbol{\beta}_2 = \mathbf{M}_2^{-1}\mathbf{y}_2 \\ \boldsymbol{\gamma}_2 = \mathbf{M}_2^{-1}\mathbf{z}_2 \end{cases} \tag{5.13}$$

The movement of the elbow part is controlled by a transformation matrix with dimension 4 x 4 which is already used by Gao [44], to control the movement of the other body parts. This matrix keeps the current position of a certain joint with respect to its initial position. Here, all the previous transformations (movements) of the joints on which depends the current joint position are taken into account. For the transformation of the elbow part, the values of the transformation matrix at the elbow joint are needed.

The transformation matrix is built as a product of a rotation and a translation matrix. It includes coordinates of a point, represented by homogeneous coordinates (using four values to represent a 3D point). In the current implementation of "BodyFlex", the first three values of the homogeneous coordinates are the x, y and z coordinates and the fourth coordinate has a value 1. The rotation matrix $\mathbf{R}_{xyz}$ is a product of the rotation matrices $\mathbf{R}_x$, $\mathbf{R}_y$ and $\mathbf{R}_z$ in x, y and z direction. Since the transformation matrix has dimension 4 x 4, the rotation matrices will also have a dimension 4 x 4. The reason why homogeneous coordinates are used is to represent a translation as a matrix multiplication operation. The translation is used to set the rotation center in a point different than $(0,0,0)$. The rotation matrices are defined as:

$$\mathbf{R}_x = \begin{bmatrix} 1 & 0 & 0 & 0 \\ 0 & \cos(\theta_x) & -\sin(\theta_x) & 0 \\ 0 & \sin(\theta_x) & \cos(\theta_x) & 0 \\ 0 & 0 & 0 & 1 \end{bmatrix}, \mathbf{R}_y = \begin{bmatrix} \cos(\theta_y) & 0 & \sin(\theta_y) & 0 \\ 0 & 1 & 0 & 0 \\ -\sin(\theta_y) & 0 & \cos(\theta_y) & 0 \\ 0 & 0 & 0 & 1 \end{bmatrix},$$

$$\mathbf{R}_z = \begin{bmatrix} \cos(\theta_z) & 0 & -\sin(\theta_z) & 0 \\ \sin(\theta_z) & 0 & \cos(\theta_z) & 0 \\ 0 & 0 & 1 & 0 \\ 0 & 0 & 0 & 1 \end{bmatrix}$$

If the cos is denoted by c and the sin is denoted by s, the rotation matrix $\mathbf{R}_{xyz}$ has the following form:

$$\mathbf{R}_{xyz} = \begin{bmatrix} c(\theta_y)c(\theta_z) & -c(\theta_y)s(\theta_z) & s(\theta_y) & 0 \\ s(\theta_x)s(\theta_y)c(\theta_z) + c(\theta_x)s(\theta_z) & -s(\theta_x)s(\theta_y)s(\theta_z) + c(\theta_x)c(\theta_z) & -s(\theta_x)c(\theta_y) & 0 \\ -c(\theta_x)s(\theta_y)c(\theta_z) + s(\theta_x)s(\theta_z) & -c(\theta_x)s(\theta_y)s(\theta_z) + s(\theta_x)c(\theta_z) & c(\theta_x)c(\theta_y) & 0 \\ 0 & 0 & 0 & 1 \end{bmatrix} \tag{5.14}$$

The $\mathbf{R}_{xyz}$ matrix is then multiplied with a translation matrix which keeps the current position of the elbow joint, denoted by el_c. This translation matrix has the following form:

$$\mathbf{T} = \begin{bmatrix} 1 & 0 & 0 & el_c(x) \\ 0 & 1 & 0 & el_c(y) \\ 0 & 0 & 1 & el_c(z) \\ 0 & 0 & 0 & 1 \end{bmatrix} \tag{5.15}$$

The transformation matrix **RT** is obtained by multiplication of the matrix $\mathbf{R}_{xyz}$ with the matrix **T**:

$$\mathbf{RT} = \mathbf{R}_{xyz}\mathbf{T} \tag{5.16}$$

The positions of the control points on the EFFD lattice after the movement are obtained in the following way. The distance in m, n and p direction is calculated, between the center of rotation (in this case are the initial local coordinates of the elbow joint, denoted by el) and the initial local values of the points from which the decahedron is built (defined in the matrix **C**). Matrix **C** is a three dimensional matrix which contains the initial local coordinates of all 27 control points, from which the EFFD lattice for the elbow is built. The initial local coordinates have values in the interval $[0, 0, 0]$ to $[1, 1, 1]$. Then a translation matrix **TL** is built for each of the 27 points from **C**, which has the following form:

$$\mathbf{TL} = \begin{bmatrix} 1 & 0 & 0 & \mathbf{C}_{ijk}(m) - el(m) \\ 0 & 1 & 0 & \mathbf{C}_{ijk}(n) - el(n) \\ 0 & 0 & 1 & \mathbf{C}_{ijk}(p) - el(p) \\ 0 & 0 & 0 & 1 \end{bmatrix} \tag{5.17}$$

where $i, j, k \in N$ and $i, j, k \in [1, 3]$. Then **RT** and **TL** matrices are multiplied and a new matrix called **RTT** is obtained.

$$\mathbf{RTT} = \mathbf{RT} \cdot \mathbf{TL} \tag{5.18}$$

There are three **RT** matrices for each layer of the EFFD control lattice of the elbow. This is due to the movement of the elbow joint. Namely the upper layer is always fixed, the middle layer is moved for half of the angle of rotation and the lower layer is moved for the full angle of rotation. In order to keep the proper values of the control points after the rotation, these three transformation matrices have to be considered. The matrix elements from the last column of the RTT matrix give the local coordinates of a deformed control point. All the local coordinates of the deformed control points, are stored in a 3 x 3 x 3 matrix named **LC**, where $i, j, k \in N$ and $i, j, k \in [1, 3]$.

$$\begin{cases} \mathbf{LC}_{ijk}(x) = RTT(1,4) \\ \mathbf{LC}_{ijk}(y) = RTT(2,4) \\ \mathbf{LC}_{ijk}(z) = RTT(3,4) \end{cases} \tag{5.19}$$

Knowing the local coordinates of the deformed control points, the deformed position of each point that is inside the decahedron can be obtained. Let us assume a point F which is inside the decahedron. Using the Newton method, first the point F is transformed from the initial global coordinates (x, y, z) to the initial local coordinates (m, n, p) in the hexahedron to which it belongs. For the given decahedron, which is separated in two hexahedrons (upper and lower one), two systems of trilinear equations, two Jacobian matrices and two initial guesses are defined. For the upper hexahedron, the middle point $(0.5, 0.5, 0.25)$ is chosen as an initial guess, while for the lower hexahedron its middle point $(0.5, 0.5, 0.75)$ is chosen. Having the initial local coordinates of F, a deformation function defined by a trivariate tensor product Bernstein polynomial is used to find the deformed position F' of the point F. In this case the Bernstein basis polynomials of second order are used.

$$\vec{F}'(m_1, n_1, p_1) = \sum_{i=0}^{2}\sum_{j=0}^{2}\sum_{k=0}^{2} B_i^2(m)B_j^2(n)B_k^2(p)\mathbf{LC}_{ijk}, \tag{5.20}$$

The deformed position of a point F in the local coordinate system is F'. To go back to the global coordinates of the deformed (moved) point F', the following algorithm should be used. Because it is not possible to perform a mapping of the deformed cube (with coordinates in **LC**) on the deformed EFFD lattice directly, both are first mapped on a unit cube. In this case, the deformed cube is treated as a decahedron, built from two merged arbitrary shaped hexahedrons. This decahedron is transformed to a unit cube as described above, when the initial EFFD lattice of the elbow is transformed to the unit cube. Since the coordinates of the points of the deformed cube (**LC**) and the coordinates of the vertices of a unit cube are known, the transformation coefficients $\boldsymbol{\alpha}_3, \boldsymbol{\beta}_3$, and $\boldsymbol{\gamma}_3$ for the upper hexahedron and $\boldsymbol{\alpha}_4, \boldsymbol{\beta}_4$, and $\boldsymbol{\gamma}_4$ for the lower hexahedron can be calculated. The eight points from the upper hexahedron are stored in vectors $\mathbf{x}_3$, $\mathbf{y}_3$ and $\mathbf{z}_3$, while for the lower hexahedron they are stored in vectors $\mathbf{x}_4$, $\mathbf{y}_4$ and $\mathbf{z}_4$. The same matrices with dimensions 8 x 8 containing the initial coordinates of the upper i.e lower parallelepiped ($\mathbf{M}_1$ and $\mathbf{M}_2$ respectively) are used for calculating the coefficients of both hexahedrons.

$$\begin{cases} \boldsymbol{\alpha}_3 = \mathbf{M}_1^{-1}\mathbf{x}_3 \\ \boldsymbol{\beta}_3 = \mathbf{M}_1^{-1}\mathbf{y}_3 \\ \boldsymbol{\gamma}_3 = \mathbf{M}_1^{-1}\mathbf{z}_3 \end{cases} \tag{5.21}$$

$$\begin{cases} \boldsymbol{\alpha}_4 = \mathbf{M}_2^{-1}\mathbf{x}_4 \\ \boldsymbol{\beta}_4 = \mathbf{M}_2^{-1}\mathbf{y}_4 \\ \boldsymbol{\gamma}_4 = \mathbf{M}_2^{-1}\mathbf{z}_4 \end{cases} \tag{5.22}$$

The same transformation procedure is performed for the global deformed (moved) EFFD lattice, which also has a decahedral shape. Since the coordinates of the control points of the deformed (moved) lattice and the coordinates of the points of the unit cube are known, the coefficients $\boldsymbol{\alpha}_5, \boldsymbol{\beta}_5$, and $\boldsymbol{\gamma}_5$ for the upper hexahedron and $\boldsymbol{\alpha}_6, \boldsymbol{\beta}_6$, and $\boldsymbol{\gamma}_6$ for the lower hexahedron are calculated.

$$\begin{cases} \boldsymbol{\alpha}_5 = \mathbf{M}_1^{-1}\mathbf{x}_5 \\ \boldsymbol{\beta}_5 = \mathbf{M}_1^{-1}\mathbf{y}_5 \\ \boldsymbol{\gamma}_5 = \mathbf{M}_1^{-1}\mathbf{z}_5 \end{cases} \tag{5.23}$$

$$\begin{cases} \boldsymbol{\alpha}_6 = \mathbf{M}_2^{-1}\mathbf{x}_6 \\ \boldsymbol{\beta}_6 = \mathbf{M}_2^{-1}\mathbf{y}_6 \\ \boldsymbol{\gamma}_6 = \mathbf{M}_2^{-1}\mathbf{z}_6 \end{cases} \tag{5.24}$$

Then the Newton method is applied to determine the coordinates of the point F' in the cube. The (m_1, n_1, p_1) coordinates and the $\boldsymbol{\alpha}_3, \boldsymbol{\beta}_3$, and $\boldsymbol{\gamma}_3$ or the $\boldsymbol{\alpha}_4, \boldsymbol{\beta}_4$, and $\boldsymbol{\gamma}_4$ coefficients are used depending on the hexahedron to which the point belongs. The initial guess for the Newton method is set to $(0.5, 0.5, 0.25)$ for the upper hexahedron and $(0.5, 0.5, 0.75)$ for the lower hexahedron. After the coordinates of the point $F'(m_2, n_2, p_2)$ in the cube are obtained, a vector $\mathbf{D}$ is assembled with the following elements:

$$\mathbf{D} = \begin{bmatrix} 1 & m_2 & n_2 & p_2 & m_2n_2 & n_2p_2 & m_2p_2 & m_2n_2p_2 \end{bmatrix} \tag{5.25}$$

The vector $\mathbf{D}$ is multiplied with the transformation coefficients $\boldsymbol{\alpha}_5, \boldsymbol{\beta}_5$, and $\boldsymbol{\gamma}_5$ for the upper hexahedron or $\boldsymbol{\alpha}_6, \boldsymbol{\beta}_6$, and $\boldsymbol{\gamma}_6$ for the lower hexahedron, depending

on where the point is located in the cube and the final global coordinates of the deformed point are obtained.
Figure 5.26 shows examples of elbow movements of the three human models Hugo, Laura and Gustav.

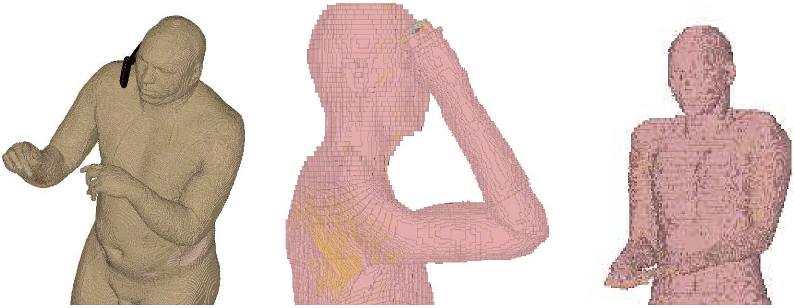

Figure 5.26.: Elbow movement of Hugo, Gustav and Laura

5.5 Algorithm for Fast Export of Human Models

During the export process, the export dataset, which consists of tissue IDs, is built based on the voxel positions of the deformed human model. At the beginning, the dimensions of the new dataset are calculated [44]. As the position of each voxel is available, the minimum and maximum position values are considered to calculate the dimension in each direction of the new dataset using the following formula:

$$EX = \frac{X_{max} - X_{min}}{\Delta X} + 2, \tag{5.26}$$

where ΔX is the voxel dimension in x-direction. The formula shows the calculation of the new dimension in x-direction. The same formula is used for calculation of the new dimension in y- and z-direction taking the respective minimum and maximum position values as well as the voxel dimension. Adding 2 at the end of the equation is to ensure that there will not be any voxel placed outside of the calculated dimension value.
The export dataset is built by voxelization of the whole space with the previously calculated dimensions, using a regular mesh of identical cubes or parallelepipeds. Figure 5.27 is used for further explanation. On the left side, the initial dataset with dimensions IX, IY and IZ is shown. This dataset is obtained by voxelizing the whole

space defined by the dimensions of the human model in initial position. During the voxelization process, voxels with dimensions Δx, Δy and Δz are created. Each voxel is represented by one dataset element, which consists of: position of the voxel in 3D space (center of the voxel), tissue ID and body part ID to which the voxel belongs.

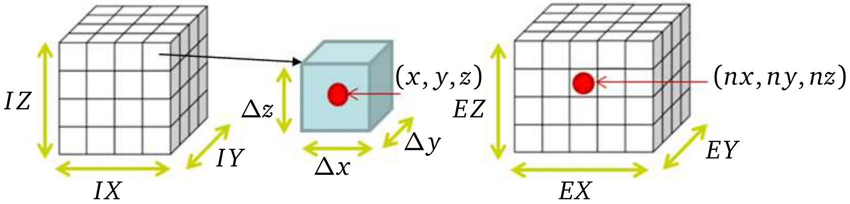

Figure 5.27.: Initial (left) and export (right) dataset and voxel (middle)

With the voxelization of the deformed model space, voxels with the same dimension as in the initial dataset (Δx, Δy and Δz) are created. The same characteristics of the voxels as the one in the initial dataset are stored in the export dataset. Each voxel in the export dataset should be assigned with one tissue ID. However, the decision which tissue ID should be assigned to the voxel is not straightforward. When the human model is deformed, the initial position of the voxel changes. All the voxels from the initial dataset should be mapped in the export dataset, based on their current position. Since the dimensions of the export dataset are known, the mapping of the voxels is as follows:

$$nx = \frac{(x + \frac{EX\Delta x}{2} + \frac{\Delta x}{2})}{\Delta x}, \quad ny = \frac{(y + \frac{EY\Delta y}{2} + \frac{\Delta y}{2})}{\Delta y}, \quad nz = \frac{(z + \frac{EZ\Delta z}{2} + \frac{\Delta z}{2})}{\Delta z} \tag{5.27}$$

where x, y, z are the current position coordinates of a voxel from the initial dataset and nx, ny, nz are the indices of that voxel in the export dataset. Since the only information necessary for the export is the tissue ID, the export dataset is represented by an array and the 1D voxel index np corresponding to the three indices of the dataset element is calculated by:

$$np = nx + nyEX + nzEXEY \tag{5.28}$$

It might happen that more than one voxel from the initial dataset has the same *np* index, resulting in a voxel with several tissue IDs in the export dataset(as shown in Figure 5.28 (right)). In this case, the decision which tissue ID should be assigned to the voxel is based on finding the most often occurring tissue ID in that voxel using the sub-division algorithm proposed by Gao [44].

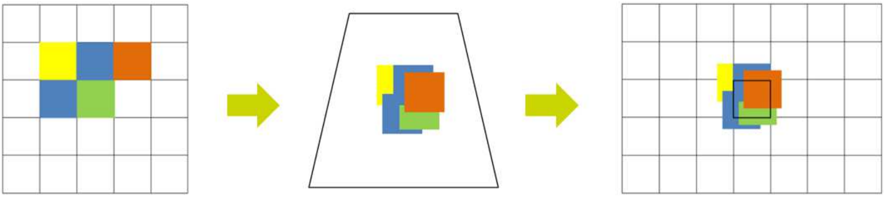

Figure 5.28.: Overlapping voxels after deformation: voxels in initial position (left), during the deformation (middle) and after voxelization of the space for export

Also with the deformation of the human model, some neighboring voxels in the initial dataset might be separated in the export dataset. When mapping these voxels in the export dataset some empty voxel/voxels can occur between them. Because the human body cannot have any tissue discontinuities, these empty voxels should be also assigned with a proper tissue ID. Gao proposed a compensation algorithm to deal with this problem [44]. This algorithm is also used in this new implementation of the export function.

Although the sub-division algorithm gives satisfactory results, an improvement was required. In order to optimize the time for export of a deformed model and the memory occupation, a new algorithm based on sparse matrices techniques is proposed.

The fastest algorithm proposed by Gao stored the occurrence of a certain tissue ID in a matrix which had as many rows as the number of the available tissues for the given human model plus 2 and as many columns as the export dataset size ($EX \times EY \times EZ$). For example the Hugo model has 32 different tissues and the matrix created had 34 rows. A visual representation of the matrix is shown in Figure 5.29.

In Figure 5.29, the 1D voxel index in the export array is denoted with np and the tissue ID is denoted by T_{ID}.

Since not all tissue IDs can occur in one voxel, most of the data kept in the matrix is redundant. Therefore, this sparse matrix is stored in compressed form by the new algorithm. Four different arrays are built, two with the export dataset size and two with the initial dataset size. The first one has the export dataset size and stores

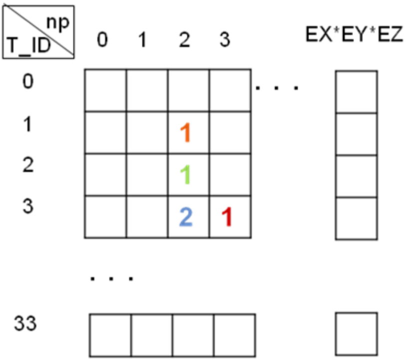

Figure 5.29.: Matrix for the tissue ID occurrences in voxels

the occurrence of the 1D voxel index *np*. The second one of the same size stores the tissue ID at *np*. If *np* occurs only once in the first array, the proper tissue ID is stored in the second one at index *np*. Otherwise, if *np* occurs several times in the first array, zero is stored in the second array at index *np*. At the same time, *np* is stored in the third array and the corresponding tissue ID is stored in the fourth array. Figure 5.30 shows one part of the described arrays and their content.

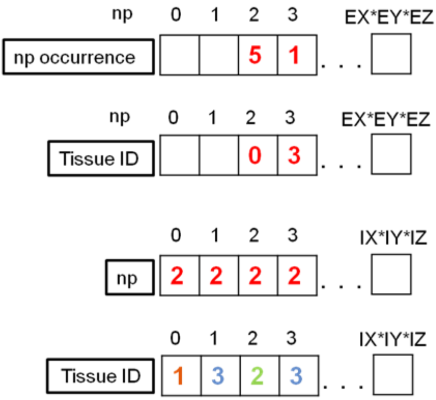

Figure 5.30.: Definition of several arrays to obtain the occurrence of tissue ID in a voxel

For example, from Figure 5.30, $np = 3$ occurs only once in the first array and the proper tissue ID (3) is stored in the second array at $np = 3$. However, $np = 2$ occurs five times and therefore zero is written at $np = 2$ in the second array. At the same time, $np = 2$ is written five times in the third array and the correspondent tissue IDs which are located at $np = 2$ are stored in the fourth array.

When all the voxels from the initial set are mapped to voxels in the new dataset, a Quick Sort algorithm is run to sort the pairs (np,Tissue ID) from the third and fourth array in ascending order of np. The Quick Sort algorithm is introduced by Hoare in [51]. Later, an algorithm is run to count and delete the duplicate pairs (np,Tissue ID) and save the counted value in a new array. This is how the sparse matrix is built and saved in a compressed form. The array index from the newly created array, with the maximum value related to a certain np gives the array index of the most occurring tissue ID.

Then tissue IDs are assigned to the empty voxels within the human body using the compensation algorithm introduced by Gao [44].

Figure 5.31 and 5.32 show the memory consumption of the "BodyFlex" to export a deformed human model and the time only for exporting the human model, respectively, using the old (Export 1) and the new (Export 2) export function.

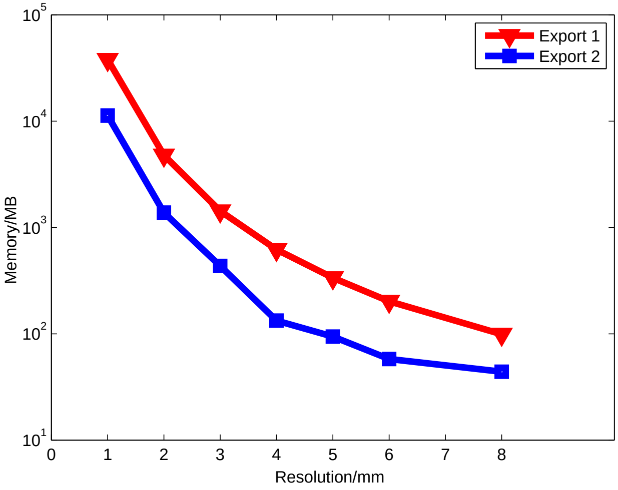

Figure 5.31.: Memory consumption to export deformed human model

The new export function proposed here occupies three times less memory and works twice faster than the old one. This results in a lot resource and time saving especially when large human model datasets are used.

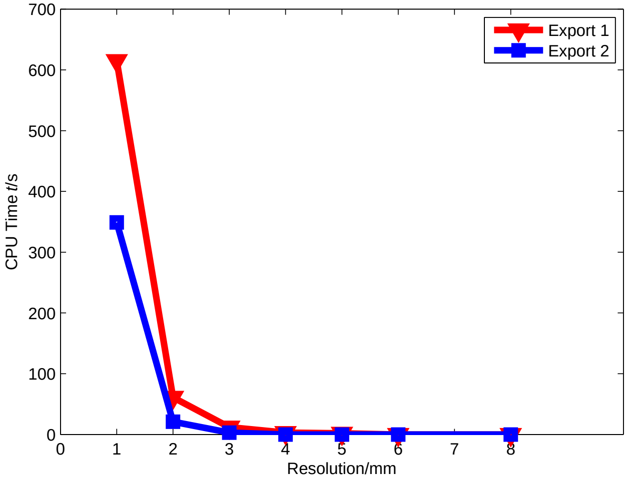

Figure 5.32.: Time to export deformed human model

5.6 Parallelization of the Poser Program

The first version of “BodyFlex” worked only on one CPU core. Since most of the program code allowed independent execution, it was parallelized to work on multiple CPUs using OpenMP®. OpenMP®(Open Multi-Processing) is an application programming interface (API) which offers directives to be included in code written in C, C++ or Fortran and usually only requires a minimal modification of the code, to allow its parallel execution on a multicore computer using a shared memory [18]. As the basic principle of working of OpenMP is multithreading, the program or parts of the program which should be executed in parallel is/are then split between threads, each running on a separate CPU and having access to the shared memory.

For test purposes, “BodyFlex” was run on a machine with the following specifications:

- Machine Type: DELL Precision T7600

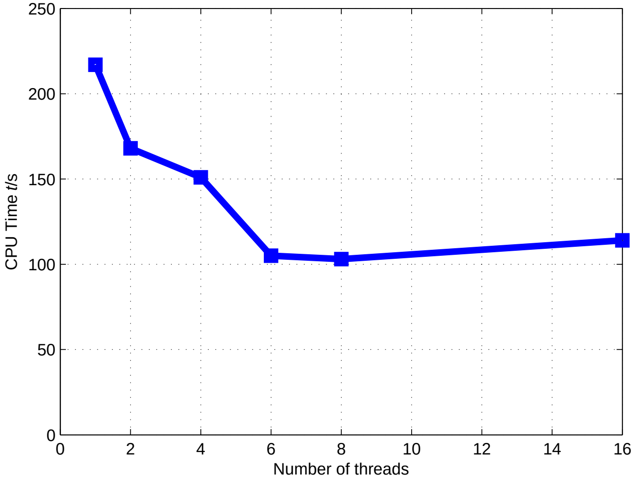

Figure 5.33.: Posture time depending on number of threads

- CPU: 2 * Intel Xeon E5-2643 (2 x 4 cores, 3.3 GHz)
- RAM: 256 GB

Within “BodyFlex”, both the posture and the export process are parallelized. During the posture process, voxels positions are calculated after the movement of the human model. Each voxel data is written on a separate memory location, which prevents conflicts during parallel execution. Therefore instead of calculating only one voxel position at a time, using OpenMP®, the number of CPUs on the machine where the program runs is found and the threads are defined for each CPU core. Then, the threads are run in parallel and each thread calculates one voxel position. Figure 5.33 shows the posture time depending on the number of threads defined for parallel calculations. It can be noticed that the computing time when eight threads are used, which is the number of the CPU cores that the testing machine has, is twice faster than the time for calculation when only one thread is defined. Setting larger number of threads than the actual number of CPU cores does not lead to any further speedup of the program.

During the export process, not only the export dataset is built, but also the possible discontinuities of the tissues inside the human model are being explored. Finding the discontinuities of the tissues in a parallel manner is also possible. Again using the OpenMP®directives, the execution of the code was accelerated. Figure 5.34

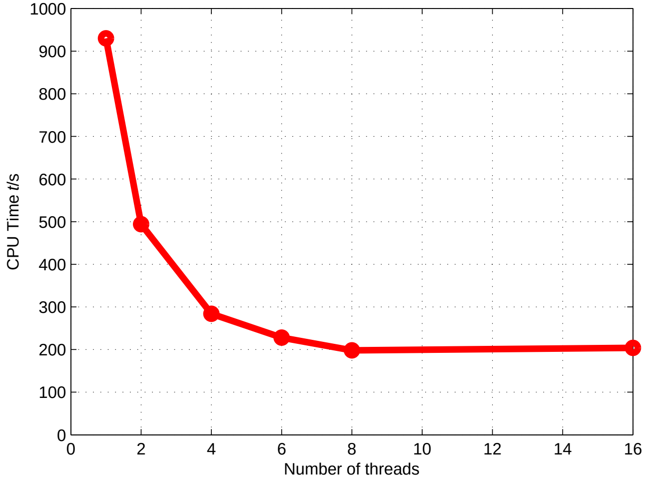

Figure 5.34.: Export time depending on number of threads

shows the posture time depending on the number of threads defined for parallel calculations. It is remarkable that the calculation when eight threads are defined, is almost five times faster than the calculation when only one thread is defined. The parallel execution drastically shortens the time for exporting large datasets, which is of high importance for the user.

6 Comparative Analysis of Performance when Posturing Human Models

In this chapter, a brief description of some existing softwares for posturing of human models is given. The performances of each software in terms of time for posturing of the human model and in terms of memory occupation are analyzed. Later, the performances and the results are compared to “BodyFlex”. All performance checks are performed on a server with the following characteristics:

- CPU: 2 * Intel Xeon X5472 (Quadcore, 3.00 GHz, 1,600 MHz FSB, 12 MB L2 Cache)
- Memory: 64 GB, 800 MHz, QuadChannel FBD

6.1 Varipose Software

6.1.1 Overview and Characteristics

VariPose is a tool for posturing voxel-based mesh of the Visible Human dataset [88]. This software tool deforms only one segmentation of the Visible Human dataset which contains 39 tissues. The Visible Human dataset can be imported in a binary format and exported in a binary (.raw), ASCII (.vox) or XFdtd suitable file. The XFdtd suitable file which stores tissue electrical parameters for a certain frequency, can be used in the XFdtd software for FDTD-based electromagnetic simulations. Exporting the data in a .vox format leads to an ASCII file which holds information about the locations of the voxels in 3D space and the color associated to the tissue in each voxel. There are five mesh sizes in which the Visible Human data set is available, namely, 10, 5, 3, 2 and 1 mm.

The process of repositioning of the human model is conducted through a project which contains various studies. This project consists of a base skeleton and a base mesh (see Figure 6.1), which are set in the default position of the Visible Human

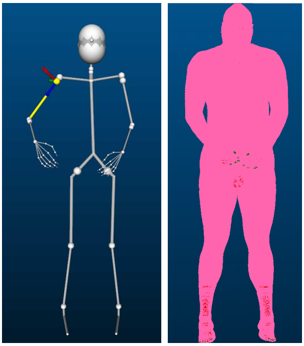

Figure 6.1.: Base Skeleton and Base Mesh representation

data. A copy of the base skeleton, which can be set in different postures, is available for each study. After the skeleton is moved in a desired position it can be used as an input for the VariPose engine, which builds a new repositioned mesh based on the skeleton. This mesh can be exported by the user for future use. Also the user has the opportunity to see the repositioned mesh in the Graphical User Interface (GUI). Additionally, using the GUI, the volume, the mass and the voxel count of all tissues are available for the initial as well as for the repositioned mesh of the human model dataset.

The graphical user interface allows visualization and manipulation of the Human Model dataset (as shown in Figure 6.2). Using the View menu, the user can see the mesh model, choose between a X, Y and Z sliced view, a 3D view, or a combination of both. The user can also choose to see the model in cubes or points. Another useful option is the fast move option, which replaces the mesh model with a box when the human model is rotating. Using the tools menu, the user can rotate, move and zoom the model, select, add or delete certain tissue voxels and reset the view without changing the joint positions.

After the skeleton is set in the desired position, an input generated by the user is forwarded to the repositioning engine. This engine consists of five components. The master program is called *VPEngine*. The input in this program is the file which contains the repositioned skeleton, from which the new repositioned mesh should be generated. This program creates input files for the other components and calls their routines. The components are called in the following order: *Separate_Body*, *Multibend*, *Heal_Body*, *Join_Body* and once more *Heal_Body*. The *Separate_Body* component separates the limbs from the trunk. Then, the *Multibend* component makes the reposition of the separated body parts. In the next step, the *Heal_Body*

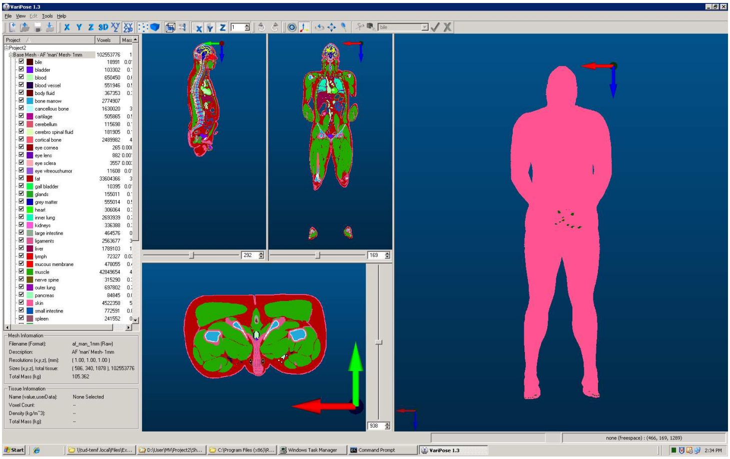

Project	Voxels	Mass
Project2		
Base Mesh - AF 'man' Mesh- 1mm	102553776	1
☑ bile	18991	0.0
☑ bladder	103302	0.
☑ blood	650450	0.
☑ blood vessel	551946	0.
☑ body fluid	367353	0.
☑ bone marrow	2774907	
☑ cancellous bone	1630020	3
☑ cartilage	505865	0.
☑ cerebellum	115698	0.
☑ cerebro spinal fluid	181905	0.
☑ cortical bone	2489982	4
☑ eye cornea	265	0.00
☑ eye lens	882	0.00
☑ eye sclera	3557	0.00
☑ eye vitreoushumor	11608	0.0
☑ fat	33604366	3
☑ gall bladder	10395	0.0
☑ glands	155011	0.
☑ grey matter	555014	0.
☑ heart	306064	0.
☑ inner lung	2693939	0.
☑ kidneys	336388	0.
☑ large intestine	464576	0
☑ ligaments	2563677	3
☑ liver	1789103	1
☑ lymph	72327	0.0
☑ mucous membrane	478055	0.
☑ muscle	42849654	4
☑ nerve spine	315290	0.
☑ outer lung	697802	0.
☑ pancreas	84845	0.
☑ skin	4522358	5
☑ small intestine	772591	0.
☑ spleen	241552	0

Mesh Information
Filename (Format): af_man_1mm (Raw)
Description: AF 'man' Mesh- 1mm
Resolutions (x,y,z), (mm): (1.00, 1.00, 1.00)
Sizes (x,y,z), total tissue: (586, 340, 1878), 102553776
Total Mass (kg) 105.362

Tissue Information
Name (value,userData): None Selected
Voxel Count: --
Density (kg/m^3): --
Total Mass (kg): --

Figure 6.2.: VariPose graphical user interface

component is called in order to fill the gaps between the tissues that might appear after the repositioning. This component is also called at the end of the repositioning process, to add skin to the outer layer of the body, so that the whole human body is covered with skin and to generate the output file. The *Join_Body* component makes a combined mesh of the repositioned limbs and the trunk. All five components of the repositioning engine can run separately with a certain input file. Additionally, the repositioning engine can be run on several computers or several processors at once.

6.1.2 Strengths and Weaknesses of the Software

The VariPose software has some advantages and disadvantages. The software allows examining a single, multiple or all tissues. To increase the performance of the GUI for large meshes, the user is allowed to reduce the drawn data from the human model dataset. Another useful advantage is the presence of the crop tool. The crop tool allows a three-dimensional block of the mesh to be selected through the two-dimensional view and to be saved as a separate file. However, these cropped meshes cannot be further repositioned. Another tool worth to be mentioned is the so-called edit mesh tool, which allows adding and deleting voxels of any tissue type. This tool can be used when the repositioned mesh is non-satisfactory. A very useful tool in VaryPose is the mesh comparison tool. This tool allows comparison of the number of voxels, the volume and/or the mass of the tissues between the default and the repositioned mesh. Despite the options for the mesh view, the user can save the skeleton after the repositioning and use it in future.

Although VariPose allows the generation of various postures by moving the skeleton, it does not guarantee that the repositioned mesh is a realistic position of a human. Overlapping of body parts may occur after the skeleton is moved without warning the user about the unrealistic posture. The software maintains the blood vessels and the nerve tissues in the mesh, but this is not true for all possible cases of deformation. The explanation is given in the next section. Another disadvantage is the computationally intensive repositioning process. For finer meshes, depending on the number of joints moved, the process can take from a few hours to a few days. It is recommended that the desired position of the mesh is chosen under coarser mesh resolution, and later the same position is applied for repositioning of the finer mesh. However, for more precise deformations, the repositioning of the coarser mesh resolution might not result into the desired position of the finer mesh. Another characteristic of the VariPose software is the support of two kinds of movements: bending and twisting. The bends are applicable to all joints, while the twists are only applicable to forearms, upperarms and neck. The twist movement is not recommended to be used if it is not necessary because it is a computationally intensive process.

6.1.3 Performance Analysis

The VaryPose software was tested according to the time for repositioning of the human model and the memory occupation for running this process. All the tests were conducted using the 2 mm mesh resolution.

At the beginning, two scenarios are tested. In the first scenario, the right arm of the human model is stretched. To achieve this pose, the shoulder, the elbow and the right index and middle finger MCP joints are rotated as shown in Figure 6.3. The elapsed time for repositioning of the human model in VariPose, which took place on one CPU core, is 55 minutes. The same posture is generated using the BodyFlex (Figure 6.3 (right)). In this case, the elapsed time for repositioning of the human model is 43 seconds by using one CPU core for computation.

In the second scenario, the right elbow of the model is bent for the maximum angle of rotation allowed for the elbow. To achieve this position, rotation and twisting of the shoulder and the elbow are performed. Again, the repositioning process with VariPose is running on one CPU core, resulting in elapsed time of execution of 9 hours and 53 minutes. The same posture of the human model in BodyFlex is achieved in 43 seconds using one CPU core. The repositioned mesh in VariPose for the second scenario is given in Figure 6.4 (left), while the repositioned human model from BodyFlex later imported in CST STUDIO SUITE® is shown in Figure 6.4 (right).

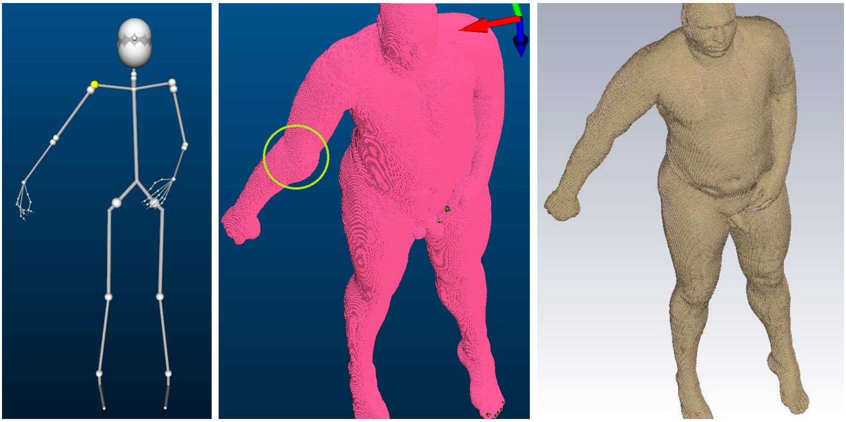

Figure 6.3.: Repositioned human model skeleton (left), model in VariPose (middle) and model from BodyFlex (right) after right arm stretch

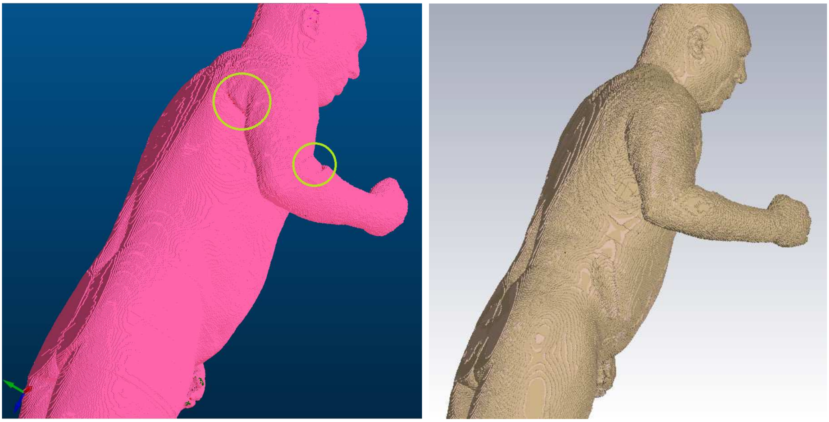

Figure 6.4.: Repositioned model in VariPose (left) and model from BodyFlex (right) after right arm and elbow movements

From Figure 6.3 and Figure 6.4 can be noticed the discontinuities of the tissues and the deformations of the right arm in an unnatural position using the VariPose software. These effects do not exist when the BodyFlex software is used.

Two more scenarios are tested using the VariPose and the BodyFlex software. In the third scenario, the human model is brought to a sitting pose. To achieve this position, the shoulders, elbows, hips and knees are rotated. The elapsed time for repositioning of the mesh using the VariPose is 14 hours and 52 minutes, while the RAM memory usage is around 0.4 GB. The deformed mesh and skeleton look compact, with small discontinuities of the tissues, and are shown in Figure 6.5.

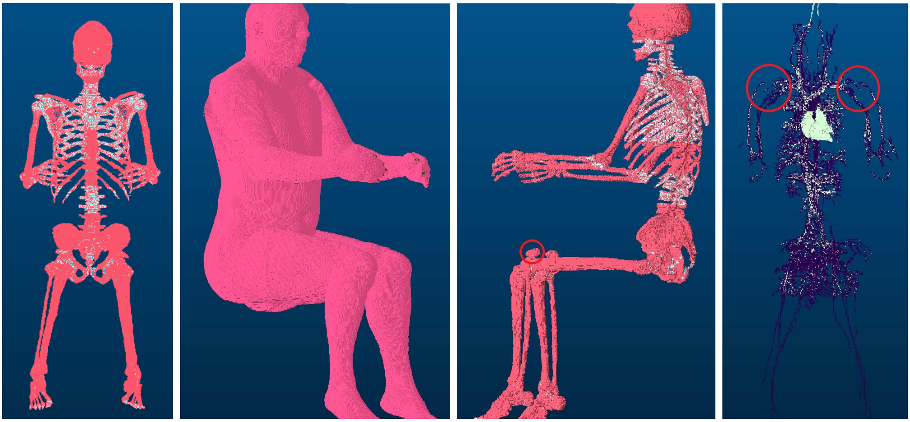

Figure 6.5.: Repositioned mesh of the human model in a sitting position using VariPose

What can be noticed from Figure 6.5 is the wrong position of the patella. Namely, when the knee is bent, the patella should move from the upper leg bone to somewhere between the upper and lower leg bones. The position shown in the figure above, is not natural. Also there exists a discontinuity of the blood vessels in the area around the shoulder, which is not present in the original model.

The same posture is generated using BodyFlex. The time for repositioning the human model is 43 seconds and the RAM memory usage is about 0.8 GB. It can be noticed that the RAM memory usage is double compared to the RAM memory usage of VariPose for the same posture. But if the time for repositioning the model is considered, the BodyFlex software works 10^3 times faster compared to the VariPose software. Additionally, the BodyFlex software treats the patellas separately, which leads to a right placement between the tibia and the femur. The human model exported using the BodyFlex and later imported in the CST STUDIO SUITE® is shown in Figure 6.6.

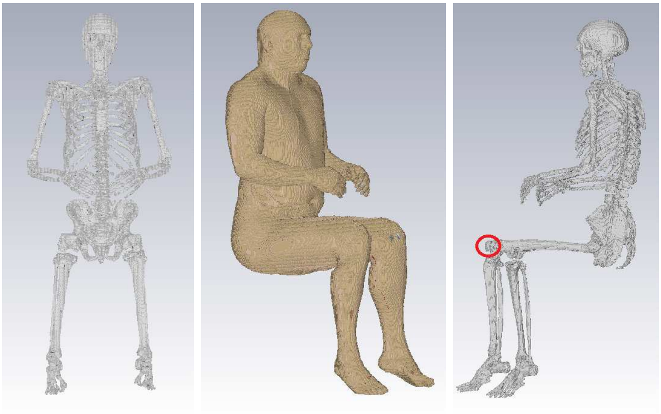

Figure 6.6.: Repositioned mesh of the human model in a sitting position using BodyFlex

In the last scenario, the human model has the right hand postured in a talk position. To achieve this position, the shoulder, elbow, wrist and fingers are rotated. The elapsed time for repositioning the model is 6 hours and 52 minutes and the RAM memory usage is as in the previous scenario about 0.4 GB. From the presented results in Figure 6.7, it is noticeable that parts of the fingers are missing. Actually, this parts are not missing in the total mesh, but they are placed on a wrong position, and they overlap with the upper arm. Also, there are discontinuities of the other tissues.

The HUGO model with the $2 \times 2 \times 2$ mm^3 resolution is also postured in a talk position using BodyFlex. The elapsed time for repositioning is 43 seconds and the RAM memory usage is about 0.8 GB. Although the RAM memory usage using BodyFlex is double compared to the RAM memory usage of VariPose for the same posture, the elapsed time for repositioning the model using the BodyFlex software is 10^3 times shorter compared to the VariPose software. Furthermore, the BodyFlex software postures the arm, hand and fingers accurately, without any missing body parts or noticeable discontinuities of the tissues. Figure 6.8 shows the postured HUGO model in CST STUDIO SUITE®.

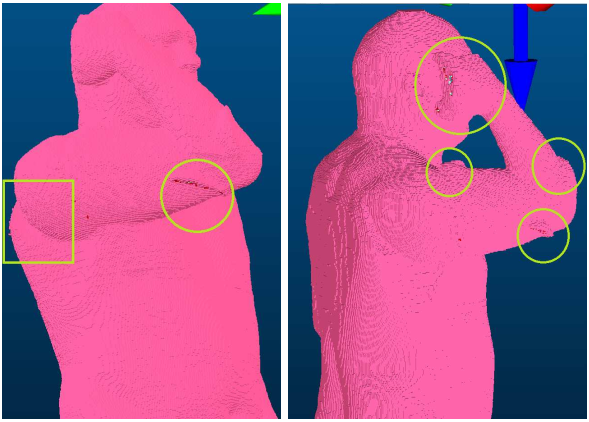

Figure 6.7.: Repositioned mesh of the human model with hand in a talk position using VariPose

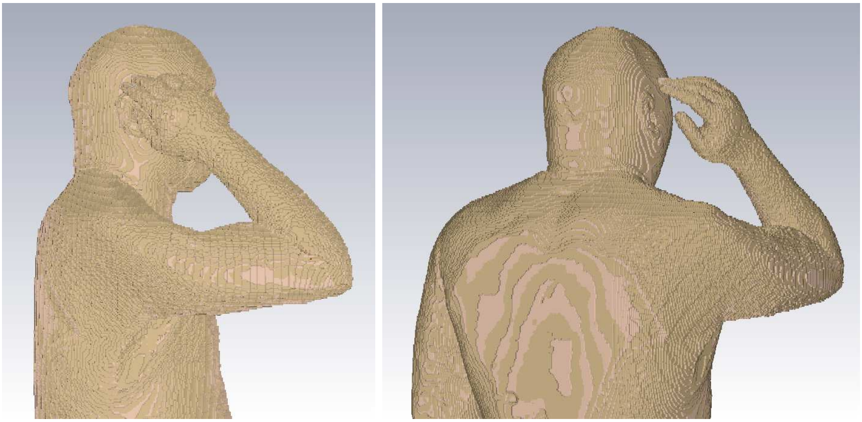

Figure 6.8.: HUGO model with hand in a talk position using BodyFlex

6.2 SEMCAD X Poser Package

6.2.1 Overview and Characteristics

SEMCAD X poser package named POP module allows deformation of human and animal models [95]. Using this module requires previous installation of the Virtual

Family Package, which is developed by the IT'IS Foundation [56]. The posable extensions are later provided by a license from SPEAG, which allow the posable models to be imported into semx (.sat) format in SEMCAD X.

The Virtual Population is a set of computational anatomical models developed by the IT'IS Foundation [21].

For the test purposes within this project, the Ella and Duke posable models (from Virtual Family version 1) were provided together with the POP module. These two models have the following characteristics:

Name	Gender	Age	Height	Weight	No. of tissues
Ella	Female	26	1.6 m	58 kg	77
Duke	Male	34	1.74 m	70 kg	77

The models were deformed in a few positions. Also a process of voxelization of the deformed surface human model was performed right after the deformation. After deformation, an option for creating a grid can be chosen. The grid can be refined using an option scale and the number of voxels of the grid can be adjusted. Depending on the number of voxels of the grid, the time for voxelization of the model differs.

6.2.2 Strengths and Weaknesses of the Software

The SEMCAD X POP module has some strengths and weaknesses. The poser module is based on techniques for computer animation. It allows a hierarchical movement of the bones, e.g if the shoulder is moved, the movement is translated to the elbow and hand respectively. One advantage of the software is the speeding up of the deformation process by activating the multi-threading option.

The deformation of the model is performed through the bone mesh tool. An additional advantage of this software is that during the deformation, influence fields for all affected tissues between the bone and the skin surface are calculated, based on the local distances to the corresponding bone. Calculating the influence fields only to the skin surface prevents the other body parts near the deformation region to be affected from the current deformation. To preserve the tissue continuity in case when the influence regions overlap, a weighted interpolation is performed. The method for deformation is described in [20].

Despite its strengths, the SEMCAD X POP module has also some drawbacks. Using the bone mesh tool, the joints of the underlying rigid skeleton can be rotated in one, two or three planes, depending on the bone. One disadvantage of the software is that the range of rotation for the bones is not clearly limited, which allows the user to deform the model in unreal postures. Another drawback is the interactive rotation. The interactive rotation means that the body part is moved right after the user specifies the final position. When the user achieves the desired position of a certain bone all the tissues around the deformed bone are repositioned. Depending on the model, it can take some time until the final position is achieved.

In order to test the features of the poser package, at the beginning, few deformations of the human models Ella and Duke are shown. Later, specific postures, e.g., a sitting position and a talk position, are separately analyzed for both models.

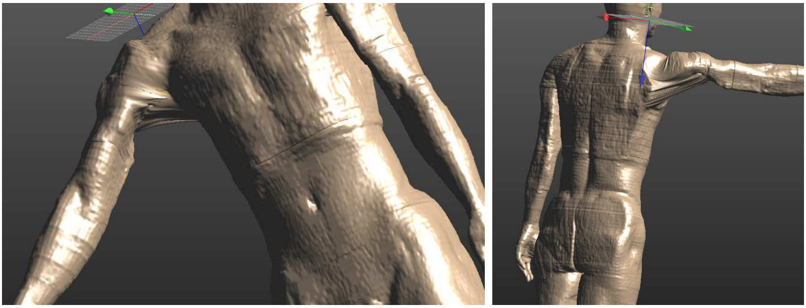

Figure 6.9.: Shoulder deformation of Duke

Figure 6.9 shows the movement of the shoulder of Duke. After the deformation of the shoulder, an unnatural change of the tissues around the shoulder can be noticed.

A few more deformations of the right shoulder, elbow and the fingers are shown in Figure 6.10. It can be noticed that the finger is deformed in an unrealistic position. Also some of the tissues have an unnatural look after the deformation, like for example the part of the skin which is stretched between the fingers. Another important remark is the discontinuity of the tissues after the deformation. Bones and blood vessels preserve the continuity, but noticeable discontinuities can be observed for the skin and the muscles.

Figure 6.11 shows the deformation of Ella. Also here some discontinuities of the tissues are noticed.

6.2.3 Performance Analysis and Comparison with the Poser Program

In this section, Duke and Ella models are postured in a sitting position and in a talk position using the SEMCAD X POP module. The time for deformation and voxelization of Duke and Ella is calculated and also the memory requirements are marked.

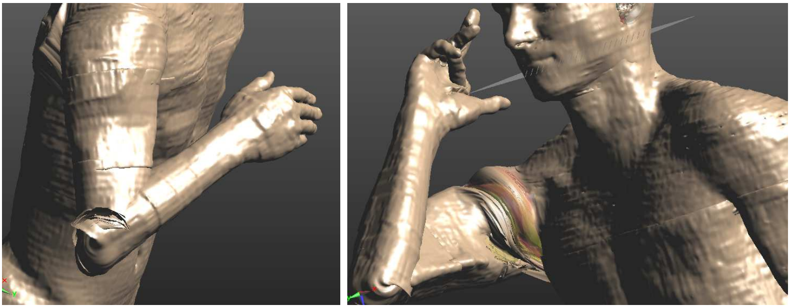

Figure 6.10.: Elbow and arm deformation of Duke

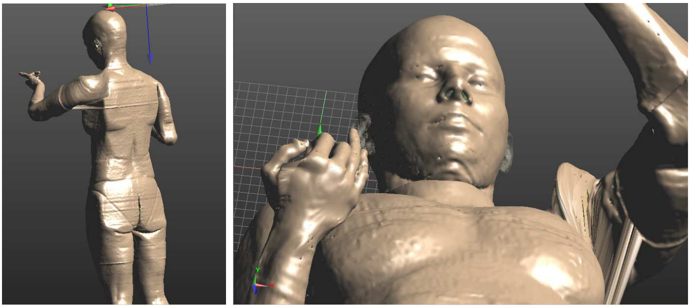

Figure 6.11.: Deformation of Ella

The performance and visual results are then compared to the results obtained using the BodyFlex software and the deformation of the three voxel models, namely, Hugo, Laura and Gustav.

Figure 6.12 and Figure 6.13 show Duke in a sitting position. The memory consumption of the program after importing Duke is 1.29 GB. The time for repositioning the tissues after each deformation step is about 20 seconds. After posturing of Duke in a sitting position, the memory consumption increased to 8.6 GB. In the next step, Duke is voxelized in a dataset with dimensions 467 × 609 × 1083. The duration of the voxelization process is 6 minutes and 23 seconds. The rendering of the voxelized model took 1 minute and increased the memory usage to 11 GB.

In Figure 6.12, the continuity of the blood vessels and the bones can be verified despite the wrong position of the patella and some discontinuities of the skin.

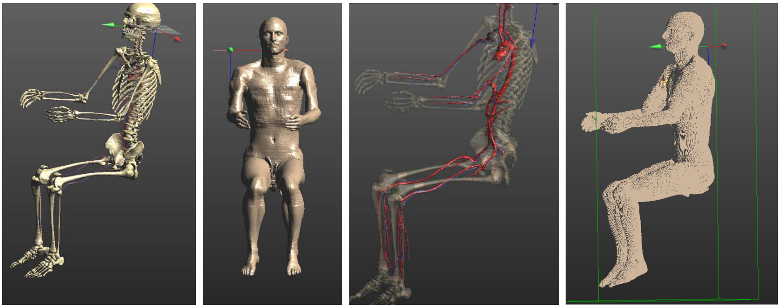

Figure 6.12.: Duke in a sitting position (skeleton, skin, arteries and voxels)

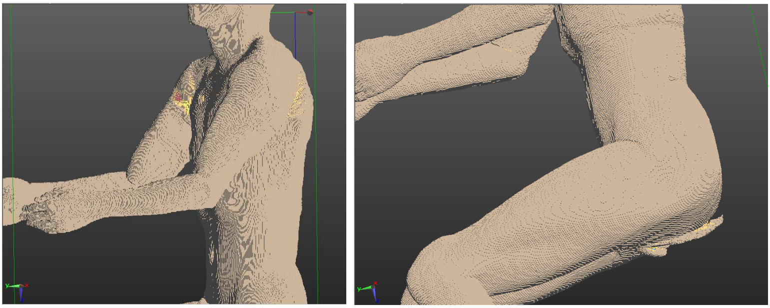

Figure 6.13.: Voxelized Duke in a sitting position

Figure 6.13 shows the voxelized Duke after deformation. The discontinuity of the skin voxels around the shoulders and also the wrong deformation of the area between the legs are noticeable.

The female human model Ella is also postured in a sitting position. After the import of Ella, the memory occupied by the program is 0.95 GB. The time for repositioning the tissues after deformation of a certain body part is the same as for Duke (20 seconds). The memory consumption after Ella is set in a sitting position increased to 3.81 GB. Then the process of voxelization of Ella is performed. The time for voxelization of the model in a dataset with dimensions 394 × 471 × 1053 voxels is 3 minutes and 52 seconds. Again for the rendering 1 minute is necessary.

The results from the repositioning and voxelization process are shown in Figure 6.14. Further analysis is performed regarding the voxelization of the tissues. Each tissue type is checked whether the voxelization is completely performed. The results show that not all the tissues are completely voxelized. Namely, the bones in the fingers are not present after the voxelization process.

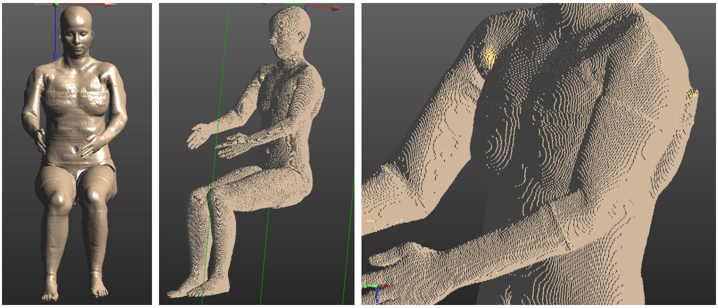

Figure 6.14.: Ella in a sitting position (skin and voxels)

Using the BodyFlex, the human models HUGO, Laura and Gustav are postured in a sitting position. The HUGO model postured in a sitting position has a voxel resolution of $1 \times 1 \times 1$ mm^3 and it is stored in a dataset with dimensions $596 \times 1303 \times 1875$ voxels. The time for posturing of the model is 7 minutes and 24 seconds using one CPU core. The memory usage when the model is postured in BodyFlex is 6.53 GB. The HUGO dataset has almost double of the size of the Duke or the Ella dataset and therefore the time for posturing of Hugo, which would be comparable to the time for voxelization of Duke and Ella is proportional.

Figure 6.15 shows the Hugo model postured in a sitting position. From the result it can be noticed that the continuity of the tissues is maintained and even the small bones in the fingers are present in the postured model. Also the patellas are placed in a realistic position after the movement of the knees of Hugo.

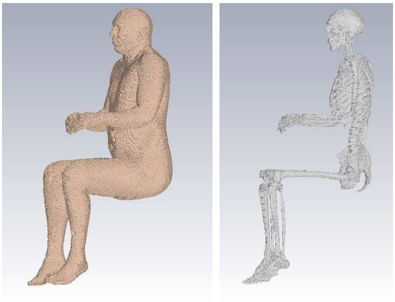

Figure 6.15.: Hugo in a sitting position (skin and bones)

Figure 6.16 shows Laura and Gustav in a sitting position. The human model Gustav, with dataset size 260 × 581 × 882, has a voxel resolution $2.08 \times 2.08 \times 2\ \mathrm{mm}^3$. The time for posturing the model is 3 minutes and 28 seconds and the memory consumption of 0.49 GB is almost the same as in the import step. The human model is rendered and shown in the user interface after 1 minute. From the figure it can be noticed that the continuity of the skin and the bones is maintained. Analysis of the continuity of the other tissues is also performed and the conclusion is that the continuity of all tissues is well maintained.

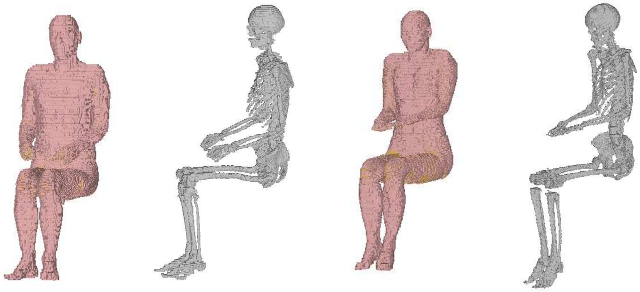

Figure 6.16.: Gustav and Laura in a sitting position

The human model Laura, with a voxel resolution of $1.875 \times 1.875 \times 1.25\ \mathrm{mm}^3$, after posturing in a sitting position has a dataset size 244 × 626 × 1386 voxels. The time for posturing the human model is 5 minutes and 8 seconds and the memory occupation is 0.78 GB, which does not differ from the memory after the import of the human model. The rendering of the human model took 1 minute before the whole model is shown in the graphical user interface. Similarly, the continuity of the tissues is maintained to an acceptable level as in the Hugo and Gustav models.

Table 6.1 shows a summary of the human models, their dataset size and the posture time.

In the second scenario, which is set up for comparison of the performances of SEMCAD X Poser and BodyFlex, the right arm, hand and fingers of the human models are postured in a talk position. The comparison relates to three human models: Duke, Ella and Hugo. The models Laura and Gustav are not considered for the second scenario because their fingers can not be deformed using BodyFlex due to their voxel resolution and inappropriate initial position of the fingers.

Figure 6.17 shows the Duke model postured in a talk position. The memory occupation is 7.49 GB after the model is deformed. After Duke is postured in a talk position, it is voxelized in a dataset with dimensions 401 × 414 × 1119. The vox-

Table 6.1.: Sitting human models dataset size and posture time

Human model	Dataset size/voxels	Posture Time
Hugo	596 × 1303 × 1875	7m 24s
Gustav	260 × 581 × 882	3m 28s
Laura	244 × 626 × 1386	5m 8s
Ella	484 × 571 × 1281	5m 48s
Duke	401 × 414 × 1119	3m 42s

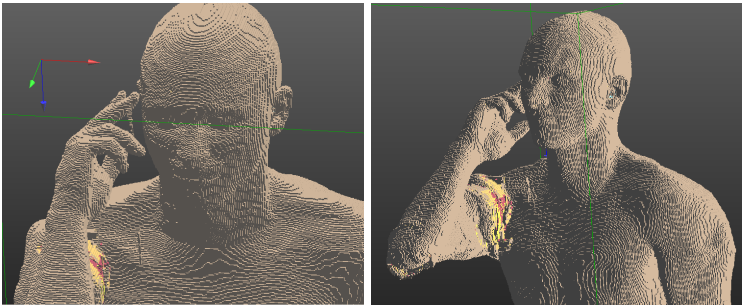

Figure 6.17.: The voxelized Duke in a talk position

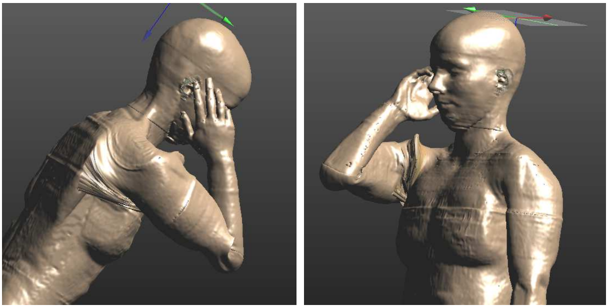

Figure 6.18.: Ella in a talk position (skin)

elization time is 3 minutes and 42 seconds and the time to show the voxelized model is 1 minute. Also the memory usage increased to 9.08 GB when the voxelized model is shown. As in the previous posture, not all bones were voxelized. Especially it can be noticed that the bones in the fingers are missing, which can lead to inaccurate results in case of analysis of energy absorption due to mobile phone radiation.

Figure 6.18 and Figure 6.19 show the model Ella postured in a talk position. After the model is repositioned, the memory occupation is 7.52 GB. The next step is the voxelization of Ella, which takes 5 minutes and 48 seconds. The model is voxelized in a dataset with dimensions 484 × 571 × 1281. The time to render the voxelized model and to show in the graphical interface is 1 minute. As in the previous posture, not all bones are voxelized. Again, the bones in the fingers are missing. However, the stretching of the skin near the fingers does not exist for Ella, but still, some discontinuity of the tissues near the shoulder can be noticed.

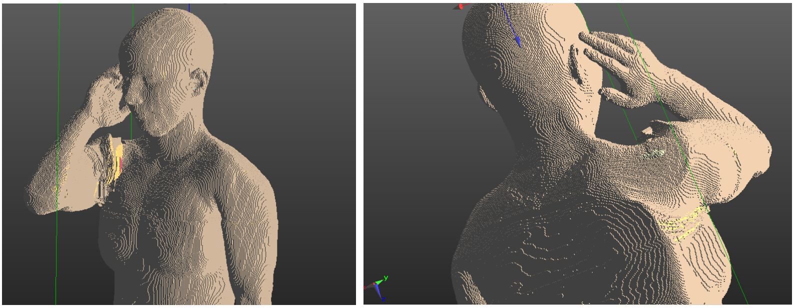

Figure 6.19.: Voxelized Ella in a talk position

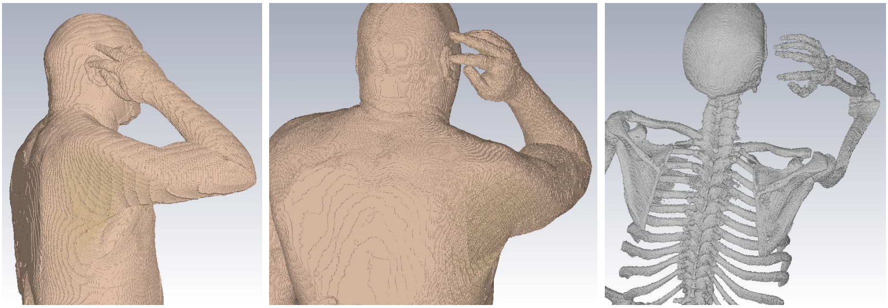

Figure 6.20.: Hugo in a talk position

Figure 6.20 shows Hugo in a talk position. The dataset size of the postured model with voxel resolution $1 \times 1 \times 1$ mm^3 is 732 × 785 × 1875. Posturing of Hugo took 7 minutes and 27 seconds, which compared to the time for voxelization of Duke

Table 6.2.: Human models in talk position: dataset size and posture time

Human model	Dataset size/voxels	Posture Time
Hugo	732 × 785 × 1875	7m 27s
Ella	484 × 571 × 1281	5m 48s
Duke	401 × 414 × 1119	3m 42s

Table 6.3.: Comparison of the time, the memory and the accuracy of Varipose, SEMCAD X POP and BodyFlex

	Varipose	SEMCAD X POP	New BodyFlex
Posturing time	long	short	short
Memory usage	low	high	high
Accuracy	inaccuracies discontinuities	inaccuracies discontinuities	accurate almost no discontinuities

and Ella is proportional to the dataset size. From the figure, the continuity of the skin and the bones can be noticed well. There exists no discontinuity of the tissues around the shoulder. Analyzing the fingers, it can be concluded that all the tissues, that exist in the initial posture of the fingers are still present after deformation. At the same time, the continuity of the other tissues is maintained to an acceptable level.

Table 6.2 gives a summary of the dataset size and the posture time of human models in a talk position.

6.3 Summary

Within this chapter, an analysis and a comparison of the performances of the three softwares for posturing human models is given. Varipose, SEMCAD X POP module and BodyFlex are the three softwares used to deform human models into various postures. These softwares are analyzed in terms of the time for posturing of the human model, the memory usage and the accuracy.

On one hand, Varipose has the lowest memory usage among the three softwares, but also the longest time needed to posture a human model. On the other hand, the SEMCAD X POP module and BodyFlex require more memory, but they posture the human model in a much shorter time compared to Varipose. In terms of the accuracy, BodyFlex generates highly accurate human models in different postures, preserving the continuity of the tissues and organs to a high level. On the contrary, Varipose and SEMCAD X POP module generate human models which have lack of accuracy, as well as visible discontinuities of some tissues and organs. Table 6.3 gives a summary of this analysis and comparison of the three softwares for posturing human models.

7 Analysis of SAR Distribution in Human Models

In this chapter, various simulation scenarios are established to investigate the impact of the electromagnetic fields on original and postured human models. An analysis of the Specific Absorption Rate (SAR) distribution is performed to determine the impact of the posture of the human body and the impact of jewelry and of the metal-framed eyeglasses. In four scenarios, the SAR distribution is related to the radiation from mobile phones. The chapter is split in six sections. The first section explains the Specific Absorption Rate (SAR). In the second section, the impact of the hand on the SAR values is described. The third section describes the impact of the fingers on the SAR values while the following section shows the effects of wearing common jewelry on the SAR distribution. In the fifth section, an analysis of the SAR distribution due to wearing metallic framed eyeglasses is given. Finally, in the last section, the influence of the position of human bodies on the SAR distribution due to a fixed irradiation source is shown.

7.1 Specific Absorption Rate

With the increasing number of electromagnetic devices used all around, the need for continuous examination of the effects of the electromagnetic device radiation on the human body grows year-by-year. Estimating the possible harmful effects of the interaction between the electromagnetic fields and the biological tissues on the health is crucial for the design and the development of electromagnetic devices. Nowadays, by using the electromagnetic simulations, it is possible to predict some effects caused by the radio-frequency exposure, such as heating as well as the specific absorption rate (SAR) distribution, which can not be directly measured inside the human body.

Two international agencies ICNIRP (2009) and IEEE (2005) have developed guidelines in which the radio-frequency exposure limits for mobile phone users are expressed in terms of specific absorption rate (SAR) [3, 2]. The SAR is related to the rate of the energy absorbed by a body exposed to a radio frequency electromagnetic field. It is commonly averaged over the whole body or a sample volume (typically 1 g or 10 g of tissue) and can be expressed by the following formula:

Table 7.1.: Occupational and general public exposure SAR limits

Exposure characteristics	Whole body average SAR	Localized SAR (head and trunk)	Localized SAR (limbs)
Occupational exposure	0.4 W/kg	10 W/kg	20 W/kg
General public exposure	0.08 W/kg	2 W/kg	4 W/kg

$$\mathrm{SAR} = \frac{\iiint\limits_V \frac{\sigma(\vec{r})\left|\vec{E}(\vec{r})\right|^2}{\rho(\vec{r})} dV}{V} \frac{W}{kg}. \tag{7.1}$$

In Eq. (7.1), σ represents the electrical conductivity, ρ is the mass density of the sample tissue, dV is the volume element and V is the volume of the sample tissue. The electric field strength magnitude $\vec{E}$ is given in terms of the root mean square value.

The maximum allowed radio-frequency exposure to mobile phones is controlled by the governments which prescribe the SAR limits in the head and in the limbs. In the USA, FCC [36] limits the maximum SAR to 1.6 W/kg over 1 g of tissue, while CENELEC in Europe [54] allows up to 2 W/kg averaged over 10 g of tissue. The SAR values mentioned previously refer to the head and torso, while for the limbs, the SAR limit is 4 W/kg as shown in Table 7.1.

7.2 Analysis of SAR Distribution due to Mobile Phone Radiation

This section contains the results from the analysis of the SAR distribution considering the radiation from mobile phones. Different simulation scenarios for investigating the SAR distribution in the human body are performed. First a study of the position of the hand and fingers of the human model is performed to determine their influence on the SAR distribution due to mobile phone radiation. The next scenario investigates the SAR effects of wearing common jewelry (rings and earrings). Finally, the last scenario related to the mobile phone exposure shows the results from the impact of eyeglasses on the SAR distribution.

In order to analyze the SAR distribution in the human body resulting from an exposure to radio-frequency electromagnetic fields, simulations were performed with the commercial software CST MICROWAVE STUDIO$^{®}$[26]. Two types of human models are considered in the electromagnetic simulation scenarios: Specific Anthropomorphic Mannequin (SAM) and HUGO. The SAM head model, available in

Table 7.2.: Dielectric properties of the tissue simulating liquid (TSL) at two GSM frequencies [73]

TSL	Rel. Permittivity	El. Conductivity (S/m)
900 MHz	41.5	0.97
1800 MHz	40.0	1.4

CST MICROWAVE STUDIO [26], is a simplified homogeneous human model built of two parts: the outer shell and a tissue simulating liquid. The dielectric properties of the head of SAM are obtained as an average of the dielectric properties of the tissues in an anatomical head. The outer shell of the SAM head model has a relative permittivity of 3.5 and an electrical conductivity of 0.0016 S/m, which are independent from the frequency. On the contrary, the dielectric properties of the tissue simulating liquid (TSL) are frequency-dependent. Their values at two typical GSM frequencies are given in Table 7.2.

Using the SAM head model in the simulations allows a fast determination of the SAR distribution in the human head, with low accuracy. The tissue simulating liquid is a homogeneous material, which does not show in which tissue in the real human head the maximum SAR value occurs. Therefore, it is more realistic to use an inhomogeneous human model. The HUGO model, as previously mentioned in Chapter 2, is a inhomogeneous human model built from 32 tissues. Each tissue in HUGO has material properties which reflect the anatomical human tissue properties. This human model is largely used for electromagnetic simulations. In this research study, the HUGO model allows detailed analysis of the SAR distribution and determination of the exact location of the maximum SAR value.

7.2.1 Influence of the Position of the Hand and the Fingers on the SAR Distribution

The current SAR measurement standards, specify the safety SAR limits by using a homogeneous head phantom (SAM), without considering the hand in which the mobile phone is held in realistic situations. Former studies referenced by the standards show that the presence of the hand generally reduces or slightly increases the SAR in the head [7][66][74].

Recent studies have shown that the consideration of the hand during the measurement of the SAR has an influence on the SAR distribution in the head of the human model [70][76][90]. This type of simulation scenarios describe real life situations in which the users hold the mobile phone in the hand in a talk position. Chung et.

al [70] observed the influence of the hand holding a mobile phone in talk position on the peak spatial-average SAR (psSAR) in the head. They performed simulations and measurements with several mobile phones at GSM frequencies. None of the simulation scenarios uses an inhomogeneous human hand, but only a generic and an anthropomorphic hand. An anatomical hand and an anthropomorphic hand are used only for the measurements. Both simulations and measurements have shown that the presence of the hand causes an increase of the psSAR in the head.

Monebhurrun et. al [76] investigated the influence of the distance of the antenna from the CTIA hand on the SAR distribution inside the SAM head. The CTIA hand model is a homogeneous hand model, recommended by the CTIA (Cellular Telecommunication Industry Association) for usage with the SAM phantom for evaluation of over the air performance of mobile phones [37]. This study shows that higher 10g averaged SAR values are observed in the presence of the hand for the UMTS frequency band, for a distance between the hand and the antenna of about 20 mm.

Ronald et. al [90] designed a hand model to investigate the impact of the hand on the SAR distribution in the head. To investigate the absorption of energy in the tissue, they designed the hand model in three versions. The first version is a solid hand; the second version has a skin and a bone tissue; the third version additionally has finger properties defined as a tendon and a palm defined as a muscle. This study shows that a smaller hand does not significantly change the SAR distribution in the head compared to the standard CTIA hand. However, the definition of a heterogeneous hand is recommended for investigation of the SAR distribution at GSM frequencies, because the different tissues properties reflect the real anatomical hand. The results have shown that the maximum SAR values appear in the hand and this cannot be concluded if a solid hand without dielectric properties has been used.

In this section, a solid hand and a heterogeneous hand with several tissues are used to investigate the SAR distribution both in a hand and in a head. The author has published the results from this study in [104]. The heterogeneous hand is the hand of the HUGO model which was moved and set in different positions, represented in the following simulation scenarios. In order to analyze how the position of the hand and the fingers influence the SAR distribution in the human body, simulations were performed with the commercial software CST MICROWAVE STUDIO®on two models: SAM and HUGO.

Two scenarios with mobile phone placed in a talk position were considered to investigate the impact of the position of the hand. In the first scenario, the mobile phone is solely placed in talk position, while in the second scenario, the hand is included in the simulation such that the mobile phone is held in the SAM's hand or the HUGO's hand is placed behind the mobile phone as shown in Fig 7.1.

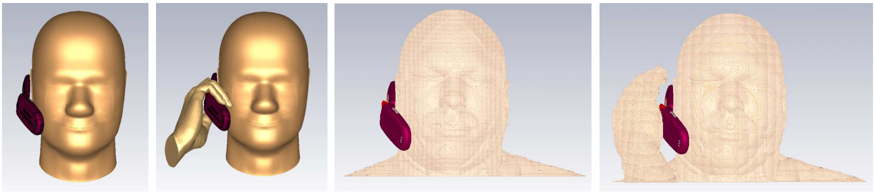

Figure 7.1.: SAM (on the left side) and HUGO (on the right side) models used for simulations

All simulations were performed using the transient solver in CST MICROWAVE STUDIO®[26]. A hexahedral mesh was used for discretizing the simulation domain. In all simulation scenarios, a foldable phone available in CST MICROWAVE STUDIO®, with a PIFA antenna operating at 0.9 GHz and 1.8 GHz was considered. For the excitation, a discrete face port with an impedance of 50 Ohm was defined. The simulated frequency range was between 0 and 2.5 GHz. Field monitors for far-fields, electric fields and power losses were defined at the GSM frequencies. According to [87], mobile phones transmit radio signals only during one eight of the time. Also the SAR values in such simulation scenarios must be avaraged over a 6 minutes interval [1]. Therefore, the reference power at the antenna was set to 1/8th of the maximum input power prescribed by the GSM standard. Namely, at 0.9 GHz, the maximum input power is 2 W, while the reference power at the antenna in the simulations was 0.25 W. Similarly, at 1.8 GHz, the maximum input power is 1 W, while the reference power at the antenna in the simulations was set to 0.125 W. The SAR values were obtained from the power loss density as a post processing result according to the IEEE C95.3 standard averaging method. In this study, the averaging mass was set to 10 g at the frequency of 0.9 GHz, while at the frequency of 1.8 GHz, the averaging mass was set to 1 g.

As expected, the SAR distribution as well as the maximum SAR values differ at the SAM and the HUGO model.

Figure 7.2 shows the SAR distribution in the SAM and the HUGO models at 0.9 GHz, when no hand is present. It can be noticed that the maximum SAR value appears on the cheek of the SAM model. If the maximum SAR values in HUGO are compared to the one in SAM, it can be concluded that for this simulation scenario, the usage of SAM would be better since the results are over-estimated and below the prescribed limits. However, if it is necessary to conduct further analysis about the SAR values inside the head, then using HUGO leads to more accurate results and conclusions.

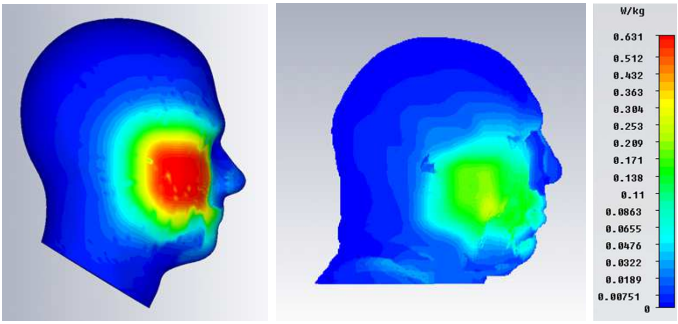

Figure 7.2.: SAR distribution in SAM (left) and HUGO (right) at 0.9 GHz without hand

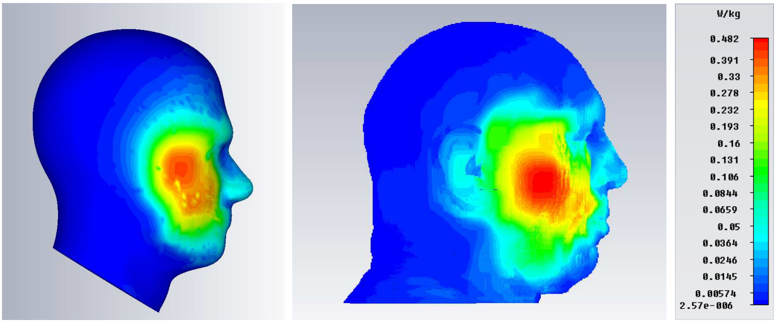

Figure 7.3.: SAR distribution in SAM (left) and HUGO (right) at 1.8 GHz without hand

In Figure 7.3, the SAR distribution is plotted in SAM and HUGO at 1.8 GHz, without hand. In terms of the maximal SAR value, the inhomogeneous HUGO has higher value than SAM. As mentioned above, the advantage of using the realistic inhomogeneous human model instead of the homogeneous human model is that it allows an accurate analysis of the SAR distribution inside the model. The area colored with red as shown in Figure 7.4 identifies the part of the head which absorbs the most energy. Analyzing HUGO, the maximum SAR values occur within the skin and within the fat tissue near the cheek. Additionally, some increased SAR values occur in the muscles in the cheek and in the mucous membrane in the nose.

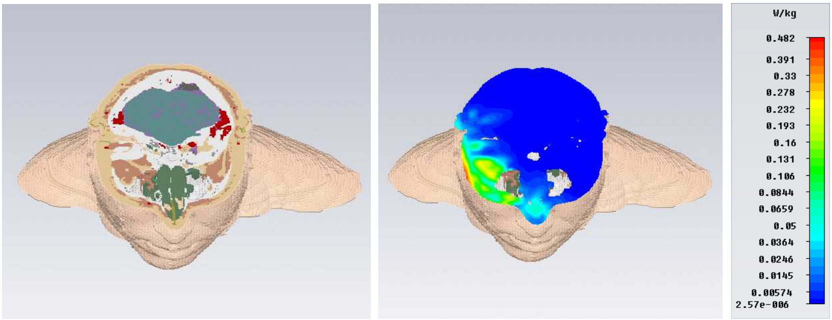

Figure 7.4.: Cut view of HUGO with SAR distribution at 1.8 GHz without hand

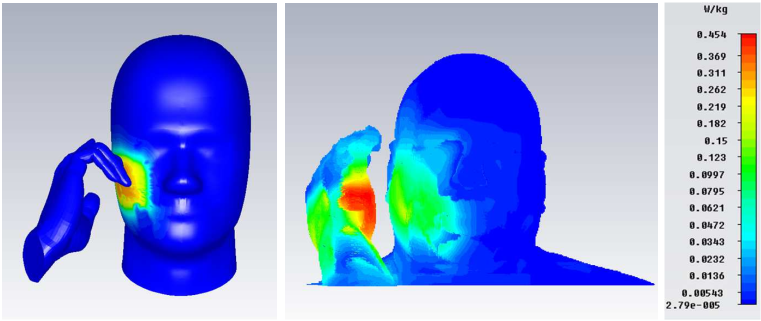

Figure 7.5.: SAR distribution in SAM (on the left side) and HUGO (on the right side) models at 0.9 GHz with hand

Therefore, simulating only the phone next to the head, but without a hand, to determine the maximum SAR value does not reflect reality. The next simulation scenarios include the SAM head together with a solid hand and the HUGO head together with HUGO's hand placed behind the mobile phone. The plots of the SAR distribution for this scenario are shown for both the SAM and HUGO models in Figure 7.5 and Figure 7.6.

Figure 7.5 shows the SAR distribution in SAM and HUGO at 0.9 GHz with hand. The results show that the maximum SAR value both in SAM and HUGO is lower in the head when the hand is present. Moreover, the SAR distribution in the inhomogeneous HUGO's hand can be computed and compared to the maximum SAR values allowed in the limbs. This is not the case when the solid hand is considered.

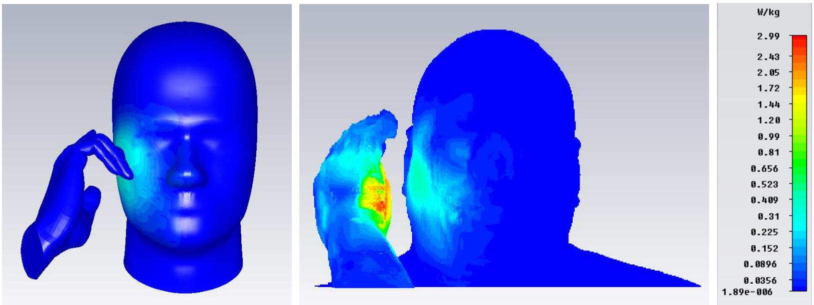

Figure 7.6.: SAR distribution in SAM (left) and HUGO (right) at 1.8 GHz with hand

Due to the lack of dielectric properties, the SAR values in the solid hand can not be computed.

Figure 7.6 shows the SAR distribution in the SAM and HUGO models at 1.8 GHz, with hand. The results show that in this case the SAR values in HUGO's head are lower than the ones in SAM's head. Additionally, it is noticeable that the maximum SAR appears in the hand of the human model, which is expected, because more of the antenna energy is radiated in the direction away from the head.

Figure 7.7 shows the SAR distribution in the HUGO model at 1.8 GHz with and without hand. When the hand is included in the simulation scenario, the maximum SAR value in HUGO's head decreases. This means that the hand has to be considered when the maximum SAR values are estimated in electromagnetic simulation scenarios which are related to the exposure from the mobile phone radiation.

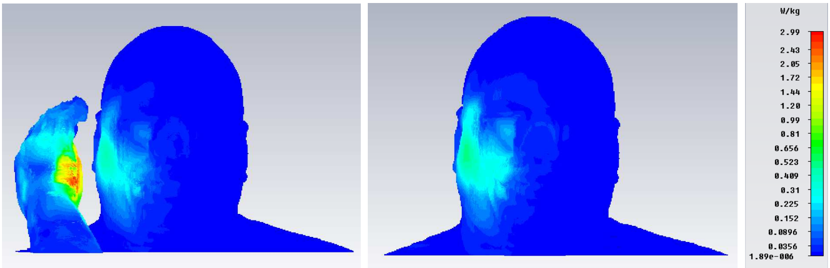

Figure 7.7.: SAR distribution in HUGO at 1.8 GHz

The next simulation scenarios are related to the impact of the positioning of the fingers on the SAR distribution due to mobile phone radiation. In order to analyze the SAR distribution in the human head, three simulation scenarios were

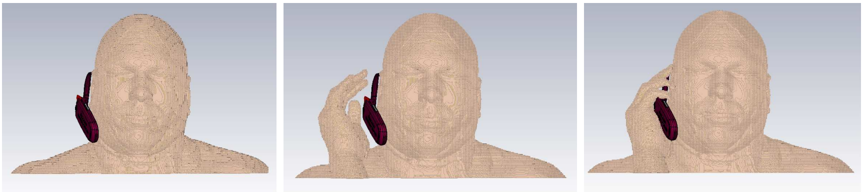

Figure 7.8.: Three postures of the HUGO model used in the simulations

performed using the transient solver in the commercial software CST MICROWAVE STUDIO® [26]: 1) the mobile phone is placed near the head, 2) the hand is placed behind the mobile phone and 3) the mobile phone is held in the hand, as shown in Figure 7.8. The same simulation setup is made and the same mobile phone is used as in the previous simulation scenarios. The author has published the results from this study in [105].

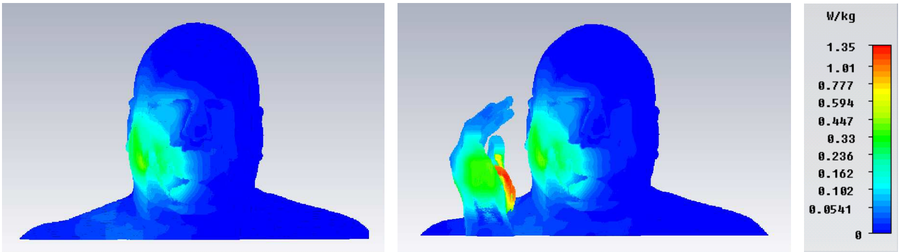

Figure 7.9.: SAR distribution at 0.9 GHz when the mobile phone alone is placed near the head (left) and the hand is placed behind the mobile phone (right)

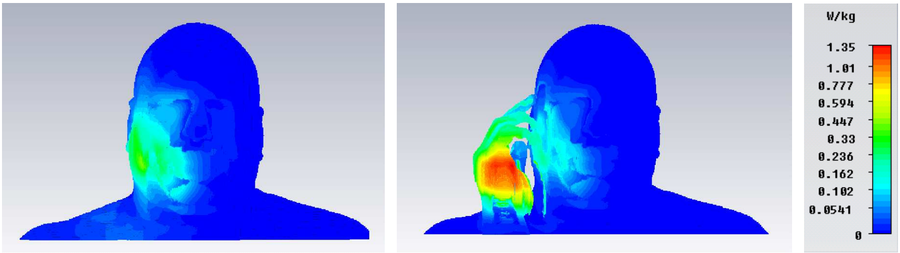

Figure 7.10.: SAR distribution at 0.9 GHz when the mobile phone alone is placed near the head (left) and the mobile phone is held in the hand (right)

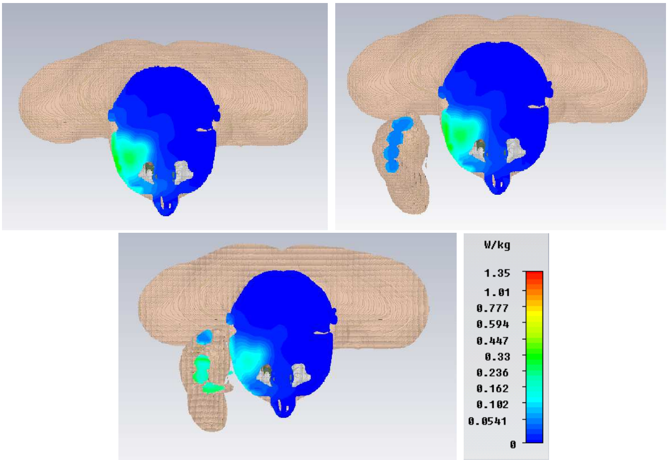

Figure 7.11.: SAR distribution in the head at 0.9 GHz for three different positions of the HUGO model

Figure 7.9 and Figure 7.10 show the SAR distribution at 0.9 GHz in the three scenarios. For the sake of clarity the mobile phone is not shown. From the results it can be observed that there is a slight difference between the SAR distribution in the head when there is no hand in the simulation and when the hand is placed behind the mobile phone. Namely, the presence of the hand causes a decrease of the SAR values on the surface of the head. This effect is more obvious in the case when the mobile phone is held in the hand. It can be observed that the area with positive SAR values in the head is significantly smaller compared to both previous cases. Also the maximum SAR value on the surface of the head is smaller when the mobile phone is held in the hand compared to both previous cases.

Additional analysis of the SAR distribution inside the head is shown in Figure 7.11. From Figure 7.11, it can be noticed that the maximum SAR values in the head, which appear when the hand is not present in the simulation, are higher compared to the case when the mobile phone is held in the hand. When the hand is present in the simulations, it absorbs a large part of the energy. Also, the maximum SAR values in HUGO's head decrease when the mobile phone is held in the hand.

Although the SAR values in the hand are high, they are below the limits prescribed in the standards, which are fixed to 4 W/kg for limbs. The computed SAR values in the head are also below the prescribed limits from 1.6 W/kg in Europe and 2.0 W/kg in USA.

7.2.2 Impact of Rings and Earrings on the SAR Distribution due to Mobile Phones Exposure

In this study, the author analyzes the SAR distribution and the maximum SAR values obtained through simulations in which the head and the hand of the inhomogeneous human model HUGO are considered. Some of the results from this study are published in [80].

Many mobile phone users wear jewellery, like earrings and rings, which may have an influence on the absorption of energy in the head or/and the hand. There are already numerous studies conducted within this research field.

Whittow [108, 109, 110] used a dipole and performed Finite-Difference Time-Domain (FDTD) simulations to investigate the effects of metallic braces, earrings, tongue and eyebrow jewellery on the SAR values. In his research he used a homogeneous and an anatomical human head and compared the SAR distributions in both. The results show that when the size of the jewellery is of the same order as of the wavelength, it can cause an increase of the SAR values in the head.

Islam [55] considered a ring placed on the human hand in order to analyze its impact on the average peak SAR when the user talks on a mobile phone. In the study, he used the homogeneous human model SAM (Specific Antropomorphic Manequin) which is proposed for evaluation of the peak SAR by the measurement standards. The ring, which was modeled as a perfect electric conductor (PEC), was placed on a hand that is not conducting. For the simulations, he used an internal dual-band inverted F-antenna (PIFA). The results show an increase of the SAR values in the head, but they vary depending on the finger on which the ring is worn.

Samsuri and Flint [92, 91] investigated the effect of wearing loop-like jewellery, like rings and bangles in homogeneously filled head and hand phantoms. In their research, they used two types of antennas: a monopole antenna and a PIFA antenna. Considering the monopole antenna, their results show that by wearing a ring on the hand, the absorbed energy in the head and in the hand decreases. On the contrary, when the PIFA antenna is used, the absorbed energy increases both in the head and in the hand. The authors conducted measurements and simulations using the homogeneous head and hand phantoms.

Simulation Setup

The same simulation setup was made as in the previous simulation scenarios. In this study, two types of simulation scenarios are proposed, based on the two types of mobile phones used in them: a foldable phone, which is the same mobile phone described in section 7.2.1, and a small phone. Figure 7.12 shows the position of the mobile phone and the human model for both simulation scenarios. The aim of these simulations is to observe and compare the SAR distribution for different shapes and phone positions.

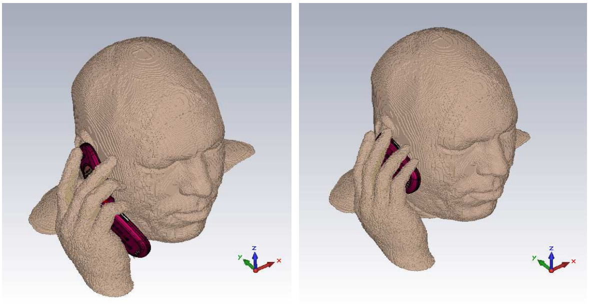

Figure 7.12.: Phones used in the simulations

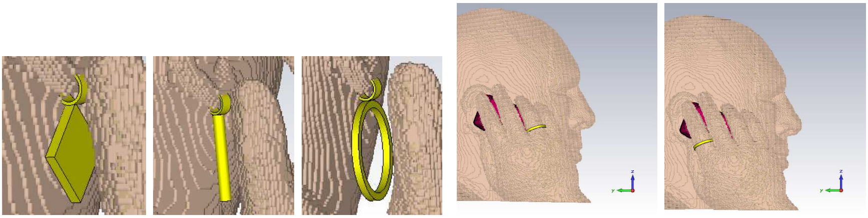

Figure 7.13.: Earrings and rings used in the simulations

Figure 7.13 shows the earrings and ring used in the simulations. There are three different shapes of golden earrings, which are considered in the simulations: rhomboidal, straight and creole (see Figure 7.13). Numerous simulations are conducted for each earring type and different earring dimensions to analyze the impact of the earring's shape and its dimensions on the maximum SAR values and the SAR distribution in HUGO's head. Within this dissertation, only the most important results in terms of the maximum SAR values are presented. Also, simulations are conducted with the golden ring, which is placed in two positions: on the index and on the ring finger. From this simulations, an analysis of the maximum SAR value in the hand and the SAR distribution in the head is performed.
As expected, in all simulations, the maximum SAR value occurs in the hand of the HUGO model. The PIFA antenna, which is embedded in both phone types, radiates in the direction away from the head.

Effect of Earrings

The analysis of the effects of the earring's shape on the maximum SAR value and the SAR distribution at frequency of 1.8 GHz show that only the creole type earring with circumference of $\sim 1\lambda$ has a noticeable effect when the small phone is used in the simulations. For analyzing the SAR distribution, a cross section at $z=765$ mm (below the ear) is shown in Figure 7.14. In comparison with the SAR values in the head without earring, it can be noticed that the SAR values in the head decrease when the creole type of earring is worn. However, it can be noticed that the SAR values on the surface of the human head increase when the earring is considered in the simulations. On the contrary, the rhomboidal and the straight shaped earrings have only negligible effects.
The same analysis is conducted at a frequency of 0.9 GHz when the small phone is used, but there are no significant changes in the SAR values and SAR distributions when the earrings are considered in the simulations. Also the results obtained from the simulations when the foldable phone is used show almost no change of the SAR distribution and the maximum SAR value.

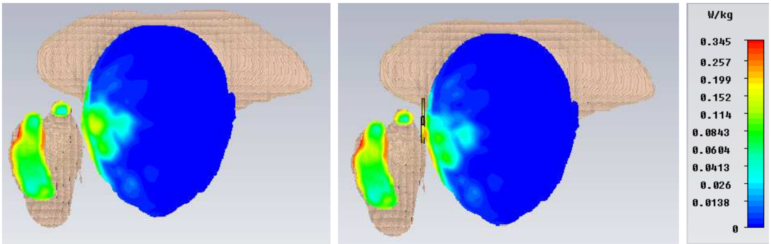

Figure 7.14.: SAR distribution in a cross section below the ear (z=765), at 1.8 GHz and for 1 g averaging mass: without earring (left) and with creole-type earring (right)

Effect of Rings

For an analysis of the effects of wearing a ring on the SAR distribution at the GSM frequencies, several 2D planes (cross sections) are created starting below the ear (at $z=745$) to above the ear (at $z=815$) with a step 10. The maximum SAR results are calculated for both 10 g and 1 g averaging mass. However, all significant results are obtained for 1 g averaging mass and will be discussed in this section. A comparison in terms of the 1 g SAR is made between three scenarios in which either the ring is not considered or it is placed on the index or the ring finger. The simulations are performed using the both phones: a foldable and a small one.

First an analysis of the results at 0.9 GHz is given. When the foldable phone is used in the simulation and the ring is placed on the ring finger, the maximum 1 g SAR value significantly increases at the cross section z=795 as shown in Figure 7.15. At this cross section, the maximum 1 g SAR value increases by a factor of 3 when the ring is placed on the ring finger.

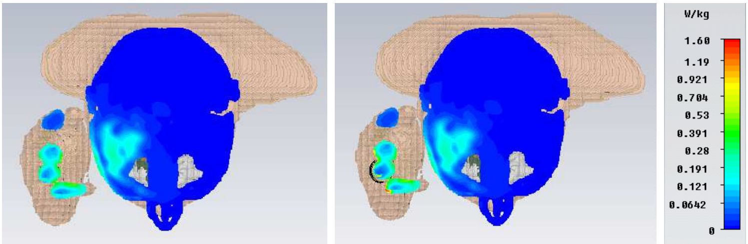

Figure 7.15.: SAR distribution in a cross section above the ring (z=795) at 0.9 GHz and 1 g averaging mass when a foldable phone is used: without ring (left) and with ring (right) on the ring finger

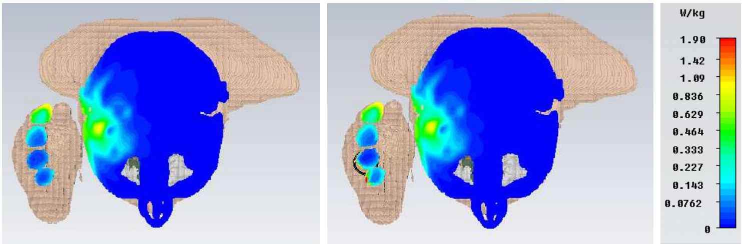

Figure 7.16.: SAR distribution in a cross section above the ring (z=795) at 0.9 GHz and 1 g averaging mass when a small phone is used: without ring (left) and with ring (right) on the ring finger

Figure 7.16 shows the maximum 1 g SAR value obtained at the same cross section when the ring is placed on the ring finger and the small phone is used in the simulation. At this cross section (z=795) the maximum 1 g SAR increases by a factor of 2 when the ring is placed on the ring finger.

From the both figures it can be noticed that the maximum 1 g SAR values increase only in the fingers. Looking at the SAR distribution in the head, there is no significant difference when the ring is worn on the ring finger.

The same simulation scenarios are repeated with the ring placed on the index finger. However, there are no significant differences in the calculated maximum 1 g SAR values when there is no ring or there is a ring placed on the index finger.

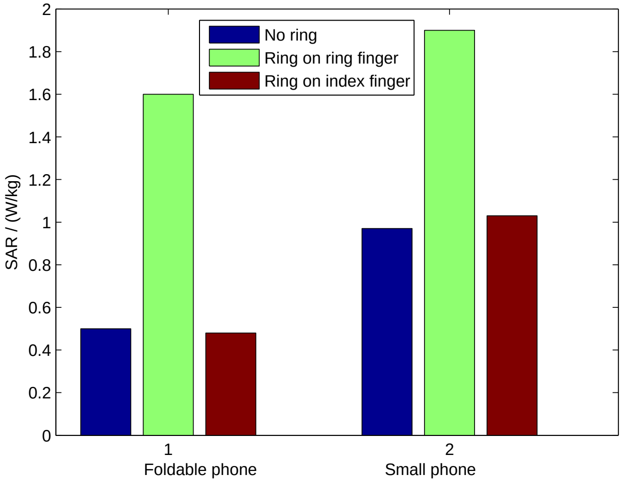

Figure 7.17.: Maximum 1 g SAR value at 0.9 GHz and at cross section z=795

Figure 7.17 shows a summary of the results for the maximum 1 g SAR value at 0.9 GHz at the cross section z=795.

At a frequency of 1.8 GHz when a foldable phone is used and the ring is placed on the ring finger, the maximum 1 g SAR value significantly increases at the cross section z=785 as shown in Figure 7.18 . At this cross section, the maxumum 1 g SAR value increases by a factor of 4 when the ring is worn on the ring finger. Figure 7.19 shows the SAR distribution at the cross section z=785. On one side, the SAR values in the ring finger near the ring increase significantly compared to the case without ring. On the other side, there is no noticeable effect of the SAR distribution in the head when a ring is worn on the ring finger.

From Figure 7.18 it can be noticed that there is almost no difference in the maximum 1 g SAR results when the ring is placed on the index finger.

Further analysis is performed at the same frequency but with the small phone. In this case there is a significant increase of the maximum 1 g SAR value at the cross

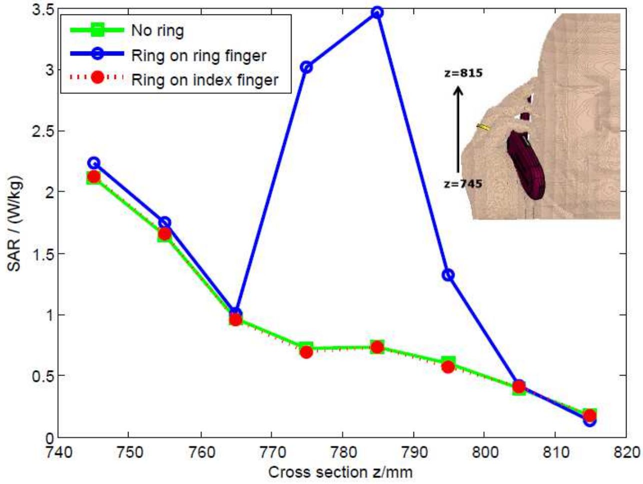

Figure 7.18.: Maximum 1 g SAR value at 1.8 GHz at different vertical cross sections (inset) when a foldable phone is used

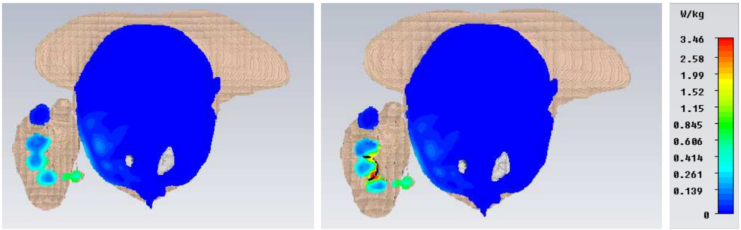

Figure 7.19.: SAR distribution in a cross section above the ring (z=785) at 1.8 GHz and 1 g averaging mass when a foldable phone is used: without ring (left) and with ring (right) on the ring finger

section z=775 when the ring is included in the simulation (as shown in Figure 7.20). Namely, when the ring is worn on the ring finger, the maximum 1 g SAR value increases by a factor of 2. Moreover, when the ring is worn on the index finger, the maximum 1 g SAR increases by a factor of 3.

Figure 7.21 shows the SAR distribution at the cross section z=775 when the ring is worn on the index finger. In this case, the maximum 1 g SAR value increases significantly in the index finger, near the ring. However, as in the case when the

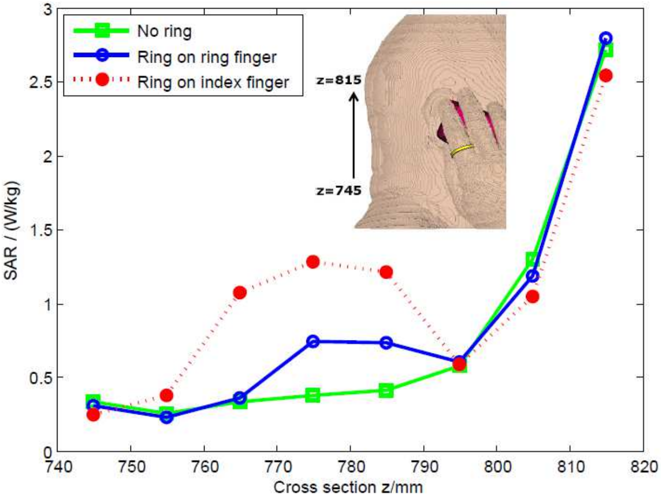

Figure 7.20.: Maximum 1 g SAR at 1.8 GHz over different z planes / cross sections (inset) with a small phone

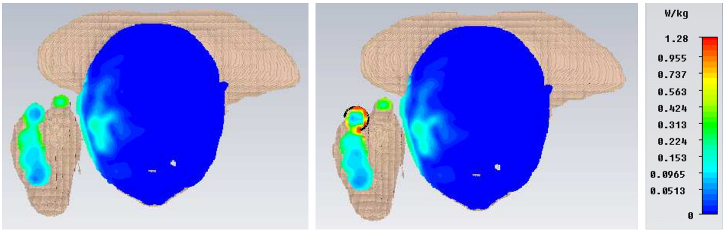

Figure 7.21.: SAR distribution in a cross section above the ring (z=775), at 1.8 GHz and 1 g averaging mass, with a small phone: without ring (left) and with ring (right) on the index finger

foldable phone is used, there is no noticeable difference in the SAR distribution in the head when the ring is worn on the index finger compared to the case without ring.

From all results it can be concluded that depending on the position of the antenna and the ring, due to the radiation of the antenna, an induced current appears in the ring, which causes additional energy to be absorbed by the tissues in the fingers.

7.2.3 Impact of Eyeglasses on the SAR Distribution

In this section, the effects of wearing metal-framed eyeglasses are studied, when a human model is exposed to mobile phone radiation. The author published the results of this study in [81].

The motivation for this study is the increasing number of mobile phone users that wear metal-framed spectacles. In presence of mobile phone radiation, an induced current may appear in the metal frames, which could result in an increased energy absorption in the human head. In most of the studies within this research field, the authors simplify the real situation by either using homogeneous human models or antennas which are not used in the mobile phones, which could lead to wrong conclusions.

Mat et al. [73] used a dipole antenna instead of a real mobile phone antenna, placed in front of the head of the SAM and HUGO models, to investigate the impact of wearing metal-framed glasses on the SAR distribution. Their results show an increase of the SAR values near the eyes and some parts of the head at both GSM frequencies, when the metal-framed glasses are worn on the human head.

Bienkowski [14] used a PIFA antenna to investigate the influence of the dimension of the metal-framed spectacles on the SAR distribution in SAM's head. The results from his study show that the metal-framed spectacles can cause resonance for certain dimension at both GSM frequencies, which leads to an increase of the maximum SAR value up to 70%. However in his study the metal frames are not in contact with the human head and also the phone is not placed in a talk position, which does not reflect reality.

Another study conducted by Joó et al. [58] investigate the impact of the human head size on the SAR distribution when wearing metal-framed spectacles or implants. Their study shows a significant increase of the SAR values at 0.9 GHz when a child has a metal implant and at 2.1 GHz when a mobile phone is vertically positioned next to an adult's head. Also their results show an increase of the SAR values in the human head when the metal-framed spectacles are considered. However, the mobile phone used in this study does not represent a real mobile phone.

The increase of the maximum SAR value when the metal-framed spectacles are considered is also shown by Zhang et al. in [114]. In this study they used a real mobile phone and an inhomogeneous Chinese voxel human model.

Simulation Setup

The parameters for the simulations are setup with the same values as in Section 7.2.1. The two types of mobile phone (a foldable and a small phone) and the same HUGO model are also used in the simulation scenarios. The metal frames are modeled with dimensions that fit to the head of HUGO. In all simulation scenarios they are modeled by a perfect electric conductor (PEC). Figure 7.22 shows HUGO, the metal frames and the phones used in the simulations.

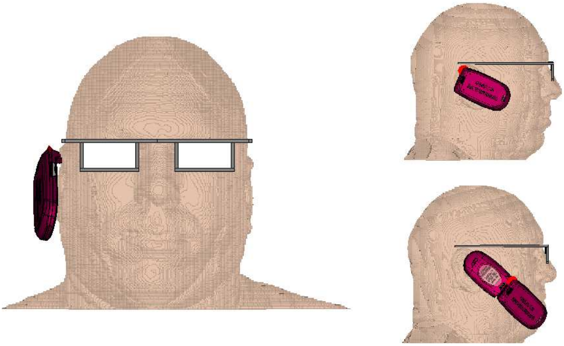

Figure 7.22.: HUGO model, metal-framed eyeglasses and two types of phones: a small phone (upper right) and a foldable phone (lower right picture)

Effect of Eyeglasses

Various realistic talk positions of the phones relative to the head are investigated to analyze the effect of wearing metal-framed eyeglasses. First, a foldable phone shown in Figure 7.22 is placed in a talk position. In this case, the results did not show any significant change in the SAR values when the metal frames are placed on the human head. This means that the antenna, which is placed in the lower part of the foldable phone, did not induce a current in the metal frames.

On the contrary, when the small phone is considered in the simulations, the results show that the position of the mobile phone has a strong impact on the SAR distribution as well as on the calculated maximum SAR values.

From several positions of the mobile phone, only the three most important (see Figure 7.23) are chosen to analyze their impact on the SAR distribution and the maximum SAR values when wearing metal-framed eyeglasses.

It is interesting to note the effect of wearing the eyeglasses depending on the phone's position. Namely, without the eyeglasses, the phone's position has a minor influence on the calculated SAR values, which is not the case when the eyeglasses are worn. On one hand, at a frequency of 0.9 GHz there is no significant change

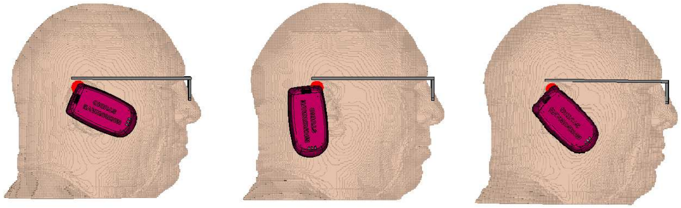

Figure 7.23.: Three positions of the mobile phone (Case1, Case2 and Case3 from left to right)

Table 7.3.: Maximum SAR values and SAR difference at 1.8 GHz, for the three positions of the mobile phone

Max SAR in W/kg	Case 1		Case 2		Case 3	
	(1g)	(10g)	(1g)	(10g)	(1g)	(10g)
Without eyeglasses	1.105	0.593	1.09	0.459	0.990	0.543
With eyeglasses	1.594	0.672	1.110	0.445	1.384	0.570
SAR diff (%)	44.25	13.32	1.83	-3.05	39.79	4.97

of the maximum SAR values when the metal-framed eyeglasses are considered (at most 5%). On the other hand, at a frequency of 1.8 GHz, there is a drastic increase of the maximum SAR values, which can be up to 44% when the metal-framed eyeglasses are worn. Table 7.3 shows the maximum SAR values calculated in the human head and the difference of the SAR values, at 1.8 GHz, with and without metal-framed eyeglasses.

From the results presented in Table 7.3 it can be seen that at 1.8 GHz, the averaging mass influences the difference between the maximum SAR values with and without glasses. Since the increase of the SAR values when the metal-framed eyeglasses are worn is a strongly localized effect, the maximum SAR values are higher when 1 g averaging mass is considered. In Case 1 and Case 3, the maximum 1g SAR values are almost close to each other and therefore only Case 1 is further analyzed in detail.

At 1.8 GHz, as shown in Table 7.3, the maximum 1g SAR value significantly increases when the metal-framed eyeglasses are considered. The maximum 1g SAR value appears near the end of the edge of the metal frames, as shown in Figure 7.24.

On the contrary, in Case 2, the presence of the metal frames does not cause any significant change of the maximum 1 g SAR value, which occurs in the middle

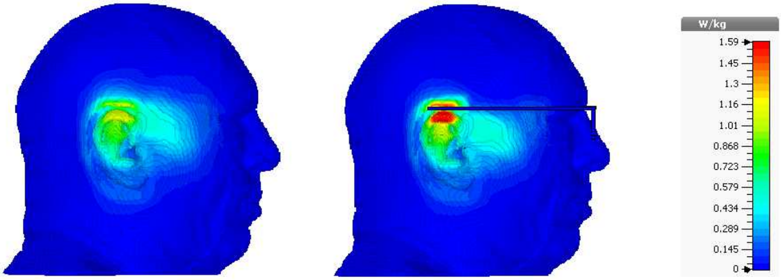

Figure 7.24.: Case1: SAR distribution at 1.8 GHz without eyeglasses (left) and with eyeglasses (right)

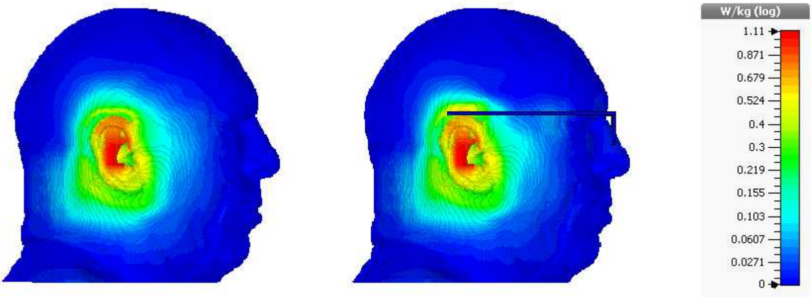

Figure 7.25.: Case2: SAR distribution at 1.8 GHz without eyeglasses (left) and with eyeglasses (right)

of the ear, both with and without metal frames (see Figure 7.25). However, it is interesting to notice that the maximum 10g SAR value decreases when the metal frames are worn.

Because the SAR results depend on the electric field strength, analysis of the electric field in the near field is conducted to support the obtained results from the simulations. Figure 7.26 and Figure 7.27 show the electric field at 1.8 GHz at 1 cm distance from the antenna both with and without metal-framed eyeglasses, for Case 1 and Case 2 respectively. In both figures it can be noticed that the position

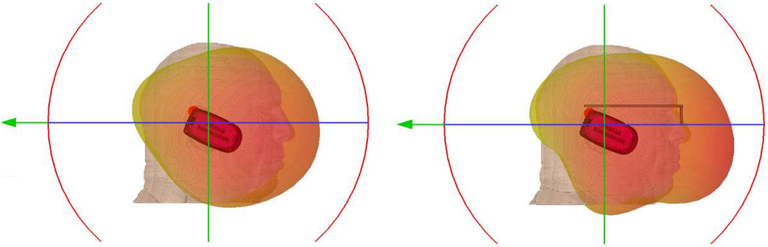

Figure 7.26.: Case1: Electric field at 1.8 GHz without metal-framed eyeglasses (left) and with metal-framed eyeglasses (right) at 1 cm distance from the antenna

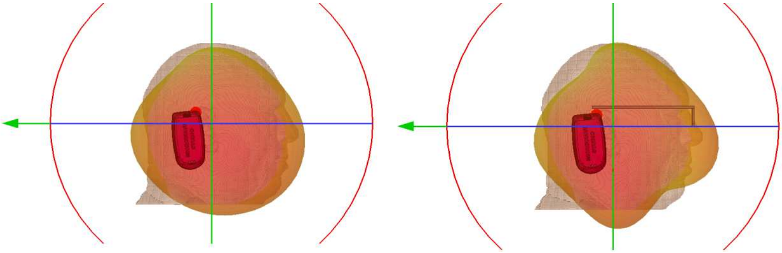

Figure 7.27.: Case2: Electric field at 1.8 GHz without metal-framed eyeglasses (left) and with metal-framed eyeglasses (right) at 1 cm distance from the antenna

of the phone as well as the presence of the eyeglasses impact the direction and the shape of the electric field pattern. On one hand, in Case 1, the presence of the metal frames in the model causes a significant change of the shape of the electric field pattern. On the other hand, in Case 2, there is only a very small change of the electric field pattern when wearing eyeglasses.
From the results obtained in this study it can be concluded that the position of the mobile phone has a huge impact on the SAR results when metal-framed eyeglasses are considered.

7.3 Influence of the Position of the Human Body on the SAR Distribution

This section describes how the geometry of the human model and its position influence the energy absorption from a fixed irradiation source. The human models are irradiated from the frontal side and in all simulations a plane wave is considered as an excitation source. The choice of the plane wave as an excitation source allows a good approximation of the electromagnetic field propagation in the far-field region. Additionally, when the human model is exposed to a plane wave and the electric field vector is parallel to the long body axis, the whole body averaged SAR reaches it maximum value [3].

The simulations are performed with the CST MICROWAVE STUDIO®[26]. In the simulations, open boundary conditions are set up. The intensity of the plane wave is 1 W/m^2. The frequency range in the simulation setup is from 0-300 MHz. This frequency range is chosen based on the recommendations from ICNIRP [3]. For an average not grounded human (height: 176 cm and weight: 73 kg) the resonant frequency is 70 MHz. This value varies depending on the size of the human model (it is lower for taller persons and higher for smaller ones). For analyzing of the results, electric field and power loss monitors are defined for the frequency range 50-100 MHz. Furthermore, SAR calculations are performed as a post-processing step.

Two groups of simulation scenarios are defined, depending on the position of the human models. Within these simulations, HUGO, Gustav and Laura are used as human models (see Figure 7.28). The HUGO model is used in the finest $1 \times 1 \times 1$ mm^3 resolution. The finest available resolutions for Gustav and Laura are $2.08 \times 2.08 \times 2$ mm^3 and $1.875 \times 1.875 \times 1.25$ mm^3, respectively. In the first group of simulations, the human models are in upright position. The second group of simulations includes the three human models in a sitting position. The goal of this simulations is to obtain the dependency of the whole body averaged SAR and the localized SAR distribution on the human model geometry and position. This analysis was already performed for the HUGO model by Gao [44].

Figures 7.29 and 7.30 show the localized SAR distribution in the human models in upright and sitting position, respectively. The SAR values are monitored for an averaging mass of 10 g at the frequency of 70 MHz, which is close to the resonant frequency. According to ICNIRP, the SAR limits given at the beginning of this chapter are defined for an averaging mass of 10 g and an incident plane wave with intensity of 10 W/m^2 for the occupational exposure and 2 W/m^2 for the public exposure. Most affected areas from the radiation with the plane wave differ for each human model. In upright position, a large portion of the electromagnetic energy is absorbed near the knees and ankles. Furthermore in comparison with HUGO, Gustav and Laura have more energy absorbed in the neck. Also near the nose it can be noticed that Laura has more energy absorbed compared to HUGO and Gustav. The maximum SAR values obtained from the simulations for the three models are: HUGO - 1.33 W/kg, Gustav - 0.4 W/kg and Laura - 0.45 W/kg. The SAR limits in the limbs defined by ICNIRP are 20 W/kg and 4 W/kg for exposure on a plane wave with an intensity of 10 W/m^2 and 2 W/m^2, respectively. In order to com-

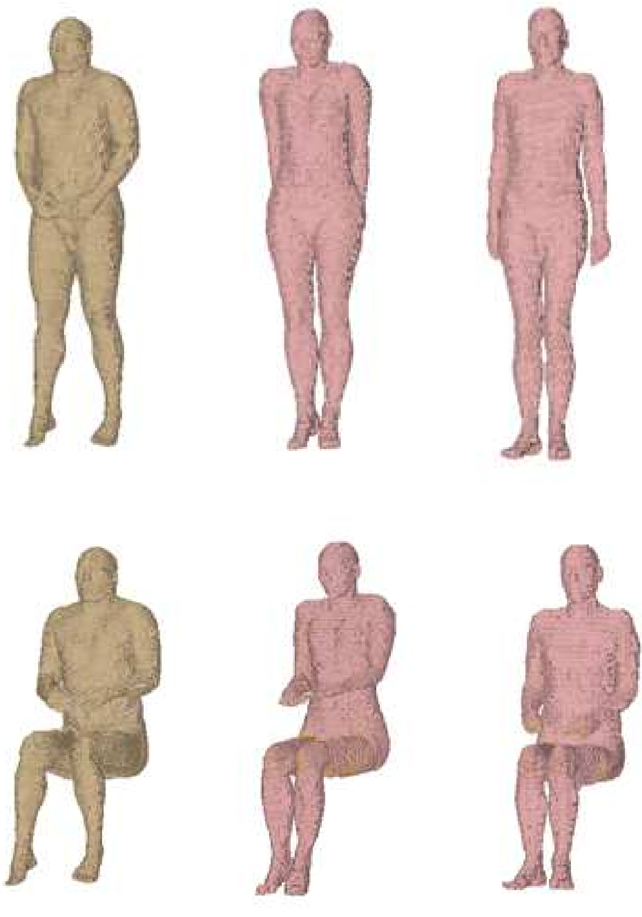

Figure 7.28.: Human models in upright position are shown in the upper figure. In the lower figure the human models are in sitting position

pare the obtained maximum SAR values to the ICNIRP prescribed one, they need to be multiplied by a factor of 10 and 2 respectively. For occupational and public exposure, the obtained SAR values are listed in the Table 7.4. This shows that the prescribed limits are not overestimated.

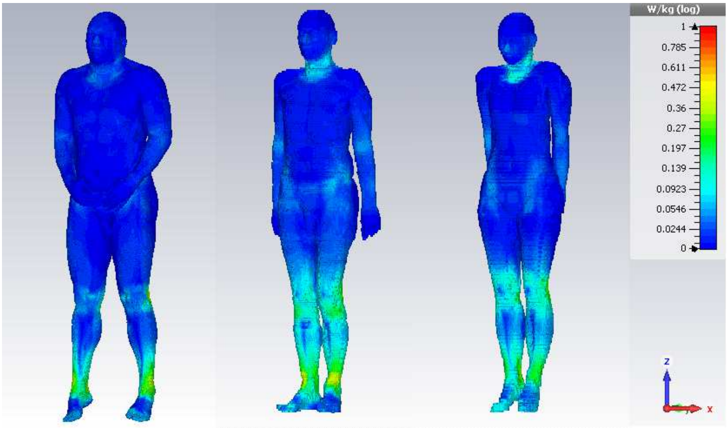

Figure 7.29.: Localized SAR distribution in the upright human models at frequency of 70 MHz and averaging mass of 10 g

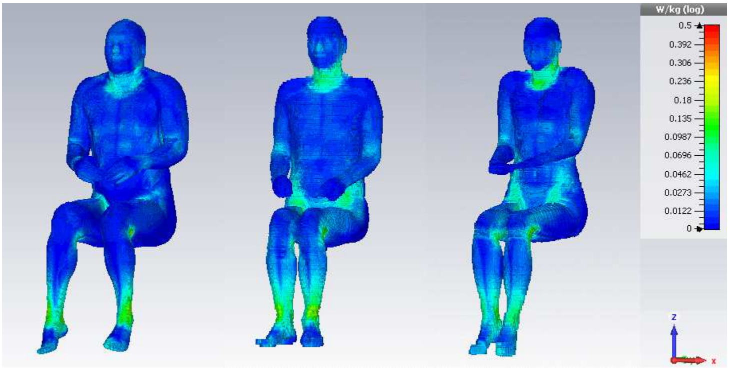

Figure 7.30.: Localized SAR distribution in the sitting human models at frequency of 70 MHz and averaging mass of 10 g

The human models in sitting position in Figure 7.30 have the most absorption of the electromagnetic energy in the areas near the ankles, knees, elbows, hips and neck. Opposite to the upright position of the human models, here can be noticed that HUGO and Gustav have significant portion of energy absorbed near the nose, which is not the case for Laura. However, the maximum SAR values for the human models in sitting position are twice lower compared to the same values

Table 7.4.: Localized SAR in the limbs for the three human models in upright position

Localized SAR (W/kg)	HUGO	Gustav	Laura	ICNIRP limit
Occupational exposure	13.3	4	4.5	20
General public exposure	2.6	0.8	0.9	4

Table 7.5.: Localized SAR in the limbs for the three human models in sitting position

Localized SAR (W/kg)	HUGO	Gustav	Laura	ICNIRP limit
Occupational exposure	6	2.3	2.5	20
General public exposure	1.2	0.4	0.5	4

for the human models in upright position. The following maximum SAR values are obtained from the simulations: HUGO - 0.6 W/kg, Gustav - 0.23 W/kg and Laura - 0.25 W/kg. For occupational and public exposure, the obtained SAR values are given in Table 7.5. As in the previous human body setup, the obtained results are lower than the prescribed SAR limits.

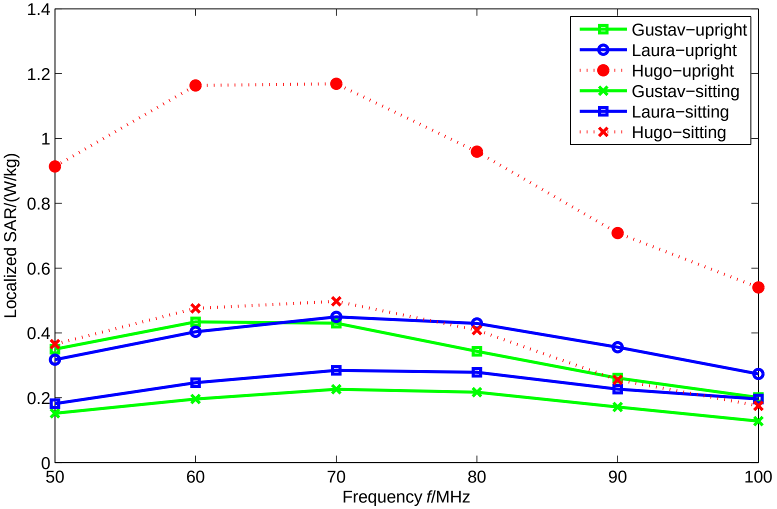

Figure 7.31.: Localized SAR at frequency range 50-100 MHz

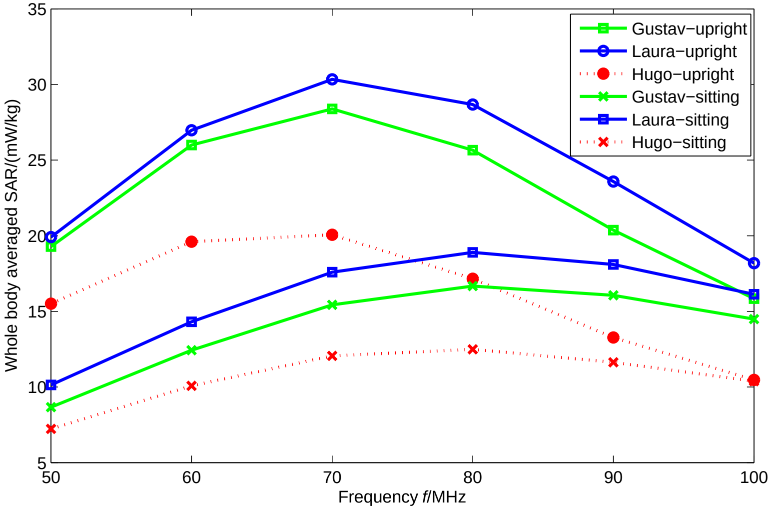

Figure 7.32.: Whole body averaged SAR at frequency range 50-100 MHz

Figure 7.31 shows the dependence of the maximum localized SAR values in the monitored frequency range (50-100 MHz). For all models, the maximum value is at 70 MHz and therefore the SAR distribution is analyzed at this frequency.
The relationship between the whole body averaged SAR and the frequency is shown on Figure 7.32. Here the resonant frequency for the human models in upright position is 70 MHz. However, when the human models are in sitting position, the resonant frequency is shifted to 80 MHz.

8 Summary and Outlook

This dissertation presents the enhancements of the poser program “BodyFlex” to generate a set of voxel-based human models in different postures. The aim of the dissertation is to develop effective methods for intuitive deformation of the human body parts combining existing deformation techniques while preserving the correct anatomy of the human body.
A variety of simulation scenarios presented in Chapter 7 show realistic electromagnetic application of the deformed human models. This chapter gives a brief summary of the main points in the dissertation and an outlook for possible future research related to this work.

8.1 Summary

In this dissertation, the main achievements are the enhancements of the poser program “BodyFlex” related to the deformation of the human model as well as the performance of the software. The enhanced main modules are: generate control points and lattices around the body parts and deform the original human model with the FFD and EFFD techniques. One optional module to scale the human voxel model in order to obtain a human model with different size is also added to “BodyFlex” .
In order to generate the control points and lattices around the different body parts, the joints are first defined using the Voxel Model Observer (VMO) [85]. Based on the joint positions, an automatic placement of the control points to build the control lattices around almost all body parts is performed. As the variety of human body models leads to huge manual effort for definition of such control lattices, the automation of this process is of a high importance. An exception is only the elbow control lattice, because of the various initial positions of this body part in different human models.
Because in the first version of “BodyFlex” not all body parts could be deformed, two enhancements are introduced. The first enhancement is the algorithm for moving of non-axis aligned body parts. The second enhancement is the numerical approach for the separation and movement of the fingers of the HUGO model. Before the movement of the fingers movement takes place, an algorithm for separating the fingers based on geometrical techniques is applied, which allows determining of

the voxels that belong to a certain finger. Later, control lattices used during the deformation process are defined, which are aligned with the position of the fingers in the original model. This separation and movement of the fingers and the hand is important for generation of a proper posture of the HUGO model for evaluating the electromagnetic effects from mobile phones.

Another enhancement introduced in this dissertation is the elbow deformation using the EFFD technique. The control lattice is built from two arbitrary shaped non-axis aligned hexahedrons, to fit with the initial position of the elbow. Connecting the two deformation techniques, FFD and EFFD, leads to a successful deformation of the body parts, while using different shapes of control lattices.

An algorithm for fast export of human models, based on the sparse matrix logic is developed in this work. Since after the deformation of the human voxel, the whole space is voxelized with the same resolution as the initial one, it might happen that multiple voxels from the initial dataset map to one voxel in the export dataset, resulting in a voxel with several tissue IDs. In this case, the decision which tissue ID should be assigned to the voxel is based on finding the most often occurring tissue ID in that voxel. Therefore a sparse matrix in compressed form is used to keep the voxel index in the export dataset, the tissue IDs that it contains and their occurrence. The new export function which works with the proposed algorithm occupies three times less memory and works twice as fast than the old one.

In order to improve the performance of “BodyFlex” the posture and the export process are partially parallelized using OpenMP®. The results obtained on an eight core CPU showed that the calculation of the voxel positions during posturing with eight threads, is almost twice as fast as the calculation with only one thread. Regarding the export of the human model, the calculation with eight threads is almost five times faster than the calculation with one thread. From the results obtained, it can be concluded that parallel execution drastically shortens the time for large datasets.

A comparative analysis of the performance of “BodyFlex” and other commercial softwares for posturing human models is also performed within this dissertation. The performances of each software are analyzed in terms of time for posturing of the human model and the memory occupation. The results showed that “BodyFlex” has many advantages over the tested softwares concerning the anatomic correctness of the deformed models. Regarding the performance, in certain cases “BodyFlex” occupies more memory than the other softwares, but it is still at an acceptable level. However, “BodyFlex” is the fastest in terms of the time to posture the human model.

In this dissertation various simulation scenarios are established to investigate the impact of the electromagnetic fields on original and postured human models. At the beginning, a study of the position of the hand and fingers of the human model is performed to determine their influence on the SAR distribution due to mobile phone radiation. First, a solid hand and a heterogeneous hand with several tissues together with SAM and the HUGO model are used in two simulation scenarios: in the first scenario, the mobile phone is not held by the hand (there is no hand in the simulation) and in the second scenario, the hand is placed behind the mobile phone. The results observed at GSM frequencies, i.e. 0.9 and 1.8 GHz, showed a difference between the SAR values computed for the SAM and the HUGO model. The maximal SAR value in HUGO's head decreases in case when the hand is present. In this case, a large part of the energy is absorbed by the hand. Additionally, if the mobile phone is held in HUGO's hand, the area of SAR distribution as well as the maximum SAR value in the head are significantly smaller compared to the two previous cases. Therefore, it is important to consider the hand of the human model for computation of the SAR values.

Another study in this dissertation considers the impact of rings and earrings on the SAR distribution due to mobile phone exposure. Two types of mobile phones are used in the simulation: a foldable and a small phone. Three different shapes of gold earrings are observed: rhomboidal, straight and creole. The results obtained for the earrings did not show any significant effect on the SAR distribution except for the creole shape. Namely, when the creole earring has circumference of $\sim 1\lambda$ the SAR values increase in the tissues on the surface of the human head. At the same time, the SAR values in the head decrease compared to the simulation results without the earring. This result is obtained using the small phone in the simulations.

Also, the SAR results for two positions of the golden ring are analyzed: ring placed on the index and ring on the ring finger. The results showed that wearing the ring on the index finger when the small phone is used, significantly increases the maximum SAR value (by a factor of 3) obtained in the index finger, near the ring. However, the presence of the ring in the simulation does not have any significant influence on the SAR distribution in the head compared to the simulation results without the ring. Wearing the ring on the ring finger has a significant effect on the maximum SAR value which appears in the hand when the foldable phone is used. Namely, in this case, the SAR value in the ring finger increases by a factor of 4 when the ring is worn.

One more realistic electromagnetic application concerns the impact of eyeglasses on the SAR distribution. The metal frames are modeled using a perfect electric conductor (PEC), such that they fit to the shape of the head of the HUGO model. The same two types of mobile phones are used in the simulations: a foldable and a small phone. The results obtained for the foldable phone are not affected whether the metallic frames are placed on the human head or not. However, when the small phone is used in the simulation, the results at the frequency of 1.8 GHz showed that the difference between the maximum SAR values in both cases (wearing the metallic frames or not) can be of up to 44% depending on the position of the mobile phone.

The last electromagnetic application example shows the influence of the position and the geometry of human bodies on the SAR distribution. Three human models with different sizes are frontally irradiated with an incident plane wave. The whole body averaged SAR and the localized SAR distribution are calculated for human models in upright and sitting position, exposed to radio-frequency electromagnetic fields in the range from 0 MHz to 300 MHz. The results showed a diversity in the SAR distribution between the human models, which is related not only to the position in which they are, but also to their geometry.

8.2 Outlook

In this section, potential research ideas and remarks related to this dissertation are given.

- Use the poser program “BodyFlex” to deform child voxel models.
- Fully automate the semi-automatic placement of EFFD lattice at the elbow to automatic.
- Use some existing techniques to prevent intersection between tissues after deformation [59],[98].
- Generate human voxel models using “BodyFlex” for further electromagnetic applications, like effects of implants or wearable devices on the SAR distribution for various human postures. Also, thermal analysis of implants or wearable devices is another interesting research topic.

A Appendix

A.1 Newton's method

Algorithm 1 Newton's method

```
function NewtonMethod($v_0, \alpha, \beta, \gamma, p$)
    $N \leftarrow 100$                                      ▷ Max number of iterations
    $tol \leftarrow 1e-04$                                  ▷ Tolerance
    $max \leftarrow 10000$                                  ▷ Value for divergence
    $fl \leftarrow 0$            ▷ Flag to control if under-relaxation is necessairy
    $v_s \leftarrow v_0$
    while $N > 0$ do                                        ▷ We have the answer if r is 0
        Jacobian($v_s, \alpha, \beta, \gamma, JJ$)          ▷ The Jacobian matrix is saved in JJ
        if $|JJ| = 0$ then
            Jacobian is singular - try new guess!
        end if
        FuncF($v_s, \alpha, \beta, \gamma, p, r$)           ▷ r-result of the evaluation of F
        $iJJ \leftarrow JJ^{-1}$
        if $fl = 0$ then
            $v_n = v_s - iJJ \cdot r$
        else
            $v_n = v_s - c \cdot iJJ \cdot r$
        end if
        FuncF($v_n, \alpha, \beta, \gamma, p, r1$)          ▷ r1-result of the evaluation of F
        if $|r1| < tol$ then
            $v_e = v_n$
            break;
        end if
        if $|r1| > max$ then
            $fl \leftarrow 1$
            $c \leftarrow c - 0.1$
            $v_s = v_0$
            $v_e = v_s$
            $N \leftarrow 101$
        end if
        $N \leftarrow N - 1$
        $v_s \leftarrow v_e$
    end while
    if $N < 0$ then
        Maximum number of iterations reached!
        exit
    end if
    return $v_e$                                            ▷ The result is $v_e$
end function
```

A.2 Anatomical whole-body human models

Table A.1.: Anatomical whole-body human models listed by IEEE-ICES [60]

Model	Ref	Height (m)	Weight(kg)	Race	Age	Sex	Data format, voxel resolution	Comment	Available from
Child	[86][112]	1.15	21.7	Caucasian	7 y	F	$1.54x1.54x8mm^3$	Small for age	www.cst.com www.ascension.de
Baby	[86][112]	0.57	4.2	Caucasian	8 w	F	$0.85x0.85x4mm^3$		www.cst.com www.ascension.de
VoxelMan	[115]			Caucasian	adult	M		Head and torso	
Norman	[32] [57]			Caucasian	adult	M		only 10 ribs	
Golem	[86][112]	1.76	68.9	Caucasian	38 y	M	$2.08x2.08x8mm^3$		www.cst.com www.ascension.de
Visible-human	[96]			Caucasian	38 y	M	various	One testicle only	www.speag.com www.remcom.com
Frank	[86][112]	1.74	95	Caucasian	48 y	M	$0.74x0.74x5mm^3$	head and torso	
Donna	[86][112]	1.70	79	Caucasian	40 y	F	$1.875x1.875x10mm^3$		www.cst.com www.ascension.de
Helga	[86][112]	1.70	81	Caucasian	26 y	F	$0.98x0.98x10mm^3$		www.cst.com www.ascension.de
Irene	[86][112]	1.63	51	Caucasian	32 y	F	$1.875x1.875x5mm^3$		
Max	[64]			Caucasian	adult	M		VoxelMan adapted to dimensions of reference man	
Nagaoka man	[79]			Asian	22 y	M	$2x2x2mm^3$		
Nagaoka woman	[79]			Asian	22 y	F	$2x2x2mm^3$		
Naomi	[31]			Caucasian	23 y	F			
Katja	[13]	1.63	62.3	Caucasian	43 y	F	$1.775x1.775x4.8mm^3$	Pregnant (24th week)	www.cst.com www.ascension.de
Roberta	[22]	1.08	17.6	Caucasian	5 y	F	CAD, $0.5x0.5x0.5mm^3$ or better		www.itis.ethz.ch
Thelonious	[21]	1.17	19.5	Caucasian	6 y	M	CAD, $0.5x0.5x0.5mm^3$ or better		www.itis.ethz.ch
Eartha	[22]	1.35	30.3	Caucasian	8 y	F	CAD, $0.5x0.5x0.5mm^3$ or better		www.itis.ethz.ch
Dizzie	[22]	1.40	26.2	Caucasian	8 y	M	CAD, $0.5x0.5x0.5mm^3$ or better		www.itis.ethz.ch
Billie	[21]	1.46	35.6	Caucasian	11 y	F	CAD, $0.5x0.5x0.5mm^3$ or better		www.itis.ethz.ch
Louis	[22]	1.69	49.9	Caucasian	14 y	M	CAD, $0.5x0.5x0.5mm^3$ or better		www.itis.ethz.ch
Ella	[21]	1.60	58	Caucasian	26 y	F	CAD, $0.5x0.5x0.5mm^3$ or better		www.itis.ethz.ch
Duke	[21]	1.74	70	Caucasian	34 y	M	CAD, $0.5x0.5x0.5mm^3$ or better		www.itis.ethz.ch www.virtualman.info
Ella (pregnant)	[16]	1.60		Caucasian	26 y	F	CAD 3rd, 7th and 9th gestational month		www.speag.com
Fats		1.78	120	Caucasian	37 y	M	CAD		www.speag.com
Chinese Male	[111]	1.72	63.05	Asian	35 y	M	$1x1x1mm^3$		
Chinese Female	[111]	1.62	53.5	Asian	22 y	F	$1x1x1mm^3$		
VHP-F	[83] [34]	1.73	75	Caucasian	60 y	F	Variable. Average: $2x2x2mm^3$	Visible Human Data Source. Variable Fat Layer	www.nevaelectromagnetics.com/MWO.html

B Register

List of Figures

Acronyms

API	Application Programming Interface
CENELEC	European Committee for Electrotechnical Standardization
CPU	Central Processing Unit
CT	Computer Tomography
CTIA	Cellular Telecommunication Industry Association
DFFD	Dirichlet Free Form Deformation
EFFD	Extended Free Form Deformation technique
FCC	Federal Communications Commission
FDTD	Finite-Difference Time-Domain Method
FEM	Finite Element Method
FFD	Free Form Deformation technique
FIT	Finite Integration Technique
FVM	Finite Volume Method
GSM	Global System for Mobile Communications
GUI	Graphical User Interface
ICNIRP	International Commission on Non-ionizing Radiation Protection
ICRP	International Commission on Radiological Protection
ICES	International Committee on Electromagnetic Safety
IEEE	Institute of Electrical and Electronics Engineers
LBS	Linear Blend Skinning
LCS	Local Coordinate System

MC	Marching Cubes
MCP	Metacarpophalangeal
MFC	Microsoft Foundation Class
MoM	Method of Moments
MR	Magnetic Resonance
MRI	Magnetic Resonance Imaging
PEC	Perfect Electric Conductor
PIFA	Planar inverted-F Antenna
PSD	Pose Space Deformation
psSAR	peak spatial-average Specific Absorption Rate
RAM	Random Access Memory
SAM	Specific Anthropomorphic Mannequin
SAR	Specific Absorption Rate
SPECT	Single-Photon Emission Computed Tomography
SSD	Skeleton Subspace Deformation
TSL	Tissue Simulating Liquid
UMTS	Universal Mobile Telecommunications System
XML	Extensible Markup Language
VHP	Visible Human Project
VMO	Voxel Model Observer

List of Symbols

A	primary grid facets
$\widetilde{A}$	dual grid facets
$\vec{B}$	magnetic flux density
$\overset{\frown}{\overset{\frown}{b}}$	magnetic facet flux
$\mathbf{C},\widetilde{\mathbf{C}}$	curl matrix on the primary/dual grid

c_0	speed of light in vacuum
$\vec{D}$	electric flux density
$\overset{\frown}{\overset{\frown}{d}}$	electric facet flux
$\vec{E}$	electric field strength
$\overset{\frown}{e}$	electric edge voltage
G	primary grid
$\tilde{G}$	dual grid
$\vec{H}$	magnetic field strength
$\overset{\frown}{h}$	magnetic edge voltage
$\vec{J}, \vec{J}_\kappa, \vec{J}_c, \vec{J}_i$	total, conduction, convection, impressed current density
L	primary grid edges
$\tilde{L}$	dual grid edges
$\vec{M}$	magnetic dipole moment density
$\vec{P}$	electric dipole moment density
P	primary grid nodes
$\tilde{P}$	dual grid nodes
$\vec{r}$	spatial variable
$\mathbf{R}_x$, $\mathbf{R}_y$, $\mathbf{R}_z$, $\mathbf{R}_{xyz}$	rotation matrices

$\mathbf{RT}$, $\mathbf{RTT}$	transformation matrices
$\mathbf{S}$,$\widetilde{\mathbf{S}}$	divergence matrix on the primary/dual grid
t	temporal variable
$\mathbf{T}$, $\mathbf{TL}$	translation matrices
V	primary grid cell
$\widetilde{V}$	dual grid cell
ε	permittivity
$\underline{\varepsilon}$, ε_r, ε_0	complex, relative, vacuum permittivity
μ	permeability
$\underline{\mu}$, μ_r, μ_0	complex, relative, vacuum permeability
ρ	electric charge density
σ	conductivity
σ_i	static ionic conductivity
τ	time constant
ω	angular frequency
Ω	computational domain

Bibliography

[1] “IEEE recommended practice for measurements and computations of radio frequency electromagnetic fields with respect to human exposure to such fields,100 kHz-300 GHz,” *IEEE Std C95.3-2002 (Revision of IEEE Std C95.3-1991)*, 2002. (Cited on page 102.)

[2] “IEEE standard for safety levels with respect to human exposure to radio frequency electromagnetic fields, 3 kHz to 300 GHz,” *IEEE Std C95.1-2005 (Revision of IEEE Std C95.1-1991)*, pp. 1–238, 2006. (Cited on pages 7 and 98.)

[3] “ICNIRP statement on the guidelines for limiting exposure to time-varying electric, magnetic, and electromagnetic fields (up to 300 GHz),” *Health Physics*, vol. 97, no. 3, pp. 257–259, 2009. (Cited on pages 7, 98, and 120.)

[4] M. J. Ackerman, “The visible human project,” *IEEE Proceedings*, vol. 86, no. 3, pp. 504–511, 1998. (Cited on page 12.)

[5] S. J. Allen, E. R. Adair, K. S. Mylacraine, W. Hurt, and J. Ziriax, “Empirical and theoretical dosimetry in support of whole body radio frequency (RF) exposure in seated human volunteers at 220 MHz,” *Bioelectromagnetics*, vol. 26(6), pp. 440–447, Sept 2005. (Cited on page 6.)

[6] K. E. Atkinson, *An introduction to numerical analysis*. John Wiley and Sons Inc., 1989. (Cited on page 26.)

[7] Q. Balzano, O. Garay, and J. Manning, T.J., “Electromagnetic energy exposure of simulated users of portable cellular telephones,” *Vehicular Technology, IEEE Transactions on*, vol. 44, no. 3, pp. 390–403, Aug 1995. (Cited on page 100.)

[8] A. Barchanski, M. Clemens, E. Gjonaj, H. De Gersem, and T. Weiland, “Large-scale calculation of low-frequency-induced currents in high-resolution human body models,” *IEEE Transactions on Magnetics*, vol. 43, no. 4, pp. 1693–1696, 2007. (Cited on page 13.)

[9] A. Barchanski, M. Clemens, T. Steiner, H. De Gersem, and T. Weiland, “Using domain decomposition techniques for the calculation of low-frequency electric current densities in high-resolution 3D human anatomy models,” *COMPEL: The International Journal for Computation and Mathematics in Electrical and Electronic Engineering*, vol. 24, no. 2, pp. 458–467, 2005. (Cited on page 13.)

[10] A. Barchanski, H. De Gersem, E. Gjonaj, and T. Weiland, “Impact of the displacement current on low-frequency electromagnetic fields computed using highresolution anatomy models,” *Physics in Medicine in Biology*, vol. 50, no. 19, pp. 243–249, 2005. (Cited on page 13.)

[11] A. Barchanski, T. Steiner, H. De Gersem, M. Clemens, and T. Weiland, “Local grid refinement for low-frequency current computations in 3-D human anatomy models,” *IEEE Transactions on Magnetics*, vol. 42, no. 4, pp. 1371–1374, 2006. (Cited on page 13.)

[12] A. H. Barr, “Global and local deformations of solid primitives,” *SIGGRAPH Comput. Graph.*, vol. 18, no. 3, pp. 21–30, Jan. 1984. [Online]. Available: http://doi.acm.org/10.1145/964965.808573 (Cited on page 19.)

[13] J. Becker, M. Zankl, U. Fill, and C. Hoeschen, “Katja - the 24th week of virtual pregnancy for dosimetric calculations,” *Polish Journal of Medical Physics and Engineering*, vol. 14(1), pp. 13–19, 2008. (Cited on pages 11 and 132.)

[14] P. Bieńkowski and P. Cała, “Influence of metallic spectacle frame on SAR in the head of a mobile phone user,” *PRZEGLĄD ELEKTROTECHNICZNY*, vol. 89, no. 12, pp. 353–355, 2013. (Cited on page 115.)

[15] P. Bourke. Rotation about an arbitrary axis (3 dimensions). [Online]. Available: http://paulbourke.net/geometry/rotate/ (Cited on page 55.)

[16] E. Cabot, A. Christ, B. Buhlmann, M. Zefferer, N. Chavannes, G. C. van Rhoon, and N. Kuster, “Quantification of the rf exposure of the foetus using anatomical cad models in three different gestational phases,” *Health Physics*, vol. 107(5), pp. 369–381, 2014. (Cited on pages 11 and 132.)

[17] M. Caon, “Voxel-based computational models of real human anatomy: a review,” *Radiation and Environmental Biophysics*, vol. 42, no. 4, pp. 229–235, 2004. [Online]. Available: http://dx.doi.org/10.1007/s00411-003-0221-8 (Cited on page 10.)

[18] B. Chapman, G. Jost, and R. van der Pas, *Using OpenMP: Portable Shared Memory Parallel Programming*. MIT Press, 2008, no. v. 10. (Cited on page 77.)

[19] W. Chen, J. Poston, and G. Warner, *An evaluation of the distribution of absorbed dose in child phantoms exposed to diagnostic medical X rays*. Oak Ridge TN, USA: Oak Ridge National Laboratory, 1978. (Cited on page 10.)

[20] E. Cherubini, N. Chavannes, and N. Kuster, "Realistic skeleton based deformation of high-resolution anatomical human models for electromagnetic simulation," *The 31st Annual Meeting of the Bioelectromagnetic Society*, 2009. (Cited on page 88.)

[21] A. Christ, W. Kainz, E. G. Hahn, K. Honegger, M. Zefferer, E. Neufeld, W. Rascher, R. Janka, W. Bautz, J. Chen, B. Kiefer, P. Schmitt, H. P. Hollenbach, J. X. Shen, M. Oberle, D. Szczerba, A. Kam, J. W. Guag, and N. Kuster, "The virtual family - development of surface based anatomical models of two adults and two children for dosimetric simulations," *Physics in Medicine and Biology*, vol. 55, no. N23, 2010. (Cited on pages 11, 88, and 132.)

[22] A. Christ, G. Schmid, R. Djafarzadeh, R. Ueberbacher, S. Cecil, M. Zefferer, E. Neufeld, M. Lichtsteiner, M. Bouterfas, and N. Kuster, "Numerische Bestimmung der spezifischen Absorptionsrate bei Ganzkörperexposition von Kindern: Abschlussbericht," IT'IS Foundation, Zurich, Switzerland, Tech. Rep., Jul. 2009. (Cited on pages 11 and 132.)

[23] M. Christy, *Mathematical phantoms representing children of various ages for use in estimates of internal dose*. Oak Ridge TN, USA: Oak Ridge National Laboratory, 1980. (Cited on page 10.)

[24] M. Clemens and T. Weiland, "Discrete electromagnetism with the finite integration technique," *Progress In Electromagnetics Research*, vol. 32, pp. 65–87, 2001. (Cited on page 36.)

[25] E. S. Cobb, "Design of sculptured surfaces using the B-spline representation," Ph.D. dissertation, The University of Utah, 1984. (Cited on page 20.)

[26] Computer Simulation Technology AG. (2012) CST STUDIO SUITE version 2012. [Online]. Available: http://www.cst.com (Cited on pages 99, 100, 102, 106, and 120.)

[27] S. Coquillart, “Extended free-form deformation: a sculpturing tool for 3D geometric modeling,” *ACM SIGGRAPH Computer Graphics*, vol. 24(4), pp. 187–196, Aug 1990. (Cited on pages 7, 20, 23, 24, and 134.)

[28] M. David. Skeletal series part 8: The human hand. [Online]. Available: http://thebonesofmine.wordpress.com/2011/07/17/skeletal-series-part-8-the-human-hand/ (Cited on pages 62 and 135.)

[29] O. R. Davis and R. P. Burton, “Free-form deformation as an interactive modeling tool,” *Journal of Imaging Technology*, vol. 17, no. 4, pp. 181–187, 1991. (Cited on page 22.)

[30] T. W. Dawson, K. Caputa, , and M. A. Stuchly, “Numerical evaluation of 60 Hz magnetic induction in the human body in complex occupational environments,” *Phys. Med. Biol.*, vol. 44(4), pp. 1025–1040, Apr 1999. (Cited on page 6.)

[31] P. Dimbylow, “Development of the female voxel phantom, NAOMI, and its application to calculations of induced current densities and electric fields from applied low frequency magnetic and electric fields,” *Physics in Medicine in Biology*, vol. 50, pp. 1047–1070, 2005. (Cited on pages 6, 11, and 132.)

[32] P. J. Dimbylow, “FDTD calculations of the whole-body averaged SAR in an anatomically realistic voxel model of the human body from 1 MHz to 1 GHz,” *Physics in Medicine in Biology*, vol. 42, pp. 479–490, 1997. (Cited on pages 6, 11, and 132.)

[33] Dipp GmbH. (2013, Apr) Anatomical volume data sets. [Online]. Available: http://www.vr-laboratory.com (Cited on pages 7 and 13.)

[34] J. M. Elloian, G. M. Noetscher, S. N. Makarov, and A. Pascual-Leone, “Continuous wave simulations on the propagation of electromagnetic fields through the human head,” *IEEE Transactions on bio-medical engineering*, vol. 61(6), pp. 1676–1683, 2014. (Cited on page 132.)

[35] E. J. Farrell, “Color display and interactive interpretation of three dimensional data,” *IBM Journal of Research and Development*, vol. 27, no. 4, pp. 356–366, 1983. (Cited on page 30.)

[36] FCC. (2016) Specific absorption rate SAR for cellular telephones. [Online]. Available: https://www.fcc.gov/general/specific-absorption-rate-sar-cellular-telephones (Cited on page 99.)

[37] C. C. T. P. for Mobile Station Over the Air Performance, “Method of measurement for radiated RF power and receiver performance,” *Rev*, vol. 3.1, 2011. (Cited on page 101.)

[38] C. Gabriel and S. Gabriel, “Compilation of the dielectric properties of body tissues at RF and microwave frequencies,” U.S. Air Force Report AFOSR-TR-96, London, Tech. Rep., 1996. (Cited on page 18.)

[39] C. Gabriel, S. Gabriel, and E. Corthout, “The dielectric properties of biological tissues: I. literature survey,” *Physics in Medicine in Biology*, vol. 41, pp. 2231–2249, 1996. (Cited on page 16.)

[40] S. Gabriel, R. W. Lau, and C. Gabriel, “The dielectric properties of biological tissues: II. measurements in the frequency range 10 Hz to 20 GHz,” *Physics in Medicine in Biology*, vol. 41, no. 11, pp. 2251–2269, 1996. (Cited on page 16.)

[41] ——, “The dielectric properties of biological tissues: III. parametric models for the dielectric spectrum of tissues,” *Physics in Medicine in Biology*, vol. 41, no. 11, pp. 2271–2293, 1996. (Cited on page 17.)

[42] J. E. Gain and D. Bechmann, “A survey of spatial deformation from a user-centered perspective.” *ACM Trans. Graph.*, vol. 27, no. 4, pp. 1–21, 2008. (Cited on page 20.)

[43] J. Gao, I. Munteanu, W. Müller, and T. Weiland, “Generation of postured voxel-based human models for the study of step voltage excited by lightning current,” *Advances in Radio Science*, vol. 9, pp. 99–105, 2011. (Cited on page 13.)

[44] J. Gao, “Generation of postured voxel-based human models used for electromagnetic applications,” Ph.D. dissertation, Technische Universität, Darmstadt, January 2012. (Cited on pages 7, 14, 19, 20, 30, 31, 42, 44, 47, 49, 50, 67, 72, 74, 76, 120, and 134.)

[45] E. Gjonaj, M. Bartsch, M. Clemens, S. Schupp, and T. Weiland, “High-resolution human anatomy models for advanced electromagnetic field computations,” *IEEE Trans. Magn.*, vol. 38, no. 2, pp. 357–360, 2002. (Cited on page 13.)

[46] M.-C. Gosselin, E. Neufeld, H. Moser, E. Huber, S. Farcito, L. Gerber, M. Jedensjö, I. Hilber, F. D. Gennaro, B. Lloyd, E. Cherubini, D. Szczerba,

W. Kainz, and N. Kuster, "Development of a new generation of high-resolution anatomical models for medical device evaluation: the virtual population 3.0," *Physics in Medicine and Biology*, vol. 59, no. 18, p. 5287, 2014. [Online]. Available: http://stacks.iop.org/0031-9155/59/i=18/a=5287 (Cited on page 10.)

[47] J. Griessmair and W. Purgathofer, "Deformation of solids with trivariate B-splines," in *Proceedings of Eurographics*, vol. 89, sep 1989, pp. 137–148. (Cited on page 22.)

[48] E. M. Haacke, R. W. Brown, M. R. Thompson, and R. Venkatesan, *Magnetic Resonance Imaging: Physical Principles and Sequence Design*. John Wiley and Sons Inc., 1999. (Cited on page 12.)

[49] G. T. Herman, *Fundamentals of Computerized Tomography:Image Reconstruction from Projections*. Springer-Verlag London, 2009. (Cited on page 12.)

[50] G. T. Herman and J. K. Udupa, "Display of 3D digital images: Computational foundations and medical applications," *IEEE Computer Graphics and Applications*, vol. 3, no. 5, pp. 39–46, 1983. (Cited on page 30.)

[51] C. A. R. Hoare, "Algorithm 64: Quicksort," *Commun. ACM*, vol. 4, no. 7, Jul. 1961. (Cited on page 76.)

[52] J. Hwang, R. Shoup, and J. Poston, *Mathematical description of a one- and five-year-old child for use in dosimetry calculations*. Oak Ridge TN, USA: Oak Ridge National Laboratory, 1976. (Cited on page 10.)

[53] ICRP, *Publication 66. Human respiratory tract model for radiological protection. Annals of the ICRP 24*, Pergamon,Oxford, 1994. (Cited on page 10.)

[54] IEC, "Human exposure to radio frequency fields from hand-held and body-mounted wireless communication devices - human models, instrumentation, and procedures - part 1: Procedure to determine the specific absorption rate (SAR) for hand-held devices used in close proximity to the ear (frequency range of 300 MHz to 3 GHz)," *IEC 62209-1:2005*, 2005. (Cited on page 99.)

[55] M. T. Islam, H. Z. Abidin, M. R. I. Faruque, and N. Misran, "Analysis of materials effects on radio frequency electromagnetic fields in human head," *Progress In Electromagnetics Research*, vol. 128, pp. 121–136, 2012. (Cited on page 108.)

[56] ITIS Foundation. (2014) Virtual Population. [Online]. Available: http://www.itis.ethz.ch/news-events/news/virtual-population/ (Cited on page 88.)

[57] D. G. Jones, “A realistic anthropomorphic phantom for calculating organ doses arising from external photon irradiation,” *Radiation Protection Dosimetry*, vol. 72, pp. 21–29, 1997. (Cited on pages 11 and 132.)

[58] E. Joo, A. Szasz, and P. Szendro, “Metal-framed spectacles and implants and specific absorption rate among adults and children using mobile phones at 900/1800/2100 MHz,” *Electromagn Biol Med*, vol. 25, no. 2, pp. 103–112, 2006. (Cited on page 115.)

[59] S. Jung, M. Hong, and M.-H. Choi, *Free-Form Deformation Axis Aligned Bounding Box*. Berlin, Heidelberg: Springer Berlin Heidelberg, 2009, pp. 804–813. [Online]. Available: http://dx.doi.org/10.1007/978-3-642-02617-1_82 (Cited on page 128.)

[60] W. Kainz, M. Douglas, R. Bodemann, R. Petersen, and D. Heirman. International committee on electromagnetic safety, technical committee 34: Wireless handset SAR certification: List of anatomical whole body models. [Online]. Available: http://grouper.ieee.org/groups/scc34/sc2/ (Cited on pages 11 and 132.)

[61] P. Kalra, A. Mangili, N. M. Thalmann, and D. Thalmann, “Simulation of facial muscle actions based on rational free form deformations,” in *Computer Graphics Forum(Eurographics 92)*, vol. 11, no. 3, 1992, pp. 59–69. (Cited on page 22.)

[62] V. J. Katz, “The history of Stokes’ theorem,” M. Anderson, V. Katz, and R. Wilson, Eds. Mathematical Association of America, 2009, pp. 78–87. (Cited on page 34.)

[63] E. Keppel, “Approximating complex surfaces by triangulation of contour lines,” *IBM Journal of Research and Development*, vol. 19, no. 1, pp. 2–11, 1975. (Cited on page 30.)

[64] R. Kramer, J. W. Vieira, H. J. Khoury, F. de Andrade Lima, and D. Fuelle, “All about MAX: a male adult voxel phantom for monte carlo calculations in radiation protection dosimetry,” *Physics in Medicine and Biology*, vol. 48, pp. 1239–1262, 2003. (Cited on pages 11 and 132.)

[65] T. Kurihara and N. Miyata, “Modeling deformable human hands from medical images,” in *Proc. SCA ’04*, Switzerland, Aug 2004, pp. 355–363. (Cited on pages 19 and 61.)

[66] N. Kuster, R. Kastle, and T. Schmid, “Dosimetric evaluation of hand-held mobile communication equipment with known precision,” *IEICE Transactions in Communication*, pp. 645–652, 1997. (Cited on page 100.)

[67] H. J. Lamousin and N. N. W. Jr, “NURBS based free-form deformations,” *IEEE Computer Graphics and Applications*, vol. 14, no. 6, pp. 59–65, 1994. (Cited on page 22.)

[68] J. Lee, S.-H. Yoon, and M.-S. Kim, “Realistic human hand deformation,” *Comp. Anim. Virtual Worlds*, vol. 17, pp. 479–489, Jun 2006. (Cited on pages 19 and 61.)

[69] J. P. Lewis, M. Cordner, and N. Fong, “Pose space deformation: a unified approach to shape interpolation and skeleton-driven deformation,” in *Proc. ACM SIGGRAPH Computer Graphics ’00*, New Orleans, LA, Aug 2000, pp. 165–172. (Cited on page 19.)

[70] C.-H. Li, M. Douglas, E. Ofli, B. Derat, S. Gabriel, N. Chavannes, and N. Kuster, “Influence of the hand on the specific absorption rate in the head,” *IEEE Transactions on Antennas and Propagation*, vol. 60, no. 2, pp. 1066–1074, Feb 2012. (Cited on pages 100 and 101.)

[71] W. E. Lorensen and H. E. Cline, “Marching cubes: A high resolution 3D surface construction algorithm,” *ACM SIGGRAPH Computer Graphics*, vol. 24(4), pp. 163–169, Jul 1987. (Cited on pages 7, 29, and 30.)

[72] N. Magnenat-Thalmann, R. Lemperriere, and D. Thalmann, “Joint dependent local deformations for hand animation and object grasping,” in *Proc. Graphics Interface ’88*, Edmonton, Alberta, Jun 1988, pp. 26–33. (Cited on pages 19 and 61.)

[73] M. H. Mat, M. F. B. A. Malek, W. G. Whittow, S. H. Ronald, M. S. Zulkefli, N. Saudin, and L. Mohamed, “The influence of human head model wearing metal-frame spectacles to the changes of SAR and antenna gain: simulation of frontal face exposure,” *Progress In Electromagnetics Research*, vol. 137, pp. 453–473, 2013. (Cited on pages 100 and 115.)

[74] F. Meyer, K. Palmer, and U. Jakobus, “Investigation into the accuracy, efficiency and applicability of the method of moments as numerical dosimetry tool for the head and the hand of a mobile phone user,” *Applied Computational Electromagnetics Society*, vol. 16, pp. 114–125, 2001. (Cited on page 100.)

[75] L. Moccozet and N. Magnenat-Thalmann, “Dirichlet free-form deformations and their application to hand simulation,” in *Proc. Computer Animation ’97*, Geneva, Switzerland, Jun 1997, pp. 93–102. (Cited on page 61.)

[76] V. Monebhurrun, M.-F. Wong, A. Gati, and J. Wiart, “Study of the influence of the hand on the specific absorption rate evaluation of mobile phones,” in *XXXth URSI General Assembly and Scientific Symposium, 2011*, Aug 2011, pp. 1–4. (Cited on pages 100 and 101.)

[77] K. Morgan, W. Snyder, and E. Struxness, *Health physics division annual progress report for period ending July 31 1966*. Oak Ridge TN, USA: Oak Ridge National Laboratory, 1966. (Cited on page 10.)

[78] T. Nagaoka and S. Watanabe, “Postured voxel-based human models for electromagnetic dosimetry,” *Phys. Med. Biol.*, vol. 53(24), pp. 7047–7061, Dec 2008. (Cited on page 6.)

[79] T. Nagaoka, S. Watanabe, K. Sakurai, E. Kuneida, S. Watanabe, M. Taki, and Y. Yamanka, “Development of realistic high resolution whole-body voxel models of japanese adult male and female of average height and weight, and application of models to radio-frequency electromagnetic-field dosimetry,” *Physics in Mededicine and Biology*, vol. 49, pp. 1–15, 2004. (Cited on pages 11 and 132.)

[80] M. Nikolovski, I. Munteanu, A. M. Cassarà, and T. Weiland, “Impact of rings and earrings on the SAR distribution due to mobile phone exposure,” in *Antennas and Propagation Conference (LAPC), 2014 Loughborough*, Nov 2014, pp. 504–508. (Cited on page 108.)

[81] M. Nikolovski, I. Munteanu, and T. Weiland, “Influence of metallic framed spectacles on the SAR distribution due to mobile phone exposure,” in *Proceedings of the 17th International Symposium on Electromagnetic Fields*, 2015. (Cited on page 115.)

[82] G. M. Noetscher, J. Yanamadala, M. Kozlov, S. Louie, A. Nazarian, and S. Makarov, “VHP-female v3.0 FEM/BEM computational human phantom,”

in *24th International Meshing Roundtable (IMR24)*, Okt 2015, pp. 1–4. (Cited on page 11.)

[83] G. M. Noetscher, J. Yanamadala, S. N. Makarov, and A. Pascual-Leone, “Comparison of cephalic and extracephalic montages for transcranial direct current stimulation - a numerical study,” *IEEE Transactions on bio-medical engineering*, vol. 61(9), pp. 2488–2498, 2014. (Cited on page 132.)

[84] A. M. Ostrowski, *Solution of Equations and Systems of Equations*. Academic Press Inc., 1966. (Cited on page 26.)

[85] M. Patrushev, “Computergestützte Gelenkpositionsbestimmung für die Bewegung von voxel Modellen in elektromagnetischen Anwendungen,” Darmstadt, 2013. (Cited on pages 8, 42, 47, and 125.)

[86] N. Petoussi-Henss, M. Zankl, U. Fill, and D. Regulla, “The GSF family of voxel phantoms,” *Physics in Medicine and Biology*, vol. 47, pp. 89–106, 2002. (Cited on pages 7, 14, and 132.)

[87] Public Health England. (9 July 2013) Mobile telephony and health. [Online]. Available: http://www.hpa.org.uk/web/HPAweb&HPAwebStandard/HPAweb_C/1195733844923 (Cited on page 102.)

[88] Remcom. (2014) VariPose. [Online]. Available: http://www.remcom.com/varipose (Cited on page 80.)

[89] T. Rhee, J. P. Lewis, and U. Neumann, “Real-time weighted pose-space deformation on the GPU,” *Computer Graphics Forum*, vol. 25, pp. 439–448, Nov 2006. (Cited on pages 19 and 61.)

[90] S. H. Ronald, M. F. A. Malek, S. I. S. Hassan, C. E. Meng, M. H. Mat, M. S. Zulke, and S. F. Maharimi, “Designing asian-sized hand model for SAR determination at GSM900/1800: simulation part,” *Progress In Electromagnetics Research*, vol. 129, pp. 439–467, 2012. (Cited on pages 100 and 101.)

[91] N. A. Samsuri and J. Flint, “A study on the effect of a metallic ring worn on human fingers using a simple scannable block hand phantom,” in *Antennas and Propagation Conference, 2008. LAPC 2008. Loughborough*, March 2008, pp. 285–288. (Cited on page 108.)

[92] N. A. Samsuri and J. A. Flint, “A study on the effect of loop-like jewellery items worn on human hand on specific absorption rate (SAR) at 1900 MHz,”

in *Antennas and Propagation Conference, 2008. LAPC 2008. Loughborough*, March 2008, pp. 297–300. (Cited on page 108.)

[93] R. Schuhmann and T. Weiland, "Conservation of discrete energy and related laws in the finite integration technique," *Progress In Electromagnetics Research*, vol. 32, pp. 301–316, 2001. (Cited on page 36.)

[94] T. W. Sederberg and S. R. Parry, "Free-form deformation of solid geometric models," *ACM SIGGRAPH Computer Graphics*, vol. 20(4), pp. 151–160, Aug 1986. (Cited on pages 7, 20, 22, and 23.)

[95] Speag. (2014) SEMCAD X. [Online]. Available: http://www.speag.com/products/semcad/solutions/ (Cited on page 87.)

[96] V. Spitzer, M. J. Ackerman, A. L. Scherzinger, and D. Whitlock, "The visible human male: a technical report," *Journal of the American Medical Informatics Association*, vol. 3(2), p. 118, 1996. (Cited on pages 13 and 132.)

[97] G. G. Stokes, *Mathematical and Physical Papers*. Cambridge University Press, 2009, vol. 3. (Cited on page 34.)

[98] M. Teschner, S. Kimmerle, B. Heidelberger, G. Zachmann, L. Raghupathi, A. Fuhrmann, M.-P. Cani, F. Faure, N. Magnenat-Thalmann, W. Strasser, and P. Volino, "Collision detection for deformable objects," *Computer Graphics Forum*, vol. 24, no. 1, pp. 61–81, 2005. [Online]. Available: http://dx.doi.org/10.1111/j.1467-8659.2005.00829.x (Cited on page 128.)

[99] P. Thoma and T. Weiland, "A consistent subgridding scheme for the finite difference time domain method," *International Journal of Numerical Modelling: Electronic Networks, Devices and Fields*, vol. 9, no. 5, pp. 359–374, 1996. (Cited on page 36.)

[100] U.S. National Library of Medicine. (21 September 2015) The visible human project®. [Online]. Available: https://www.nlm.nih.gov/research/visible/visible_human.html (Cited on pages 12, 13, and 134.)

[101] J. Valentin, *Reference man: anatomical, physiological and metabolic characteristics. ICRP publication 23*, Pergamon,Oxford, 1975. (Cited on page 10.)

[102] U. van Rienen and T. Weiland, "Triangular discretization method for the evaluation of rf-fields in waveguides and cylindrically symetric cavities," *Particle Accelerators*, vol. 20, no. 3, pp. 239–266, 1987. (Cited on page 36.)

[103] J. L. Volakis, A. Chatterjee, and L. C. Kempel, *Finite Element Method Electromagnetics: Antennas, Microwave Circuits, and Scattering Applications*. Wiley-IEEE Press, 1998. (Cited on pages 25 and 134.)

[104] M. Vuchkovikj, I. Munteanu, and T. Weiland, "Application of postured human model for SAR measurements," *Advances in Radio Science*, vol. 11, pp. 347–352, 2013. (Cited on pages 54, 59, and 101.)

[105] ——, "Numerical approach for separation and movement of the fingers of the hugo model for analysis of SAR distribution," in *Software, Telecommunications and Computer Networks (SoftCOM), 2013 21st International Conference on*, Sept 2013, pp. 1–5. (Cited on pages 19, 54, 59, 62, and 106.)

[106] T. Weiland, "A discretization model for the solution of Maxwell's equations for six-component fields," *Archiv Elektronik und Uebertragungstechnik*, vol. 31, pp. 116–120, 1977. (Cited on pages 6 and 36.)

[107] T. Weiland, "On the unique numerical solution of Maxwellian eigenvalue problems in three dimensions," *Particle Accelerators*, vol. 17, pp. 227–242, 1985. (Cited on page 36.)

[108] W. Whittow, C. Panagamuwa, R. Edwards, and J. Vardaxoglou, "Specific absorption rates in the human head due to circular metallic earrings at 1800MHZ," in *Antennas and Propagation Conference, 2007. LAPC 2007. Loughborough*, April 2007, pp. 277–280. (Cited on page 108.)

[109] W. Whittow, R. Edwards, C. Panagamuwa, and J. Vardaxoglou, "The SAR effects of popular jewellery on the human head," in *The Second European Conference on Antennas and Propagation, 2007. EuCAP 2007.*, Nov 2007, pp. 1–6. (Cited on page 108.)

[110] W. Whittow, C. Panagamuwa, R. Edwards, and J. Vardaxoglou, "Effect of tongue jewellery and orthodontist metallic braces on the SAR due to mobile phones in different anatomical human head models including children," in *Antennas and Propagation Conference, 2008. LAPC 2008. Loughborough*, March 2008, pp. 293–296. (Cited on page 108.)

[111] T. Wu, L. Tan, Q. Shao, C. Zhang, C. Zhao, Y. Li, E. Conil, A. Hadjem, J. Wiart, B. Lu, L. Xiao, N. Wang, Y. Xie, and S. Zhang, "Chinese adult anatomical models and the application in evaluation of rf exposures," *Physics in Medicine in Biology*, vol. 56, pp. 2075–2089, 2011. (Cited on pages 11 and 132.)

[112] M. Zankl, N. Petoussi-Henss, U. Fill, and D. Regulla, “The application of voxel phantoms to the internal dosimetry of radionuclides,” *Radiation Protection Dosimetry*, vol. 105, pp. 539–548, 2003. (Cited on pages 11, 14, and 132.)

[113] M. Zankl and A. Wittmann, “The adult male voxel model “Golem” segmented from whole-body CT patient data.” *Radiation and Environmental Biophysics*, vol. 40(2), pp. 153–162, 2001. (Cited on page 12.)

[114] M. Zhang and X. Wang, “Influence on SAR due to metallic frame of glasses based on high-resolution chinese electromagnetic human model,” in *Electromagnetic Compatibility (APEMC), 2010 Asia-Pacific Symposium on*, April 2010, pp. 48–51. (Cited on page 115.)

[115] G. Zubal, C. Harrel, E. Smith, Z. Ratner, G. Gindi, and P. Hoffer, “Computerized three-dimensional segmented human anatomy,” *Medical Physics*, vol. 21, pp. 299–302, 1994. (Cited on page 132.)

Curriculum Vitae

Marija Nikolovski (maiden name: Vuchkovikj)
Born 02.08.1985 in Skopje, Macedonia

Education

09/92-06/00 Primary school "Gjorche Petrov", Skopje, Macedonia
09/00-06/04 Gymnasium "Nikola Karev", Skopje, Macedonia

Academic Studies

10/2004-09/2008 Informatics and Computer Engineering, Faculty of Electrical Engineering and Information Technologies, University "Ss Cyril and Methodius", Skopje, Macedonia

09/2008 Bachelor of Science in Electrical Engineering and Information Technologies, majoring in Informatics and Computer Engineering. Bachelor thesis subject: "Performance of ad hoc networks for realistic models of movement through 3D terrain", supervisor Prof. Dimitar Trajanov

11/2008-11/2010 Computer Networks and E-Technologies, Faculty of Electrical Engineering and Information Technologies, University "Ss Cyril and Methodius", Skopje, Macedonia

11/2010 Master of Science in Electrical Engineering and Information Technologies, majoring in Computer Networks and E-Technologies. Master thesis subject: "Performance analysis of ad hoc networks on 3D terrain modeled with triangular irregular network"

Work Experience

10/2007-06/2008 Assistant, Faculty of Electrical Engineering and Information Technologies, University “Ss Cyril and Methodius”, Skopje, Macedonia

12/2008-06/2009 Junior Teaching Assistant, Faculty of Communication and IT, FON University, Skopje, Macedonia

07/2009-09/2011 Software Engineer, Printec Group of Companies, Skopje, Macedonia

09/2009-09/2011 Trainer/Lecturer, Semos Education, Skopje, Macedonia

11/2012-03/2015 Research Assistant, Computational Electromagnetics Laboratory, Faculty of Electrical Engineering and Information Technology, Technical University Darmstadt, Darmstadt, Germany

11/2015-12/2016 Software Development Engineer, CST AG, Darmstadt, Germany

Publications

2009 S. Filiposka, D. Trajanov, M. Vuckovik: “Performances of Clustered Ad Hoc Networks on 3D Terrains”, in: Proceedings of the 2nd International Conference on Simulation Tools and Techniques, Rome, Italy, 2009, pp. 45:1–45:10.

2010 M. Vuckovik, D. Trajanov, S. Filiposka: “Durkin’s Propagation Model Based on Triangular Irregular Network Terrain”, in: ICT Innovations 2010, Springer Berlin Heidelberg, 2011, pp. 333-341.

2012 M. Vuchkovikj, I. Munteanu, T. Weiland: “Application of postured human model for SAR measurements”, in: Advances in Radio Science, Vol. 11 (2013), pp. 347–352.

2013 M. Vuchkovikj, I. Munteanu, T. Weiland: “Numerical approach for separation and movement of the fingers of the HUGO model for analysis of SAR distribution”, in: Proceedings of the 21st International Conference on Software, Telecommunications and Computer Networks (SoftCOM), Sept, 2013, pp. 1-5.

2014 M. Nikolovski, I. Munteanu, A. M. Cassarà, T. Weiland: “Impact of rings and earrings on the SAR distribution due to mobile phone exposure”, in: Proceedings of the Antennas and Propagation Conference (LAPC), Loughborough, 2014, pp. 504-508.

2015 M. Nikolovski, I. Munteanu, T. Weiland: “Influence of Metallic Framed Spectacles on the SAR Distribution due to Mobile Phone Exposure”, in: Proceedings of the 17th International Symposium on Electromagnetic Fields, Valencia, 2015.

Awards

Best paper award on the international conference Simutools, Rome, Italy, March 2009 for “Performances of Clustered Ad Hoc Networks on 3D Terrains” written by S. Filiposka, D. Trajanov, M. Vuckovik.

Acknowledgment

This work is jointly supported by the ’Excellence Initiative’ of the German Federal and State Governments and the Graduate School of Computational Engineering (GSCE) and the Computational Electromagnetic Laboratory (TEMF) at Technical University Darmstadt. The knowledge and the success are greater when they are shared, thus finishing this thesis would not have been possible without the support, help and discussions with several people, to whom I would like to sincerely thank:

- Prof. Dr.-Ing. Thomas Weiland, for giving me the great opportunity to work on this thesis and be part of the GSCE and TEMF. I would especially like to thank him for his support during all the years of my PhD work.

- Prof. Dr.-Ing. Irina Munteanu, for her support and the productive discussions and ideas during the realization of this PhD thesis. Additionally, I would like to thank her for giving me the opportunity to assist her and to conduct the exercises on Technical Electrodynamics for iCE for three years.

- Dr.-Ing. Alexander Prokop, for his constructive comments and ideas during the PhD work, as well as the given opportunity to work together with him as a part of the Bio-EM team at CST.

- My colleagues at the GSCE and TEMF, especially Dr.-Ing. Irene Woyna with whom I shared the office at TEMF and became very good friends.

- My husband Ivo, who was the main supporter during my whole studies as well as a reason to move to Germany in order to challenge myself and upgrade my knowledge to this level.

- My son Teodor, who changed my life and taught me about setting priorities.

- My mother Danica, my father Mito, my sister Ivana and my husband’s family, Slobodan, Verica and Andrijana, for encouraging me and giving me support during all these years.

- My friends in Macedonia and in Germany.